MINIATURE OPTICAL FIBER PHOTOACOUSTIC GAS SENSORS BASED ON 3D MICRO-PRINTED OPTOMECHANICAL MICRORESONATORS

LI TAIGE

PhD

The Hong Kong Polytechnic University

2025

The Hong Kong Polytechnic University

Department of Electrical and Electronic Engineering

Miniature Optical Fiber Photoacoustic Gas Sensors Based on 3D Micro-printed Optomechanical Microresonators

LI Taige

A thesis submitted in partial fulfillment of the requirements

for

the degree of Doctor of Philosophy

May 2025

CERTIFICATE OF ORIGINALITY

I hereby declare that this thesis is my own work and that, to the best of my knowledge and belief, it reproduces no material previously published or written, nor material that has been accepted for the award of any other degree or diploma, except where due acknowledgement has been made in the text.

_____ (Signed)

(LI Taige)

Abstract

Gas sensors have become an important tool for various industrial, agricultural, and environmental applications, such as hazardous gas leakage detection, food production/storage monitoring, and air quality real-time assessment. Compared with electrical gas sensors, which typically possess inherent limitations, such as poor selectivity, slow response, susceptibility to electromagnetic interference, optical gas sensors have not only the advantages of high selectivity and fast response but also the ability for remote monitoring in harsh environments. Most of the optical gas sensors are based on laser absorption spectroscopy (LAS), which renders the advantage for very high selectivity because of the use of narrow-linewidth excitation lasers matching well with specific gas absorption lines. One of the most sensitive and robust LAS gas sensing technologies is photoacoustic spectroscopy (PAS), wherein absorbed modulated light induces acoustic waves proportional to gas concentration, enabling direct transduction of molecular absorption into quantifiable acoustic signals. To detect the induced acoustic signal, existing optical PAS gas sensors typically require the incorporation of acoustic wave transducers, such as tuning forks, diaphragms, and cantilevers. However, these detection approaches suffer from inherent trade-offs between miniaturization, sensitivity, and operational simplicity.

To address these limitations, this thesis is devoted to developing miniature optical fiber PAS gas sensors with directly 3D micro-printed spirally-suspended optomechanical microresonators (OMRs). A special design of planar-spiral spring OMR (PSS-OMR) is employed to tackle the trade-off between small size and high sensitivity for PAS gas sensing. The use of planar-spiral springs can not only reduce the size of the entire

structure for sensor minimization but also tailor vibration resonance for sensitivity enhancement. A thin-film reflector is introduced in the OMR to form Fabry-Pérot (F-P) micro-interferometer together with the end-face of optical fiber for optical interferometric readout of acoustic signals. Moreover, to precisely fabricate such exquisite and complex PSS-OMRs, an optical 3D micro-printing technology has been developed to enable rapid in-situ printing of micrometer-scale OMRs using SU-8 epoxy photoresist, which has advantages of high optical transparency, high mechanical strength, and superb chemical and temperature resistance, for development of small-size PAS sensors.

Firstly, we designed and fabricated a miniature optical fiber PAS gas sensor based on a 3D micro-printed ferrule-top PSS-OMR. The end-face of a fiber-optic ferrule is a platform directly exposed with light without need of additional coupling, offering opportunities for micro-engineering 2D/3D microstructures for development of novel miniature optical fiber sensors. In the experiments, we directly printed a PSS-OMR with a diameter of 400 μm at a 1.25-mm wide fiber-optic ferrule to make a miniature optical fiber PAS sensor. The testing results showed that this sensor can very sensitively detect acoustic and ultrasonic signals from 100 Hz to 60 kHz. Compared with non-resonance response, the sensor's acoustic response can be greatly enhanced by 102 times when it operates at the fundamental resonance frequency. After integrating the sensor with a 1.4 μL non-resonant photoacoustic cell, the optical fiber PAS sensors can be used to detect acetylene (C_2H_2) gas at the concentration level of 45 ppb, and the sensor's response time can be as short as 0.2 seconds.

To develop ultrasmall PAS for applications in highly space-constrained environments, we further developed an ultraminiature optical fiber-tip PAS gas sensor based on a 3D micro-printed fiber-top PSS-OMR.

Compared with the abovementioned optical fiber PAS sensor, it is a monolithic design with a much smaller sensor head and without the need of extra PA cell. Its sensor head has the same size as a standard single-mode optical fiber, i.e., with a diameter of 125 μm. Experimental results demonstrate that mechanical vibrational resonance of PSS-OMR can enhance the sensor's acoustic sensitivity by about two orders of magnitude. Gas sensor testing experiments reveal that, comparing with off-resonance operation, the optical fiber-tip PAS sensor at on-resonance operational mode can achieve a remarkably stronger PA signal whose signal-to-noise ratio (SNR) is improved by up to 550 %. The sensor can detect acetylene (C_2H_2) at a very low concentration level of 55 ppb, and its response time is less than 0.2 seconds.

These small-size high-sensitivity optical fiber PAS gas sensors provide new trace-gas detection technology for various applications such as environmental monitoring and industrial process controls in many space-constrained applications, such as in-reactor or battery monitoring and medical diagnosis.

Publications arising from the thesis

Journal papers:

1. **T. Li**, P. Zhao, P. Wang, S. Liu, L. Guo, W. Jin, and A. P. Zhang, "Ultra-miniature and sensitive optical fiber-tip optomechanical resonant photoacoustic spectroscopy gas sensors," 2025. (under review)
2. P. Wang, **T. Li**, H. Lin, P. Zhao, S. Liu, H.-Y. Tam, and A. P. Zhang, "Miniature optical fiber accelerometer based on an in-situ 3D micro-printed ferrule-top Fabry-Pérot microinterferometer," *Light: Advanced Manufacturing*, Vol. 6, Art. No. 18, 2025.
3. **T. Li**, P. Zhao, P. Wang, K. V. Krishnaiah, W. Jin, and A. P. Zhang, "Miniature optical fiber photoacoustic spectroscopy gas sensor based on a 3D micro-printed planar-spiral spring optomechanical resonator," *Photoacoustics*, Vol. 40, p. 100657, 2024.
4. P. Zhao, K. V. Krishnaiah, L. Guo, **T. Li**, H. L. Ho, A. P. Zhang, and W. Jin, "Ultraminiature optical fiber-tip 3D micro-printed photothermal interferometric gas sensors," *Laser & Photonics Reviews*, Vol. 2024, p. 2301285, 2024.
5. H. Wang, Z. Chen, **T. Li**, H. Xie, B. Yin, S. H. D. Wong, Y. Shi, and A. P. Zhang, "Optofluidic chip with directly printed polymer optical waveguide Mach-Zehnder interferometer sensors for label-free biodetection," *Biomedical Optics Express*, Vol. 15, pp. 3240-3250, 2024.
6. Z. Ding, H. Wang, **T. Li**, X. Ouyang, Y. Shi, and A. P. Zhang, "Fabrication of polymer optical waveguides by digital ultraviolet lithography," *IEEE/OSA Journal of Lightwave Technology*, Vol. 40, Iss. 1, pp. 163 – 169, 2022.

Conference papers:

1. P. Wang, **T. Li**, S. Liu, X. Cheng, H.-Y. Tam, & A. P. Zhang, "Ultraminiature Optical Fiber Accelerometer Based on a 3D Microprinted Proof Mass-Integrated Fabry-Pérot Microinterferometer," *29th International Conference on Optical Fiber*

Sensors (OFS), Porto, Portugal, 25-30 May 2025.

2. **T. Li**, P. Zhao, P. Wang, K. V. Krishnaiah, W. Jin, and A. P. Zhang, "Miniature optical fiber photoacoustic gas sensor based on a 3D micro-printed ferrule-top optomechanical resonator," *12th Optical Fiber Sensors Conference China* (*OFS-China* 2024)*,* 20 - 22 Sept 2024, Chongqing, China.
3. P. Wang, **T. Li**, and A. P. Zhang, "Optical fiber ferrule-top suspended optomechanical microresonators for acceleration sensing," *Conference on Lasers and Electro-Optics (CLEO) 2024*, ID: AM2A.4, North Caroline, USA, 07– 12 May 2024.
4. H. Wang, Z. Chen. **T. Li**, Y. Shi, and A. P. Zhang, "Fabrication of polymer optical waveguide-based Mach-Zehnder interferometer microsensors for integrated optofluidic biodetection," *Optica Sensing Congress 2023*, ID: STu3C.4, Munich, Germany, Aug. 2023.
5. **T. Li**, K. V. Krishnaiah, P. C. Zhao, and A. P. Zhang, "Optical fiber ferrule-top spirally-suspended optomechanical microresonators for photoacoustic spectroscopic gas sensing," *Conference on Lasers and Electro-Optics/Europe (CLEO Europe) 2023*, ID: 829, Munich, Germany, 26– 30 June 2023.

Acknowledgements

I would like to appreciate everyone who provided me with help during the pursuing of my PhD degree in the Hong Kong Polytechnic University.

First, I would like to express my sincerest gratitude to my chief supervisor, Prof. A. Ping Zhang, for his patience and kind guidance. His profound knowledge and constructive suggestions helped me a lot in my PhD period. And his passion, meticulosity and enthusiasm for research set me a good example and will influence me in the following days. I am also grateful for his suggestive advice and efforts on revising my writings and presentations for the past few years.

I would also like to thank Dr. Pengcheng Zhao for providing me with great help in conducting gas sensing experiments and giving suggestions. I appreciate all members in the Micro/nano Photonics Research Lab for having such a great research atmosphere and helping each other. I express my gratitude to the kind support offered by various people in the Polytechnic University, who have helped my study and life throughout the years.

Finally, I want to express my gratitude to my parents, friends, and Kaixin Chen for their unselfish dedication and support.

Table of Contents

List of Figures

List of Tables

List of Acronyms

FEM	Finite element method
FFT	Fast Fourier transformation
FP	Fabry-Pérot
FPI	Fabry-Pérot interferometer
FSR	Free spectral range
FWHM	Full width at half maximum
LIA	Lock-in amplifier
LoD	Limit of detection
MEMS	Microelectromechanical systems
NEA	Noise equivalent absorption
NEC	Noise equivalent concentration
NNEA	Normalized noise equivalent absorption
OMR	Optomechanical microresonator
PA	Photoacoustic
PAS	Photoacoustic spectroscopy
PTS	Photothermal spectroscopy
SNR	Signal-to-noise ratio

Introduction

Chapter 1

1.1 Background

Gas sensors have become an active research area in the past decades due to their important purposes such as detecting toxic or flammable gases to ensure safety, monitoring feedstocks and key species in products and reaction processes [1], as well as analyzing various breath gases for metabolic health or disease diagnosis, including nitric oxide (NO), ethane (C_2H_6), ammonia (NH_3), and so on [2]. Compared with electrical gas sensors, which typically possess limitations of poor selectivity, slow response, susceptibility to electromagnetic interference, optical gas sensors have not only the advantages of high selectivity and fast response but also the ability for remote monitoring in harsh environments. Various technologies have been utilized for optical gas detection, including non-dispersive infrared (NDIR) [3], spectrophotometry [4], laser absorption spectroscopy (LAS) [5], and so on. Here LAS has been widely studied and adopted by industries due to its advantages of very high selectivity, since it uses a narrow-linewidth excitation laser matching well with specific gas absorption lines for gas detection.

One of the most sensitive and robust LAS gas sensing technologies is

photoacoustic spectroscopy (PAS) [6], which is regarded as a prospective candidate for highly sensitive and compact gas sensors. Instead of using a photodetector to measure the light intensity associated with gas absorption, a microphone is utilized to measure the acoustic signal generated from photoacoustic effect. Compared with other techniques, PAS gas sensors could achieve both sensitivity and small size because their detection limit does not scale linearly with the laser-gas interaction length. It also make them to easily benefit from high-power lasers along with the elimination of the maximum peak power limit of the photodetector [1]. Conventional PAS systems rely on acoustic sensors to transduce sound into electrical signals, such as electromagnetic, piezoresistive, or piezoelectric microphones [7]. However, these sensors often struggle to reconcile miniaturization, sensitivity, and optical compatibility.

This limitation has driven the development of all-optical PAS sensors, where fiber-optic acoustic sensors replace traditional microphones. By leveraging optical fiber's unique properties, such as micrometer-scale dimensions, immunity to electromagnetic interference, and seamless integration with photonic systems, these sensors enable fully optical PAS platforms. Many optical fiber technologies, such as fiber Bragg gratings [8], fiber-based Fabry-Pérot cavities [9], micro/nano fibers [10], photonic crystal fibers [11] and other specialty optical fibers [12], have been employed to develop various kind of sensors for many types of gases.

These fiber-optic sensors can generally achieve both small size and remote sensing, compared to spatial optical acoustic sensors [13]. Notably, the flat end-face of optical fiber provides a unique platform for developing miniature photonic sensors. The small size and large aspect ratio of optical fibers make it a promising candidate for in vivo and in situ sensing as a highly integrated photonic sensing device [14]. Optical fiber-based micrometer-scale Fabry–Perot interferometer (FPI) can be devised to measure acoustic signal-caused wavelength shifts and light intensity change. The common configuration of a fiber-optic FPI acoustic sensor is to use a flat end-face to form a microcavity with a mechanical-sensitive element, such as a thin diaphragm or a cantilever [15].

In recent years, the advances in micro- and nano-fabrication technology and the newly developed materials have open up opportunities in the development of new gas sensors. As for optical fiber-tip sensors, many fabrication techniques have been applied to pattern the flat end-surface of an optical fiber, such as photolithography [16], nanoimprinting [17], electron-beam lithography [18], focused ion-beam milling [19], two-photon polymerization [20], femtosecond laser ablation [21], etc. Notably, fabrication processes require proper optimization for different designs of optical fiber sensors, which is quite different from these planar substrates, due to its ultra-small size and high aspect ratio.

1.2 Motivations and objectives of research

Small-size and high-sensitivity optical fiber gas sensors are very appealing for applications requiring in situ gas monitoring within space-constrained environments, such as industrial pipes, reaction chambers, or embedded systems. Despite advances in optical fiber-based PAS technologies and micro/nano-fabrication methods, existing sensors often sacrifice performances to achieve small size. Conventional designs struggle to balance compactness with the acoustic sensitivity needed for trace gas detection, limiting their practicality in real-world settings.

This thesis addresses these limitations by developing miniature PAS gas sensors using 3D-microprinted optomechanical microresonators (OMR) on the end faces of fiber-optic ferrule and optical fiber. Especially a specially designed optomechanical microresonator, i.e., planar-spiral spring optomechanical microresonators (PSS-OMR)), is devised to develop miniature optical fiber PAS gas sensors. Using our own-established optical 3D micro-printing technology, we first designed and fabricated a miniature optical fiber PAS gas sensor based on a PSS-OMR that 3D micro-printed on the end-face of fiber-optic ferrule. Thereafter, an ultraminiature optical fiber-tip PAS gas sensor was developed by further optimization of 3D micro-printing technology to fabricate a fiber-top PSS-OMR. Both optical fiber PAS gas sensors have been demonstrated to detect C_2H_2 gas in experiments.

1.3 Outline of thesis

The chapters of this thesis are organized as below:

Chapter 1: Introduction. This chapter introduces the motivation for developing small-size high-sensitivity optical fiber PAS gas sensors. It reviews the challenges of conventional PAS systems, outlines the objectives of this research, and presents the thesis structure.

Chapter 2: Overview of optical fiber PAS gas sensing technologies. This chapter overviews optical fiber acoustic sensors in PAS gas sensors based on different sensing schemes. First, it details the working principles of PAS gas sensors, including signal generation and sensitivity limits. Next, it reviews existing optical fiber PAS sensors for gas sensing, briefing their structural design and performances. Finally, it categorizes fabrication techniques for optical fiber PAS sensors, identifying the gaps between the design and fabrication.

Chapter 3: Miniature optical fiber photoacoustic spectroscopy gas sensor based on a 3D micro-printed ferrule-top optomechanical resonator. In this chapter, a miniature optical fiber PAS gas sensor based on a planar-spiral spring OMR (PSS-OMR), which is in situ 3D micro-printed on the end-face of a fiber-optic ferrule, is presented. Experimental results demonstrate that mechanical vibrational resonance can enhance the sensor's acoustic sensitivity by over two orders of magnitude. Together with a 1.4 μL non-resonant photoacoustic cell, it can detect C_2H_2 gas

concentration at the 45-ppb level, and its response is very fast approximating 0.2 seconds.

Chapter 4: Ultraminiature optical fiber photoacoustic spectroscopy gas sensor based on a 3D micro-printed fiber-top optomechanical microresonator. In this chapter, an ultraminiature optical fiber-tip PAS gas sensor based on a PSS-OMR that is 3D micro-printed on the end-face of an optical fiber is further developed. Compared with the above-mentioned optical fiber PAS sensor, it has a much smaller sensor head whose diameter is the same as a standard single-mode optical fiber, i.e. 125 μm. Moreover, it has a monolithic design that directly transmits pump and probe laser lights via the same optical fiber, eliminating the requirement of photoacoustic cell and alignment complexities in traditional PAS sensors. The sensor can detect C_2H_2 gas at the concentration of one-hundred ppb level. Compared to optical fiber photothermal sensor, the signal-noise-ratio (SNR) of this optical fiber-tip PAS sensor can increase 550%.

Chapter 5: Conclusions and outlook. This chapter summarizes the thesis and outlook for future work on optical fiber PAS gas sensors.

Chapter 2 Overview of optical fiber photoacoustic spectroscopy gas sensing technologies

2.1 Introduction

Optical gas sensing has become an important technology for real-time environmental monitoring due to its rapid response, minimal baseline drift, and non-destructive sampling capabilities [13]. Typical optical gas sensing methods include light-induced thermoelastic spectroscopy (LITES) [22], tunable diode laser absorption spectroscopy (TDLAS) [23] or cavity-enhanced absorption spectroscopy (CEAS) [24], which rely on direct optical absorption measurements. In contrast, photoacoustic spectroscopy (PAS) distinguishes itself through a very different detection mechanism: it converts absorbed optical energy into acoustic waves, making the length of light absorption path less important. This unique feature enables PAS sensing devices to achieve both low detection limits and compact size. Recent advancements further improve PAS gas sensor's performance by replacing conventional microphones with optical acoustic sensors, which address the limitations of electromagnetic interference and bandwidth constraints.

Acoustic waves, spanning frequencies from infrasound (<20 Hz) to

ultrasound (>20 kHz), are ubiquitous in both natural phenomena and industrial applications [25]. Traditional electroacoustic transducers, while widely used, face challenges in harsh environments with strong electromagnetic interference, explosive hazards, or requirements for remote monitoring. Optical acoustic sensors offer a robust alternative due to their inherent immunity to electromagnetic noise and compatibility with long-distance signal transmission. Especially the advances in micro- and nano-fabrication have further propelled the field to facilitate the development of miniaturized high-sensitivity acoustic detectors with reduced manufacturing costs, aligning with the demands of modern industrial sensing.

In particular, fiber-optic acoustic sensors hold promise for PAS gas sensing, which has numerous advantages such as compact size, multiplexing capability, and adaptability to harsh environments. While fiber Bragg gratings (FBGs), long-period gratings, and interferometric configurations are common, fiber-tip acoustic sensors stand out for their ultracompact size and potential cost efficiency [15]. The unique geometry of optical fiber tips—featuring microscopic cross-sections and high aspect ratios—provides an unconventional platform for sensor design. It allows unobtrusive deployment in confined or hazardous spaces, holding promise in many industrial applications.

This chapter starts from the working principles of PAS gas sensing,

with emphasis on performance enhancements for trace gas detection. Subsequently, recent advances of fiber-optic PAS gas sensors are reviewed, categorizing them by transduction mechanisms. Finally, state-of-the-art fabrication techniques for fiber-optic PAS gas sensors are discussed, highlighting trends in structural design and material innovation.

2.2 Working principles of photoacoustic spectroscopy gas sensors

This section outlines the working principles of photoacoustic spectroscopy (PAS) and their application in gas sensors. PAS is a spectroscopic method derived from light absorption spectroscopy (LAS) [26]. As an absorption-based technique, it retains the core advantages of absorption spectroscopy, including high selectivity, sensitivity, and suitability for trace gas analysis. Unlike conventional optical gas detection methods, PAS transduces convert light energy into acoustic waves via localized heating in the target medium, which are then detected using acoustic sensors. In the following sections, fundamentals of LAS and PAS gas sensors are reviewed.

2.2.1 Fundamentals of laser absorption spectroscopy

The identification of individual gas species via absorption spectroscopy relies on selective photon-matter interactions. Chemical compounds often exhibit distinct absorption signatures within the UV/visible to mid-infrared

spectral ranges, which serve as molecular fingerprints for detection. When the wavelength of a laser is tuned to a species-specific absorption line and irradiates a gas sample, photons are absorbed by target molecules, inducing a transition from ground to excited electronic or vibrational states. These excited molecules subsequently undergo thermal relaxation, releasing energy as heat and generating localized pressure fluctuations [27].

The Beer-Lambert law governs the theoretical foundation of absorption spectroscopy, defining the transmitted light intensity $I(\nu)$ through an absorbing medium of path length l at wavenumber ν as:

$$I(\nu) = I_0(\nu)\exp\left(-\alpha(\nu)l\right) \tag{2.1}$$

where $I_0(\nu)$ is the incident intensity, $\alpha(\nu)$ is the absorption coefficient of gas sample and ν typically has unit of cm^{-1}. This relationship underpins quantitative gas analysis by linking absorption magnitude to species concentration.

The absorption coefficient $\alpha(\nu)$ in the Beer-Lambert law is directly proportional to the absorption line intensity S ($cm^{-1}\cdot molecule^{-1}\cdot cm^2$), a parameter rooted in the quantum mechanical properties of target molecules. Specifically, S is determined by the population N_n of molecules in the lower quantum state n and the transition probability between lower state n and higher state m (quantified by the Einstein coefficient B_{nm}), which is given by [28]:

$$S = \frac{N_n}{N}\frac{h\upsilon_{nm}}{c}B_{nm}[1 - \exp\left(\frac{hc\upsilon_{nm}}{kT}\right)], \quad (2.2)$$

where c is the vacuum light velocity, k is the Boltzmann constant, h is the Planck constant, T is the temperature in K, and N is the target gas molecular density in mol/cm^3.

In real-world environments, individual spectral lines are broadened by temperature, pressure, and concentrations of other gases. For instance, at atmospheric pressure, the absorption coefficient $\alpha(\upsilon)$ of a single absorption line broadens into a Lorentzian profile due to pressure effects as [1]:

$$\alpha = C_{mol}S\frac{\gamma}{\pi(\gamma^2+(\upsilon-\upsilon_0)^2)}, \quad (2.3)$$

where C_{mol} is the gas concentration (molecules·cm^{-3}), γ is the pressure- and temperature-dependent half-width at half-maximum (HWHM, cm^{-1}), and υ_0 is the central position of absorption line. The HWHM γ itself varies with the partial pressure and temperature of the gas.

2.2.2 Principles of photoacoustic spectroscopy gas sensing

Photoacoustic spectroscopy is derived from laser absorption spectroscopy. When laser energy applied to a gas medium undergoes periodic modulation, cyclical thermal expansion occurs, producing acoustic waves due to photoacoustic effect. A simplified representation of this process is shown in **Fig. 2.1**, where three steps are involved: Initially, heat release happens in the sample material due to relaxation of optical light absorption through

molecular collisions. Thereafter, with a localized short-term heating and expansion, both sound and thermal waves generate. Finally, the resulting pressure signal within the photoacoustic chamber is measured by using a microphone.

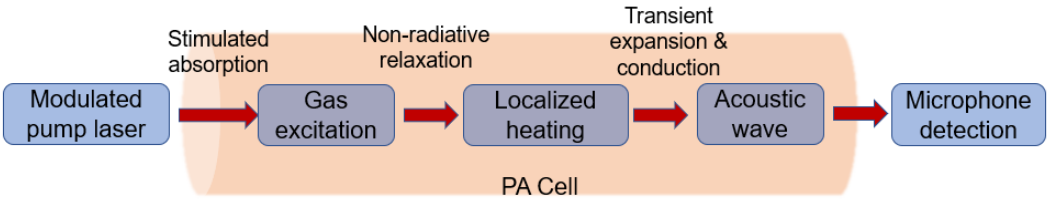

Figure 2.1. Schematic of photoacoustic processes including optical energy absorption, molecular vibrational relaxation, thermal energy transfer, and pressure wave transmission.

To make the analysis for the PAS theory clearer, the following part is divided into two sections: heat production and acoustic wave generation.

(a) ***Heat production***

The conversion from optical energy to heat is induced by molecular absorption of photons at a proper wavelength and subsequent non-radiative relaxation of the excited state (collisional relaxation). Heat production in a gaseous sample excited by an intensity modulated laser beam can be described by utilizing molecule population levels model [29]. In a simplified two-level absorption model, the population dynamics of the excited vibrational state (density N') relative to the ground state (density N-N') is governed by:

$$\frac{dN'}{dt} = (N - N')\sigma\phi - N'\sigma\phi - \frac{N'}{\tau}, \tag{2.4}$$

where σ is the absorption cross-section, ϕ is photon flux, and $\tau^{-1} = \tau_n^{-1} + \tau_r^{-1}$ represents the total relaxation rate combining nonradiative (τ_n) and radiative (τ_r) processes. The terms on the right correspond to photon absorption, stimulated emission, and relaxation (both spontaneous emission and nonradiative decay). Under typical atmospheric conditions, nonradiative relaxation dominates ($\tau \approx \tau_n$) [28], ensuring nearly all absorbed energy converts to heat. For weak absorption ($\sigma\phi \ll \tau^{-1}$), the excited-state population remains small ($N \ll N'$), allowing omission of the stimulated emission term ($N'\sigma\phi$). This simplifies Eq. (2.4) to:

$$\frac{dN'}{dt} = N\sigma\phi - \frac{N'}{\tau}, \tag{2.5}$$

Here, the heat generation rate directly relates to the nonradiative decay term N'/τ, as radiative contributions become negligible under these assumptions.

When the photon flux is time-modulated as $\phi = \phi_0(1 + e^{i\omega t})$, with angular frequency ω, the steady-state solution of Eq. (2.5) becomes:

$$N' = \frac{N\sigma\phi_0\tau_n}{\sqrt{1+(\omega\tau_n)^2}} e^{i(\omega t-\varphi)}, \tag{2.6}$$

where φ represents the phase delay of the excited-state population N' relative to the modulated photon flux.

Under low-frequency modulation ($\omega \ll 10^6$ rad/s,$\omega\tau \ll 1$), the heat generation rate simplifies to:

$$H = H_0 e^{i\omega t}, \tag{2.7}$$

and

$$H_0 = N\sigma I_0 = \alpha I_0, \tag{2.8}$$

where $\alpha=N\sigma$ is the gas absorption coefficient. In practical gas sensing systems, where modulation frequencies are typically at kHz scale, the condition $\omega\tau \ll 1$ holds due to short relaxation times (τ). Consequently, thermal response remains in phase with the optical intensity modulation, eliminating measurable phase lag.

(b) Acoustic wave generation

The generation of acoustic and thermal waves in PA systems is modeled through coupled governing principles: momentum conservation (Navier-Stokes equations), energy conservation (thermal diffusion equation), mass conservation (continuity equation), and thermodynamic state relations. They collectively describe the interdependent dynamics of four key variables: the spatially and temporally varying temperature $T(\mathbf{r},t)$, pressure $P(\mathbf{r},t)$, density $\rho(\mathbf{r},t)$, and the three-dimensional velocity vector $\mathbf{v}(\mathbf{r},t)$, which defines the system's photoacoustic and photothermal behaviors. These variables represent changes induced by light absorption compared to their equilibrium values, and consequently they could be regarded as very small quantities. Higher order products can be neglected as well. In that sense, a linearized wave equation is derived. To describe thermal conduction and friction in fluid or gas, the linearized Navier-Stokes equation is expressed as [30]:

$$\frac{\partial \mathbf{v}}{dt} = -\frac{1}{\rho_0}\nabla p(\mathbf{r},t) + D_v \nabla(\nabla \cdot \mathbf{v_l}), \tag{2.9}$$

where $D_v = 4\eta/3\rho_0 + \eta_b/\rho_0$. Here, η and η_b denote the shear and bulk viscosity coefficients, respectively, ρ_0 is the equilibrium gas density, and $\boldsymbol{v_l}$ is the longitudinal velocity component. The transverse velocity $\boldsymbol{v_t}$, which does not contribute to acoustic pressure generation, is disregarded.

Sound pressure fluctuations correlate with temperature variations, governed by the thermal diffusivity equation:

$$\frac{K}{\rho_0 C_p}\nabla^2 T(\mathbf{r},t) = \frac{\partial}{\partial t}\left(T_a(\mathbf{r},t) - \frac{\gamma-1}{\gamma\beta_T}\kappa_T p(\mathbf{r},t)\right) - \frac{H(\mathbf{r},t)}{\rho_0 C_p}, \tag{2.10}$$

where K is thermal conductivity, Cp is the specific heat at constant pressure, $\gamma = C_p / C_v$ is the heat capacity ratio, β_T is the thermal expansion coefficient, κ_T is the isothermal compressibility, and $H(\mathbf{r},t)$ represents the volumetric heat power density deposited in the medium.

To complete the analysis of the system, the mass-density continuity equation is utilized:

$$\frac{\partial \rho(\mathbf{r},t)}{\partial t} + \rho_0 \nabla \cdot \mathbf{v_l} = 0, \tag{2.11}$$

along with the thermodynamic equation of state

$$\rho(\mathbf{r},t) = \frac{\gamma}{c_s^2}\left(\rho(\mathbf{r},t) - \frac{\beta_T}{\kappa_T}T(\mathbf{r},t)\right), \tag{2.12}$$

where c_s is the sound velocity in gas.

To derive the modified wave equation, by combining Eq. (2.9) – Eq. (2.12), $\boldsymbol{v}_l$ and $\rho(\mathbf{r},t)$ are eliminated and we have

$$\nabla^2 p(\mathbf{r},t) = \frac{\gamma}{c_s^2}\left(\frac{\partial^2}{\partial t^2} - D_v\nabla^2\right)\left(p(\mathbf{r},t) - \frac{\beta_T}{\kappa_T}T(\boldsymbol{r},t)\right), \tag{2.13}$$

The coupled equations (2.10) and (2.13) yield two distinct solutions with different underlying mechanisms [31]. The first corresponds to a propagating acoustic wave with wavelengths spanning centimeters to meters, while the second represents a highly attenuated thermal wave with submillimeter wavelengths that rapidly decay near the excitation region. These solutions underpin photoacoustic (PA) and photothermal (PT) detection principles, respectively. When the PA cell dimensions far exceed the thermal wave's decay length, the second-order spatial derivatives of $T(\mathbf{r},t)$ become negligible. Merging Eqs. (2.10) and (2.13) yields a unified pressure wave equation:

$$\nabla^2 p(\mathbf{r},t) - \frac{1}{c_s^2}\frac{\partial^2 p(\boldsymbol{r},t)}{\partial t^2} + \frac{1}{c_s^2}D_v\nabla^2 p(\mathbf{r},t) = -\frac{(\gamma-1)}{c_s^2}\frac{\partial H(\mathbf{r},t)}{\partial t}. \tag{2.14}$$

This equation describes a damped pressure wave, incorporating viscous damping (via D_v) on the left-hand side. Due to the non-analytical nature of the damping term, no closed-form analytical solution exists, necessitating numerical or approximate methods for practical analysis. In this study, the resonance of the acoustic cell is not utilized. For the fundamental acoustic mode (j=0), which corresponds to a uniform pressure distribution within the cavity, the pressure field simplifies to:

$$p(\mathbf{r},t) = A_0(\omega)e^{i\omega t}, \tag{2.15}$$

with

$$A_0(\omega) = \frac{i}{\omega}\frac{\gamma-1}{V_c}\alpha P_0 L. \tag{2.16}$$

This configuration corresponds to a closed non-resonant system, where the modulation frequency is significantly lower than the resonance frequency of the gas cell. Under these conditions, the acoustic wavelength far exceeds the cell dimensions, preventing sound wave propagation and the formation of standing waves. Consequently, the spatially averaged pressure oscillates uniformly at the modulation frequency within the cavity.

From Eq. (2.16), the photoacoustic signal in this non-resonant regime is proportional to the absorbed power (αP_0) and inversely dependent on both the modulation frequency (ω) and cross section area (V_c). For practical applications, efficient signal generation is achieved by using a small cavity (with dimensions much smaller than the acoustic wavelength) and operating at low modulation frequencies, typically in the kHz range.

2.2.3 Wavelength modulation spectroscopy for PAS gas sensing

The development of distributed feedback (DFB) lasers has positioned wavelength modulation spectroscopy (WMS) as the predominant modulation method for trace-gas detection [32, 33]. WMS leverages the tunability and high-frequency modulation capabilities of semiconductor lasers, enabling absorbance measurements with sensitivities in the 10^{-5} – 10^{-6} range that corresponds to parts-per-million (ppm) detection limits for many substances such as CO, CO_2, H_2O, CH_4, NH_3, C_2H_2, etc.

In amplitude modulation (AM)-based photoacoustic spectroscopy

(PAS), the acoustic signal frequency matches the laser modulation frequency. However, this method suffers from coherent acoustic noise generated by periodic heating of photoacoustic cell wall(s) and optical window(s). Since this noise has the same frequency with the signal, it cannot be suppressed by using lock-in amplifier. WMS-based PAS overcomes this limitation through second-harmonic detection (2*f* detection). In this approach, the laser wavelength is slowly tuned across an absorption line while being modulated at a high frequency. The interaction between the modulated light and the absorption line generates signals at the harmonics of the modulation frequency. By collecting the second harmonic (2*f*) component, which exhibits the highest SNR, via lock-in detection, the measured signal becomes directly proportional to the gas concentration. A key advantage of 2*f* detection is the shift of the measurement to higher frequencies at which laser excess noise (e.g., 1/*f* noise) is significantly reduced.

In semiconductor lasers, light modulation is straightforwardly achieved by modulating injection current. This process simultaneously induces both frequency modulation (FM) and intensity modulation (IM) in the emitted light, with a characteristic phase shift (Ψ) between the two modulations. The instantaneous laser frequency governing WMS signals is:

$$\upsilon(t) = \upsilon_0 - \Delta\upsilon \cos(\omega t + \Psi), \tag{2.17}$$

where ν_0 is the optical carrier frequency, $\Delta\nu$ is its maximum deviation, ω =

$2\pi f$ is the modulation angular frequency, and Ψ is the phase shift between the IM and the FM. In case of FM, the laser injection current i is modulated at the angular frequency ω:

$$i(t) = i_0 + \Delta i \cos \omega t, \tag{2.18}$$

which induces simultaneous IM in the emitted light:

$$I(t) = I_0 + \Delta I \cos \omega t, \tag{2.19}$$

where I_0 is the average intensity and ΔI is the amplitude of intensity variation. The optical frequency modulation, however, exhibits a phase shift Ψ relative to the IM, as described by Eq. (2.17). The negative sign in Eq. (2.17) ensures a zero-phase shift between IM and FM at low modulation frequencies.

For the systems with combined IM–FM effects, the intensity dependence on optical frequency is modeled as a linear relationship:

$$I_0(x) = I_0(p\Delta\nu_{line}x + 1), \tag{2.20}$$

where I_0 is the optical power at the absorption line center, x is the normalized frequency detuning, and p (in cm^{-1}) quantifies the slope of the laser power variation with frequency. For DFB lasers, p is negative due to their characteristic power decrease with frequency.

The transmitted light through a weakly absorbing medium is approximated by:

$$\begin{aligned} t(x) &= I_0(x)\exp\left[(-a(x)\right] \cong I_0(x)[1 - a(x)] \\ &= I_0(p\Delta\nu_{line}x + 1)[1 - a(x)]. \end{aligned} \tag{2.21}$$

where $a(x)$ is the wavelength-dependent absorption coefficient. This linearization assumes small absorption ($a(x) \ll 1$), which is valid for trace gas detection applications.

The frequency dependence of FM efficiency [34] necessitates distinct p coefficients for different modulation schemes: one for high-frequency sinusoidal modulation at angular frequency ω and another for the low-frequency ramp (angular frequency Ω) used to scan the laser wavelength across the absorption line. To account for this, two coefficients, p_ω and p_Ω, are defined to quantify the laser optical power variations under the two modulation modes.

For a Lorentzian lineshape, the detected IM-FM signal is expressed as:

$$s_{\mathrm{IM-FM}}(x) = I_0(p_\Omega \Delta\nu_{line} x_0 - p_\omega \Delta\nu_{line} m\cos\omega t + 1) \times \{1 - \frac{a_0}{1+[x_0 - m\cos(\omega t+\Psi)]^2}\}, \quad (2.22)$$

where p_Ω and p_ω in $1/\mathrm{cm}^{-1}$ represent laser modulation parameters, and Ψ denotes the IM-FM phase shift at frequency f. Building on this framework, the signal is reformulated to explicitly resolve harmonic contributions [32]:

$$s_{\mathrm{IM-FM}}(x) = I_0[\sum_{n=0}^{\infty} s_{np}(x)\cos n\omega t - \sum_{n=0}^{\infty} s_{nq}(x)\sin n\omega t]. \quad (2.23)$$

Here, the functions $s_n(x)$ in Eq. (2.23) describe the pure FM component, while $s_{np}(x)$ and $s_{nq}(x)$ correspond to the in-phase and quadrature amplitudes at the n-th harmonic frequency $n\omega$. This distinction arises

because combined IM-FM modulation generates harmonic terms with both amplitude (s_{np}) and phase (s_{nq}) dependencies. Explicit expressions for the first three harmonics under IM-FM modulation are derived as follows:

$$\begin{cases} s_{1p}(x) = I_\Omega(x)\cos\Psi\, s_1(x) - p_\omega \Delta v_{line}\dfrac{m}{2} \\ \qquad \times [2s_0(x) + \cos 2\Psi\, s_2(x)] \\ s_{1q}(x) = I_\Omega(x)\sin\Psi\, s_1(x) - p_\omega \Delta v_{line}\dfrac{m}{2} \\ \qquad \times [\sin 2\Psi\, s_2(x) \end{cases} \tag{2.24a}$$

$$\begin{cases} s_{2p}(x) = I_\Omega(x)\cos 2\Psi\, s_2(x) - p_\omega \Delta v_{line}\dfrac{m}{2} \\ \qquad \times [\cos\Psi\, s_1(x) + \cos 3\Psi\, s_3(x)] \\ s_{2q}(x) = I_\Omega(x)\sin 2\Psi\, s_2(x) - p_\omega \Delta v_{line}\dfrac{m}{2} \\ \qquad \times [\sin\Psi\, s_1(x) + \sin 3\Psi\, s_3(x)] \end{cases} \tag{2.24b}$$

$$\begin{cases} s_{3p}(x) = I_\Omega(x)\cos 3\Psi\, s_3(x) - p_\omega \Delta v_{line}\dfrac{m}{2} \\ \qquad \times [\cos 2\Psi\, s_2(x) + \cos 4\Psi\, s_4(x)] \\ s_{3q}(x) = I_\Omega(x)\sin 3\Psi\, s_3(x) - p_\omega \Delta v_{line}\dfrac{m}{2} \\ \qquad \times [\sin 2\Psi\, s_2(x) + \sin 4\Psi\, s_4(x)] \end{cases} \tag{2.24c}$$

These generalized expressions are applicable to both pure FM and combined IM-FM scenarios. In the pure FM case, the parameters are constrained to $p_\Omega = p_\omega = 0$ and $I_\Omega = 1$, simplifying the harmonic amplitudes to $s_{np}(x) = \cos n\Psi s_n(x)$ and $s_{nq}(x) = \sin n\Psi s_n(x)$. The resultant WMS signals for the first three harmonics, illustrated in **Fig. 2.8**, exhibit characteristic derivative-like line shapes due to the FM-induced phase dependence.

Lock-in detection further enhances signal resolution by enabling simultaneous measurement of in-phase (cos$n\omega t$), quadrature (sin$n\omega t$), and arbitrarily phased (cos($n\omega t$+Φn)) components. The detected signal at the n-th harmonic with a user-defined phase offset Φn is expressed as:

$$s_{n,\Phi}(x) = I_0[s_{np}(x)\cos\Phi_n + s_{nq}(x)\sin\Phi_n]. \qquad (2.25)$$

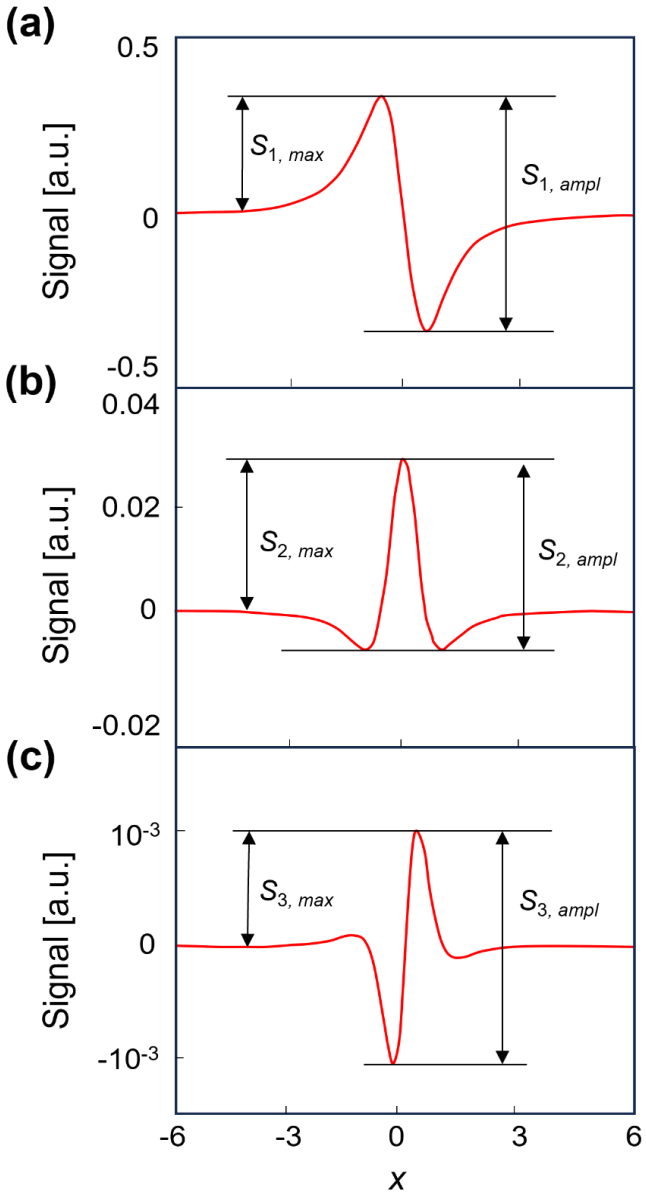

Figure 2.2. Theoretical WMS signals for the first three harmonics under pure FM with a modulation depth of m=0.1. The derivative-shaped profiles highlight the characteristic response of each harmonic, with $s_{n,\mathrm{max}}$ (peak magnitude) and $s_{n,\mathrm{ampl}}$ (peak-to-peak

amplitude) indicated.

In the regime of small modulation amplitudes ($m \ll 1$), the n-th harmonic signal deviates from a strict proportionality to the n-th derivative of the lineshape function s_n, as observed in pure FM. Instead, contributions from adjacent harmonic orders ($n \pm 1$) emerge, reflecting a superposition of lower- and higher-order derivatives. While conventional WMS theory posits that the n-th harmonic corresponds to the n-th derivative of the absorption line under the $m \ll 1$ condition, this relationship becomes distorted at a larger modulation depth. As illustrated in **Fig. 2.2**, the key metrics $s_{n,\max}$ and $s_{n,\mathrm{ampl}}$ exhibit a pronounced dependence on the modulation index m. For each harmonic, two distinct optimal modulation indices are identified: $m_{n,max}^{opt}$ maximizing $s_{n,\max}$, and $m_{n,ampl}^{opt}$, maximizing $s_{n,\mathrm{ampl}}$.

This analytical framework generalizes WMS to account for combined IM-FM effects, including arbitrary phase shifts (Ψ) inherent to diode laser current modulation. By decomposing the detected power into Fourier harmonics, the method isolates components such as the second harmonic ($2f_m$), which lies outside the flicker noise regime. A key advantage lies in its inherently calibration-free methodology: harmonic ratios depend solely on gas absorption properties rather than laser intensity, enhancing robustness for quantitative sensing [35].

2.3 Recent advances in optical fiber PAS gas sensing technologies

Over the past decades, many optical fiber acoustic sensors and devices, including intensity-modulated technology [36, 37], FBG-based technology [8, 38], interferometers [39-43], etc, have been demonstrated for PAS gas sensing. Notably, interferometer-based methods using cantilever, diaphragm, and hollow-core fiber (HCF) sensors are applicable for both optical fiber acoustic sensors and PAS systems. The working principles of optical fiber acoustic sensors and PAS gas sensors are broadly classified in **Fig. 2.3**. These technologies highlight the versatility and adaptability of sensor designs across different sensing applications. In the next section, optical fiber PAS gas sensors will be overviewed and their working principles and applications are introduced.

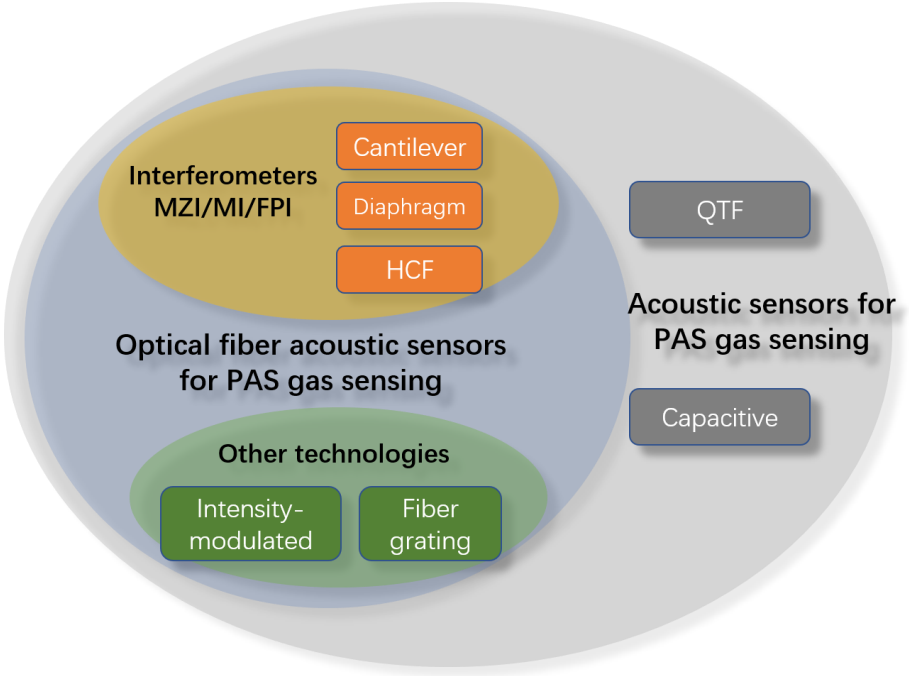

Figure 2.3. Classification of optical fiber acoustic sensors and those used for PAS gas sensing. HCF: hollow-core fiber; QTF: quartz tuning fork.

2.3.1 Non-interferometric optical fiber PAS gas sensors

(a) Intensity-modulated optical fiber PAS gas sensors

The most basic optoacoustic detectors are based on modulation of light intensity by partial lockage of light in illumination pathway, enabling compatibility with non-coherent or wide-spectrum light source. Because of its long-development history and stable performance, the intensity-modulated optical acoustic sensor has achieved commercial mass production [44]. Another type of early developed optical fiber acoustic sensors utilize the strain-optic effect, which means the refractive index of fiber material is modulated via the acoustic pressure induced strain. These intensity-based sensors utilizes an optical lossy structure such as U-bend [36] or coupler [37], whose optical loss is modulated by acoustic pressure. For example, Sheem et al. developed a sound detection device employing a near-field optical fiber coupler, as shown in **Fig. 2.4(a)**, analyzing signal attenuation across the 0.5 - 2 kHz spectrum while achieving detection thresholds as low as 52 dB relative to 10^{-6} N/m^2 [37].

For gas sensing purposes, Suchanek et al. devised layered graphene and mica structures as flexible beams into an opto-acoustic detector for simultaneous analysis of acetone, acetic acid, and methanol mixtures [45]. Acoustic-induced deformation in the beam alters the reflected laser intensity, synchronized with the vibrational frequency stimulated by a laser beam. A helium-neon light source paired with a quadrant photodetector

monitors beam displacement, as shown in **Fig. 2.4(b)**. The detection limits of methanol are 1.8 ppm, 0.8 ppm, 0.9 ppm, and 3.97 ppm for rectangular mica cantilever, circle mica cantilever, multilayer graphene cantilever, and condenser microphone, respectively.

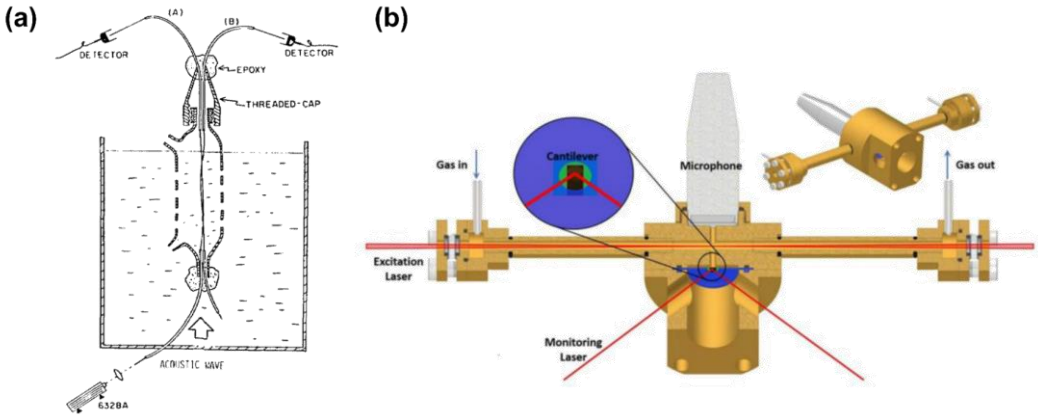

Figure 2.4. Acoustic sensors based on intensity modulation scheme. (a) Diagram illustrating the apparatus for assessing the sound-responsive characteristics of a bottle resonator design. Adapted from Ref. [37]. (b) Framework of a light-intensity-based PAS system employing composite mica-graphene microscale cantilevers. Adapted from Ref. [45].

Generally, intensity-modulated optical fiber acoustic detectors exhibit resilience in extreme thermal or chemically corrosive conditions because of their refraining from the use of electronic components. However, their SNR remains vulnerable to variations in light output and mechanical instabilities.

(b) Fiber grating-based optical fiber PAS gas sensors

Fiber grating-based acoustic sensors operate by detecting the shift of the peak resonant wavelength caused by strain-induced alterations to the

grating's effective refractive index and period. This approach can overcome the limitations of intensity-modulated sensors by decoupling signal detection from light source stability, thereby mitigating sensitivity to optical power variations [13]. For instance, LI et al. demonstrated a pliable sound detection device using a laterally modified fiber Bragg grating (FBG), as shown in **Fig. 2.5(a)** [38]. The sensor operates through acoustic wave-induced perturbations at the side-polished region of the FBG, which modulate its spectral response and induce a measurable wavelength shift, as illustrated in **Fig. 2.5(b)**. Different to traditional intensity-modulated detection systems, FBG's wavelength-encoded output inherently eliminates dependence on absolute optical power. Consequently, measurements remain unaffected under fluctuation in light intensity or transmission path losses, ensuring robust noise immunity. Additionally, the FBG's narrow spectral bandwidth enables two important benefits: (1) high-precision detection by minimizing crosstalk from ambient spectral interference, and (2) compatibility with wavelength-division multiplexing (WDM) technology, allowing scalable sensors within a single optical network.

Advances in FBG acoustic sensor technology have enabled implementations of novel PAS gas sensors. For instance, Wu et al. demonstrated a fully optical PAS platform utilizing thermally stabilized FBG sensors, processed through annealing to achieve operational stability

above 800°C [8]. As illustrated in **Fig. 2.5(c)**, the FBG sensor is integrated into a molybdenum membrane within a custom PA cell, where it transduces acoustic waves generated by gas absorption into measurable wavelength shifts. Experimental validation using the setup in **Fig. 2.5(d)** confirmed its efficacy for precise water vapor detection. Due to the FBG's resilience to extreme temperatures and mechanical stress, this design is suited for harsh industrial environments, such as Integrated Gasification Combined Cycle (IGCC) systems, where it enables real-time in situ monitoring of gas composition and properties.

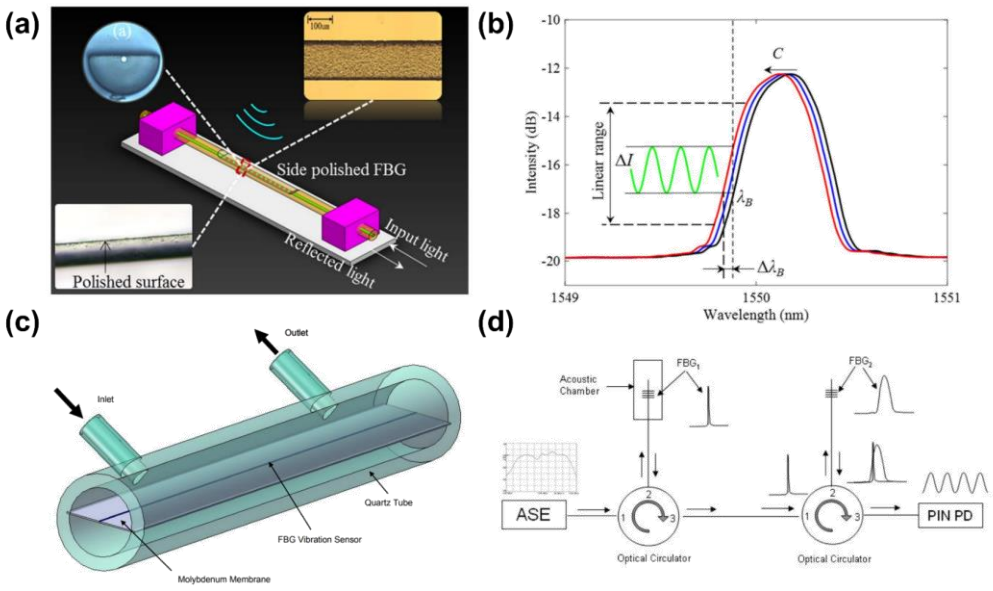

Figure 2.5. FBG-based acoustic sensor and its application in PAS gas sensing. (a) Schematic of a side-polished FBG acoustic sensor, where acoustic perturbations induce strain modulation at the polished region, translating mechanical vibrations into measurable wavelength shifts. (b) Experimental characterization of the FBG's spectral response under strain, demonstrating a linear relationship between applied strain and wavelength shift. This sensitivity forms the basis for detecting acoustic signals in PAS

systems. (a) and (b) are adapted from Ref. [38]. (c) The resonant acoustic chamber employed for gas sensing. (d) The experimental setup for the FBG vibration/acoustic sensor. (c) and (d) are adapted from Ref. [8].

To summarize, FBG acoustic sensors enable PAS systems to operate reliably in extreme conditions while supporting quasi-distributed detection scheme. These capabilities make the technology particularly valuable for scenarios requiring spatially resolved, real-time gas monitoring. Compared to previously discussed intensity-modulated sensors, its signal is less affected by environmental noise and light source stability. However, due to the need for precise fabrication of the FBGs and sophisticated interrogation techniques to detect wavelength shifts, FBG-based PAS gas sensors can be more complex and costly and are more suitable for applications requiring high sensitivity and remote sensing.

2.3.2 Optical fiber interferometric PAS gas sensors

Optical interferometers have become important tools for high-sensitivity acoustic detection in PAS, leveraging phase modulation rather than direct intensity measurements. The most prominent configurations are the Mach-Zehnder (MZI), Sagnac (SI), and Fabry-Pérot (FPI) interferometers.

MZI-based systems split light into reference and sensing arms, and acoustic signals induce phase shifts in the sensing path via strain or refractive index changes. Upon recombination, interference patterns encode acoustic information [46]. For example, Munir et al. [47]

demonstrated a fiber-optic MZI (**Fig. 2.6a**) in which a 10-m coiled fiber wrapped around a foil cylinder served as the sensing arm within a PA cell. This configuration achieved a detection limit of 50 ppb for gas contaminants at 500 mW pump power, corresponding to a minimum detectable absorption of 7×10^{-8} W/(cm$\sqrt{\text{Hz}}$), outperforming conventional electric microphones.

Sagnac interferometry based on Sagnac loops can enable unique multiplexing capabilities, though less common due to inherent sensitivity limitations [48]. Shi et al. [49] integrated an SI into a fiber laser system (**Fig. 2.6b**), combining it with an FPI for remote gas pressure sensing. The SI acted as a wavelength-selective filter, while the FPI transduced pressure-induced cavity length changes into spectral shifts. This hybrid design achieved a pressure sensitivity of 9.69 nm/kPa with a 45 dB SNR and a narrow 0.02 nm bandwidth, highlighting its potential for distributed sensing in harsh environments.

Optical fiber FPI enable simpler signal analysis and enhanced potential for miniaturization relative to the three previously mentioned interferometer configurations, owing to their elimination of components like couplers and reference arms. [13]. They could be further divided according to the formation of FP cavity with optical fiber, could be roughly divided by diaphragm [50-52] and cantilever [53]. The usages and applications are further discussed in the following sections.

(a) Diaphragm-based optical fiber-based PAS gas sensors

Diaphragm-based optical fiber FPI sensors have a simple structure that includes an air cavity and a flexible vibrating diaphragm mounted on the end-face of optical fiber. A typical configuration (**Fig. 2.6c**) employs a cavity formed between a fiber end-face with a vibrating polymer diaphragm (e.g., PVDF). Acoustic waves modulate the cavity length, altering the interference pattern formed by the light beams reflected from the fiber end-face and diaphragm. Demodulation of these shifts enables real-time monitoring and can achieve 61 mV/MPa sensitivity, a 2.3 kPa noise floor over 25 MHz, and flat frequency response up to 25 MHz [39].

Graphene-enhanced FPIs can further push sensitivity limit. As shown in **Fig. 2.6(d)**, a 100-nm graphene diaphragm-based FPI sensor can achieve 1100 nm/kPa deflection sensitivity and a noise-equivalent pressure of 60 μPa/Hz $^{1/2}$ at 10 kHz [40]. The design maintained a flat response from 0.2 kHz to 22 kHz, making it ideal for trace gas detection where sub-ppm resolution is critical.

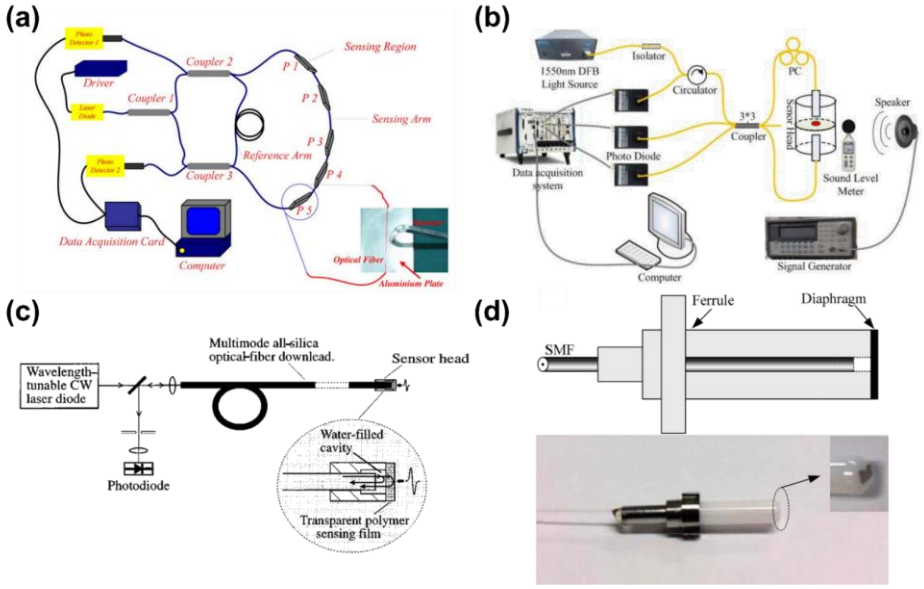

Figure 2.6. Interferometric optical fiber acoustic sensors. (a) Schematic of an optical fiber-based MZI for the analysis of contaminant species in gases. Adapted from Ref. [47]. (b) Schematic of a gas pressure sensor combining an SL and an FPI. PC: polarization controller. Adapted from Ref. [49]. (c) Schematic diagram showing the optical-fiber detection of ultrasound by optical fiber FPI. Adapted from Ref. [39] (d) The schematic diagram and photo of an optical fiber FPI-based gas sensor. Adapted from Ref. [40]

High quality vibrating diaphragms are essential in acoustic devices and directly influence their acoustic performance. A diverse array of membrane-based sensors have been adapted for pressure/acoustic sensing applications, traditionally utilizing inorganic and polymer materials such as silica [54, 55], silicon [56], silver [57, 58], stainless steel [59], chitosan [60], Parylene-C [61], etc. In recent years, diverse novel diaphragm materials have been employed to improve critical performance metrics such as stability and sensitivity in acoustic sensing systems, with high-performance two-dimensional (2D) nanomaterials being a focal point of

extensive research, such as graphene [40, 62], graphene oxide [63], MoS_2 [64], etc. In a fiber-tip diaphragm-based pressure sensor with limited diaphragm diameter, the mechanical properties and thickness of the diaphragm play a crucial role in enhancing sensitivity. Specifically, a diaphragm with a thinner profile and higher Young's modulus leads to increased pressure sensitivity.

Diaphragm-based optical fiber acoustic sensors have been widely used for PAS gas sensing. In 2013, Cao et al. [65] developed a fiber-tip photoacoustic sensor for trace gas analysis. As shown in **Fig. 2.7(a)**, this sensor features a compact hollow-cavity structure at the fiber end with a deformable polymer diaphragm (~2 μm thick) and millimeter-scale dimensions. Operated under non-resonant acoustic conditions, the system detected acetylene (C_2H_2) at concentrations as low as 4.3 ppm using an 8 mW laser. Later in 2017, subsequent work by Tan et al. [9] improved sensitivity by leveraging the mechanical resonance of a graphene diaphragm, as shown in **Fig. 2.7(b).** The sensor achieved a noise-equivalent pressure of 2.11 μPa/$Hz^{1/2}$ at 10.1 kHz and a C_2H_2 detection limit of 119.8 ppb with 123.9 mW pump power. Similarly, sliver diaphragm could also be used, as shown in **Fig. 2.7(c)** [66]. The sensor reduced the acetylene detection threshold to 0.87 ppb by volume.

In 2022, Xiao et al. introduced a highly sensitive all-optical PAS gas sensor incorporating a fiber-optic microphone (FOM) that employs Fabry-

Perot interferometry and ultrathin gold-chromium (Au-Cr) composite nanomembranes (330 nm thickness, 6.35 mm radius), as shown in **Fig. 2.7(d)** [67]. The sensor exhibited a stable frequency response between 300 and 900 Hz with less than 1 dB variation. In addition, a double channel differential T-type photoacoustic cell is designed and employed in the all-optical PAS gas sensor. The sensor is verified for CH_4 detection and the NNEA is 4.42×10^{-10} W•cm^{-1}•Hz$^{-1/2}$. The minimum detection limit (MDL) of 36.45 ppb is achieved with a 1 s integration time.

Diaphragm-based optical fiber PAS sensors have the advantages of high sensitivity and ease of fabrication for its simple structure. However, from the theoretical analysis, the sensitivity directly relates to its dimension due to thickness limited by material strength. In addition, the mechanical resonance of the diaphragm is usually hard to adjust, which limits the design flexibility for different applications.

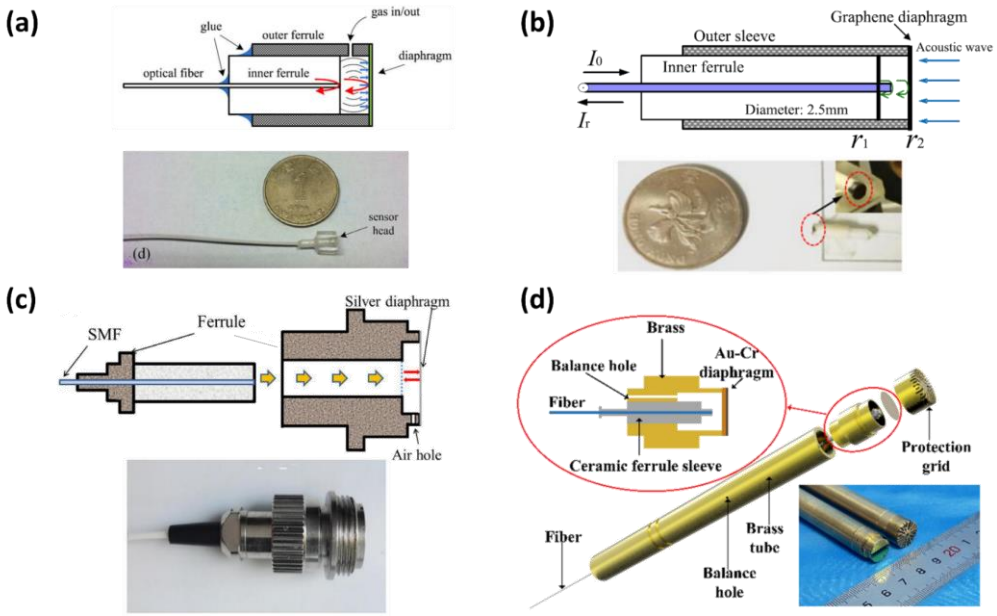

Figure 2.7. PAS gas sensors based on diaphragms. (a) Schematic diagram and photograph of the miniature fiber-tip sensor head. An EFPI is formed between the fiber end of the diaphragm. Adapted from Ref [65]. (b) Schematic diagram and photograph of the fiber FPI acoustic detector with a 2.5 mm-diameter-graphene diaphragm covering the endface of a sleeve. Adapted from Ref [9]. (c) Schematic and photo of a standard PC type fiber optic connector assembled with the proposed FPI-based sensor head. Adapted from Ref [66]. (d) The schematic structure and packaged samples of the proposed FOM. Adapted from Ref [67].

(b) Cantilever enhanced fiber-optic PAS sensors

Cantilevers have become a promising platform for PA detection. Their motion exhibits high linearity and a dynamic range surpassing conventional diaphragms, making them suitable for integration into optical fiber-based PAS systems, typically called as cantilever-enhanced PAS (CEPAS), where they act as transducers for PA signals. Cantilevers can operate in either static mode or resonant mode. In static mode, the displacement is directly proportional to the applied acoustic pressure. In

resonant mode, the vibration of the cantilever can significantly amplified. Compared to diaphragm-based sensors, the resonant frequency of cantilevers can be flexibly adjusted by tailoring geometries for sensing gases with different relaxation rates [27].

PAS gas sensors based on cantilever acoustic sensors have already been widely studied. For instance, Zhou et al. [68] developed a compact, high-sensitivity PA spectrometer employing an all-optical sensor, illustrated in **Fig. 2.8(a)**. The sensor features a micro-mirror fabricated from a borosilicate glass ribbon and suspended by a cantilever beam structure, integrated onto an external mounting platform. With a minimized gas cell volume of under 6 μL and a 23-mW excitation laser, the system achieved a NEC of 15 ppb for acetylene detection (at a 300 ms time constant). This performance corresponds to a normalized noise equivalent absorption coefficient (NNEA) of 7.7×10^{-10} Wcm^{-1} $Hz^{-1/2}$, demonstrating high sensitivity for trace gas analysis.

To enable all-optical passive methane (CH_4) detection in confined or harsh environments, Guo et al. [69] designed a miniaturized cantilever-enhanced fiber-optic photoacoustic sensor with a compact photoacoustic cell (PAC) featuring integrated diffusion channels, as shown in **Fig. 2.8(b)**. The system measures CH_4 concentration by detecting the vibrational amplitude of a stainless-steel cantilever, which is modulated by pressure induced by PA signal. Operating at the cantilever's resonant frequency, the

sensor achieved a methane detection limit of 0.32 ppm (60 s integration time) and a NNEA coefficient of 2.44 × 10^{-8} W·cm^{-1} $Hz^{-1/2}$.

Cantilever-based FPI acoustic sensors can utilize diverse signal interrogation methods. For instance, Li et al. [70] proposed a multiplexed FPI cantilever array in a fiber-optic photoacoustic gas sensor. The design employs dual fiber-optic interferometric cantilever microphones positioned symmetrically to enhance SNR. As depicted in **Fig. 2.8(c)**, the sensor incorporates a silicon cantilever (0.8 mm × 2 mm × 6 μm) with a resonant frequency of 2.44 kHz. This configuration achieved an NNEA of 2.5 × 10−9 cm^{-1}·W·$Hz^{-1/2}$ and a minimum detection limit (MDL) of 0.2 ppm for acetylene (C_2H_2) at 1-s averaging time. Similarly, Wang et al. [53] introduced a dual-comb photoacoustic spectroscopy (DC-PAS) system using a high-sensitivity fiber-optic cantilever sensor paired with a non-resonant PAC. As shown in **Fig. 2.8(d)**, the FPI sensor includes a stainless-steel cantilever (2 mm × 1 mm × 10 μm) with a resonant frequency of ~1 kHz. With 100 mW dual-comb laser power and 10-s averaging time, the sensor achieved an MDL of 860 ppb for detection of C_2H_2.

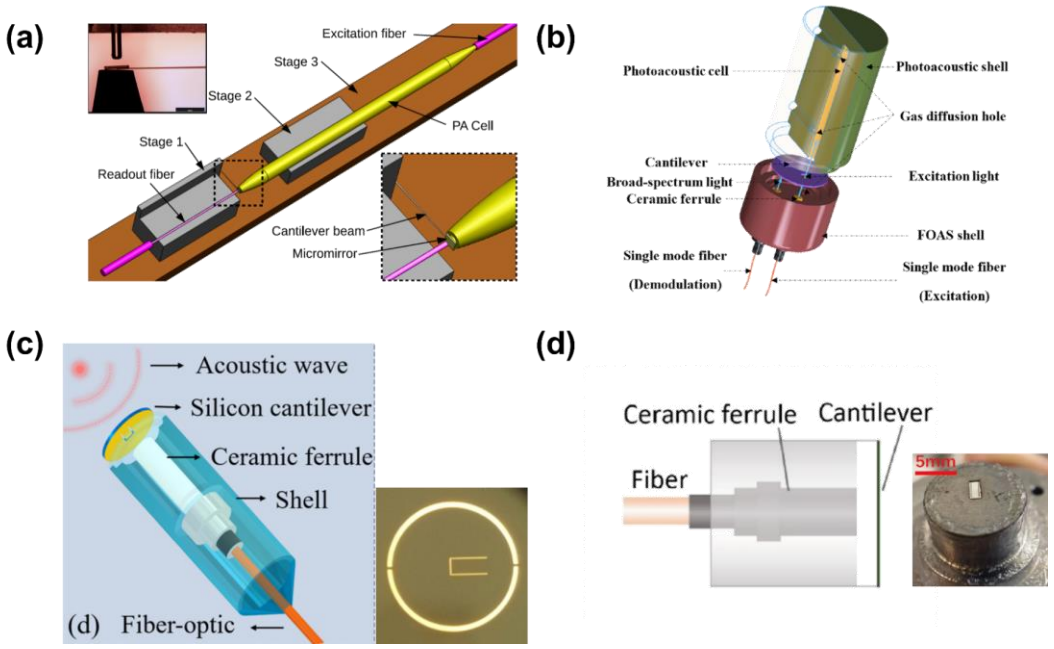

Figure 2.8. PAS gas sensors based on micro cantilever. (a) Schematic diagram of the PA sensor. Insets provide enlarged details of the micro-mirror alignment relative to the PA cell outlet and the fiber-optic readout assembly. Adapted from Ref. [68]. (b) Schematic structure of the cantilever-enhanced fiber-optic photoacoustic sensor. Adapted from Ref. [69]. (c) Sketch of the fiber-optic interferometric cantilever microphone. Adapted from Ref. [70]. (d) Schematic and image of FPI cantilever sensor head which is composed of a stainless-steel shell, a fiber, a ceramic ferrule and a cantilever. The cantilever is manufactured by laser micromachining technique and has a size of 2 mm × 1 mm × 10 μm. Adapted from Ref. [53].

2.4 Fabrication techniques for optical fiber sensors

In recent decades, many advanced manufacturing technologies have been applied to fabricate optical fiber sensors for enhancing compactness and sensitivity. Especially, various types of optical fiber-tip acoustic sensors have been developed for PAS gas sensing, overcoming the problems of size and ability of working in harsh environments. Typical fabrication

techniques include focused ion beam (FIB) etching, femtosecond laser ablation, lithography methods, two-photon lithography.

(a) Focused ion beam (FIB) milling

FIB milling is a cornerstone technique in MEMS fabrication, enabling direct, maskless patterning of various materials ranging from fiberglass to metals by selectively sputtering surface atoms with a high-energy ion beam [14]. This capability has spurred innovations in optical fiber tip engineering, where FIB's nanoscale precision was exploited to create functional microstructures.

For instance, Iannuzzi et al. demonstrated FIB-machined cantilevers on single-mode fiber tips (**Fig. 2.9a**), where a suspended cantilever aligned over the fiber core acts as a reflective element, transducing mechanical displacements into intensity-modulated optical signals [71]. André et al. combined FIB milling with chemical etching to fabricate fiber-tip Fabry-Perot interferometers (**Fig. 2.9b**) [72]. Their cantilever-based design achieved vibration sensitivity across 1 Hz – 40 kHz, with resonance frequencies up to 360 kHz, highlighting its potential for PAS gas detection working at high frequency.

Nevertheless, FIB milling technologies faces inherent limitations. First, achieving vertical sidewalls becomes challenging for larger etched structures, often resulting in unintended tapered geometries. Second, ion implantation into the low-conductivity fiber substrate remains unavoidable,

potentially altering material properties. Additionally, FIB's serial writing process is time-consuming, and its restricted field of view limits the scalability of fabrication steps [73].

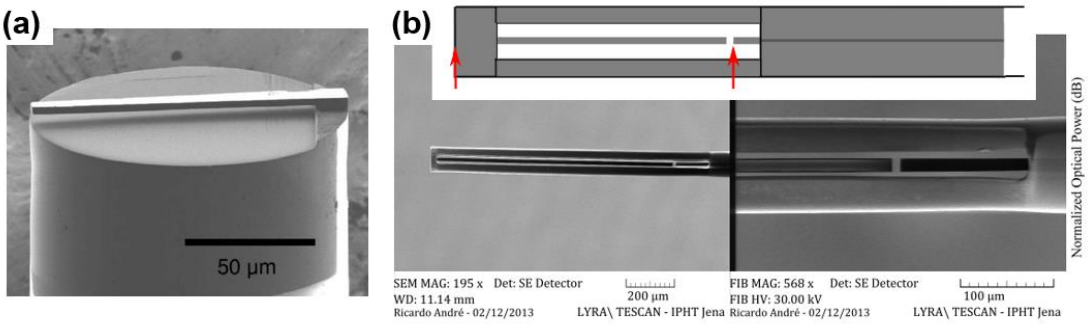

Figure 2.9. Fiber-top structures fabricated by FIB milling. (a) A fiber-top cantilever with dimensions of length ≈ 112 μm, width ≈ 14 μm, and thickness ≈ 3.7 μm. Adapted from Ref. [71]. (b) SEM image of a F-P structure fabricated by FIB-milled microwire. Adapted from Ref. [72].

(b) Femtosecond laser ablation

Femtosecond (fs) laser ablation has emerged as a high-precision technique for fabricating intricate 3D microstructures, leveraging ultra-short pulsed lasers to achieve localized material removal with minimal thermal damage to surrounding regions [14]. A notable application is the fabrication of fiber-top FP cavities [74, 75]. Dai et al. demonstrated this by patterning multilayer graphene (MLG) diaphragms using fs-laser ablation (**Figs. 2.9a–b**) [74]. By sculpting the MLG into a cross-shaped geometry, environmental pressure-induced signal fluctuations were reduced from 17 dB to 3.5 dB, significantly enhancing sensor stability. Beyond planar structures, fs-laser-assisted etching enables 3D microfabrication. Said et al.

produced fiber-top microcantilevers by irradiating silica fibers with a Ti:sapphire fs-laser, followed by hydrofluoric acid (HF) etching to selectively remove laser-modified regions (**Figs. 2.9c–d**) [76]. This method achieved a 90-minute fabrication time—faster than FIB milling—with higher material removal rates, suggesting scalability for mass production. However, the resulting cantilevers exhibited thicker profiles and rougher surfaces than FIB-machined counterparts, leading to light scattering losses that compromise signal fidelity.

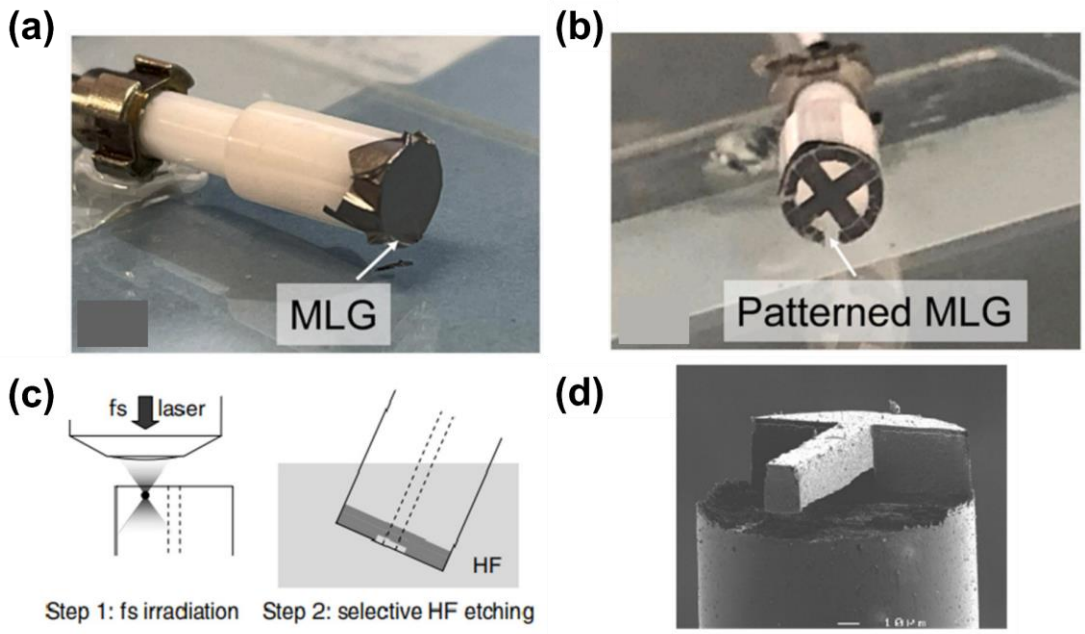

Figure 2.10. Fiber-top devices fabricated via femtosecond laser ablation. (a)–(b) Microscope images of an MLG-based Fabry-Perot cavity (a) before and (b) after fs-laser patterning. Adapted from Ref. [74]. (c) Fabrication workflow and (d) SEM image of a fs-laser-etched fiber-top microcantilever. Adapted from Ref. [76].

(c) Photolithography and digital UV exposure technologies

Lithography techniques represent a cornerstone of micro- and nanofabrication, offering unparalleled precision in patterning for

applications spanning nanoelectronics and photonics [14]. While optical fiber end-faces can theoretically serve as planar substrates for lithographic patterning, their ultra-small size and high aspect ratio introduce challenges that prevent direct adoption of standard processes.

A critical step in lithography is the deposition of a uniform, thickness-controlled photoresist layer. For instance, dip-coating simply immerse optical fiber in a photoresist solution followed by mechanical vibration to regulate uniformity [77]. Spin-coating, widely used for planar systems, achieves precise thickness control through adjustments in rotational speed and duration. However, the micrometer-scale cylindrical geometry and high aspect ratio of optical fibers disrupt the hydrodynamic conditions, rendering this method with challenges. Thus, improvements and modifications are required by using e.g. specialized rotating chucks [78]. Lastly, spray-coating deposits photoresist on the end face of optical fiber by a nozzle [79]. It could be integrated into the exposure system without the need to transfer the sample during the steps and enabled rapid fabrication of optical fiber-tip sensors.

Notably, digital UV exposure technologies have been developed to directly print various 2D/3D microstructures on the end-face of fiber-optic ferrule or optical fiber to develop miniature optical fiber sensors [79-82]. For instances, Wu et al. [80] demonstrated an innovative fiber-optic FPI pressure sensor featuring an in-situ printed microscale air cavity. Utilizing

a custom-developed optical 3D micro-printing system, the authors fabricated a suspended SU-8 diaphragm with integrated light-scattering structures directly onto a standard fiber end-face, forming a hermetically sealed F-P cavity (**Fig. 2.10a**). The resulting sensor exhibited a linear pressure response of 2.93 nm/MPa within a 0–700 kPa range and a temperature sensitivity of 38 pm/°C between 30°C and 65°C.

In 2020, Yao et al. [81] introduced a miniaturized fiber-optic acoustic sensor leveraging an optomechanical resonator fabricated *in situ* on a single-mode fiber end-face via optical 3D micro-printing. As illustrated in **Fig. 2.10(b)**, the device integrates a suspended polymer micro-disk—coaxially aligned with the fiber core—to form an FPI cavity, which concurrently functions as a micromechanical resonator for acoustic wave detection at a specific frequency. Experimental characterization revealed a sensitivity of 118.3 mV/Pa and a noise-equivalent acoustic signal level of 0.328 $\mu Pa/Hz^{1/2}$ at audio frequencies. Furthermore, resonance amplification enhanced sensitivity by 40.1-fold when acoustic frequencies matched the resonator's natural mechanical resonance. This ultracompact design combines miniaturization-driven broadband response with mechanically amplified sensitivity, positioning it as a transformative tool for precision acoustic sensing, biomedical imaging, and nondestructive testing applications.

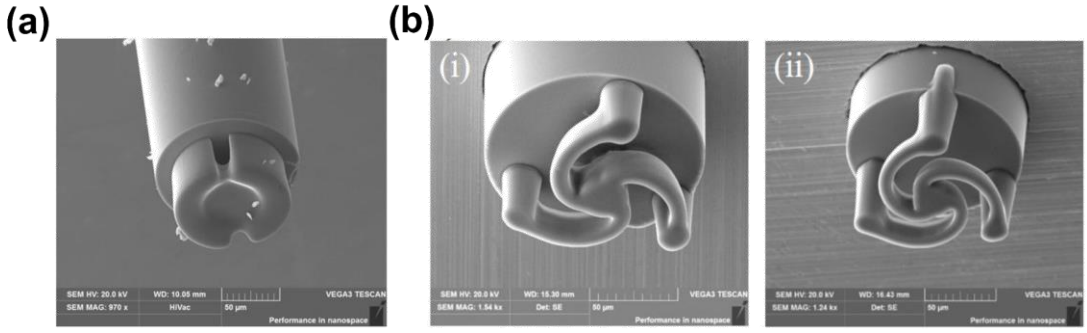

Figure 2.11. (a) Scanning electron micrograph of the fiber-tip Fabry-Pérot pressure sensor with integrated light-scattering features. Adapted from Ref. [80]. (b) SEM images of the fiber-top spirally suspended optomechanical microresonator. Adapted from Ref. [81].

Generally, lithography methods have enabled the fabrication of small-size high-performance optical fiber-tip sensors. The fabrication process has advantages of high resolution and ease of implementation.

(d) Two-photon lithography

Two-photon lithography (TPL), a form of multiphoton polymerization (MPP), is a nanofabrication technique capable of producing arbitrary 3D nanostructures with sub-100 nm resolution [83, 84]. A standard TPL system integrates a femtosecond laser for nonlinear photopolymerization, photoresist materials, a high-precision 3D nanopositioning stage, and computational control. The ultrashort pulses and high peak intensity of the focused femtosecond laser enable localized two-photon absorption exclusively at the focal volume, initiating resist polymerization.

Recent advances in TPL have expanded its ability in engineering optical fiber sensors. For instance, Liu et al. [85] demonstrated a gas-

sensitive "optical tentacle" comprising polymer micro-ring resonators 3D-printed onto a multicore fiber tip. As shown in **Fig. 2.12(a)**, three suspended micro-waveguides arranged in a nested configuration support symmetrically suspended micro-ring pairs, transforming the multicore fiber into a sensing platform for volatile organic compounds.

Further exemplifying TPL's versatility, Zou et al. [86] developed a fiber-tip polymer clamped-beam probe for micro-force sensing in biological environments (**Fig. 2.12b**). The sensor—comprising two bases, a clamped beam, and a probe—achieved a force sensitivity of 1.51 nm/μN^{-1}, a detection limit of 54.9 nN, and a dynamic range of ~2.9 mN, underscoring its suitability for delicate biomechanical measurements.

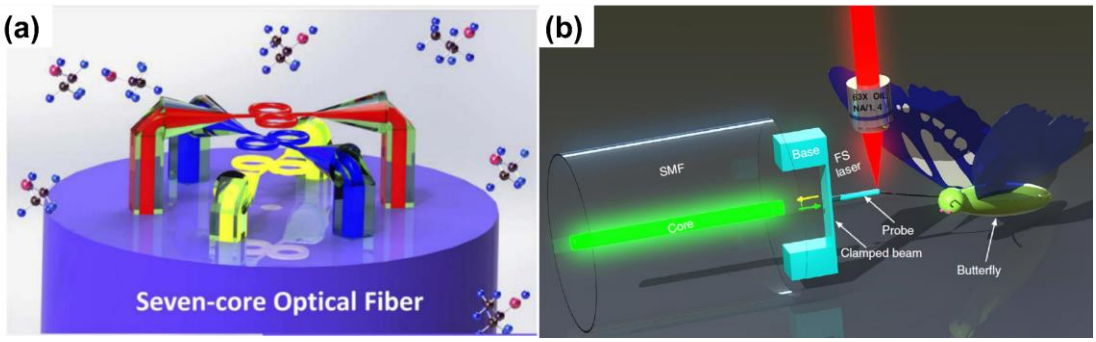

Figure 2.12. 3D direct-laser-writing-fabricated optical fiber-tip devices via TPL/MPL. (a) Schematic of the multicore fiber-tip "optical tentacle" with three sensing channels (red, blue, yellow: light propagation paths). Adapted from Ref. [85]. (b) Design of the clamped-beam micro-force sensor. Adapted from Ref. [86].

2.5 Summary

This chapter reviewed the theoretical and experimental foundations for optical fiber PAS gas sensors. First, we dissected the theories governing

PAS gas sensing, including laser absorption spectroscopy, photoacoustic signal generation, and wavelength modulation spectroscopy, to clarify their interplay in optimizing sensitivity and selectivity. Next, we systematically reviewed optical fiber PAS gas sensors, categorizing their operational principles and interrogating their underlying sensing mechanisms. This analysis provides critical insights into design considerations for next-generation PAS gas sensors, as explored in subsequent chapters. Finally, we overviewed cutting-edge micro- and nanofabrication methodologies for engineering optical fiber end-faces for sensing applications. Concurrently, we critically evaluate representative applications of these optical fiber-tip sensors, highlighting their potential in trace gas detection. Together, this synthesis bridges theoretical principles, fabrication techniques, and practical implementations for future advancements in small-size high-performance optical fiber PAS gas sensors.

Chapter 3

Miniature optical fiber photoacoustic spectroscopy gas sensor based on a 3D micro-printed ferrule-top optomechanical resonator

3.1 Introduction

Optical gas sensors based on laser absorption spectroscopy (LAS) have emerged as powerful trace-gas analysis tools due to their rapid response, high sensitivity and selectivity [1, 87, 88]. Among various LAS techniques, photoacoustic spectroscopy (PAS) stands out because of its robustness and precision. PAS employs an amplitude-modulated laser, precisely aligned to a gas's absorption wavelength, to generate low-amplitude pressure waves via non-radiative relaxation processes. These acoustic signals are then measured to quantify gas concentrations with high precision [13, 27, 89, 90]. Unlike conventional optical sensors requiring spectral analyzers, PAS employs cost-effective acoustic transducers (e.g., microphones), fostering its adoption as a competitive technology with compact configurations and broad sensor compatibility [91-96].

The performance of PAS gas sensors relies on their acoustic transducers' ability to detect weak photoacoustic (PA) signals. Resonant transducers are

commonly integrated to amplify signals via resonance, improving signal-to-noise ratio (SNR) and sensitivity. Quartz-enhanced photoacoustic spectroscopy (QEPAS) leverages the high-Q resonance of a quartz tuning fork to amplify acoustic energy generated by modulated laser excitation, thereby enabling detection of faint photoacoustic signals with enhanced signal-to-noise ratios [97, 98]. Its rapid response and high SNR have spurred numerous QEPAS adaptations for real-time gas monitoring [99-101]. However, piezoelectric readout mechanisms in traditional QEPAS hinder deployment in harsh or remote environments. Recent advances integrate fiber-optic Fabry-Pérot (FP) micro-interferometers with tuning forks for remote interferometric readout [102], yet centimeter-scale sensor dimensions limit use in confined spaces.

Fiber-optic PAS technologies address these limitations by combining laser delivery via optical fibers with miniaturized acoustic transducers, such as diaphragm [68, 103, 104] or cantilever [9, 67, 75]. Diaphragm-based FP cavities at fiber ends are prevalent; for example, Tan et al. utilized a graphene diaphragm nanoresonator to achieve 119.8 ppb C_2H_2 detection via resonance amplification [9]. However, diaphragm resonance customization remains challenging. Additionally, Fan et al. reported a graphite diaphragm sensor with a multi-pass Au film cell enabling ~50 ppb sensitivity but lacking resonant amplification [75].

Cantilever-enhanced PAS (CEPAS) offers greater resonance tunability.

Zhou et al. developed a fiber-optic CEPAS system using a borosilicate glass micromirror suspended on a >2-mm cantilever, achieving 15 ppb C_2H_2 detection at resonance [68]. Despite the high sensitivity, its multi-stage assembly yielded a bulky centimeter-scale device. In addition, Guo et al. demonstrated a silicon cantilever FP sensor combined with a non-resonant photoacoustic cell (PAC), attaining 199.8 ppt C_2H_2 sensitivity [104]. However, reliance on lengthy cantilevers and mechanical assembly resulted in a 2-cm-long sensor, impractical for compact settings.

These challenges are mitigated by a novel spirally-suspended optomechanical microresonator (OMR) [81], which reconciles miniaturization and sensitivity. Extending this concept, we propose a ferrule-top planar-spiral spring OMR (PSS-OMR) for PAS sensing [105, 106]. Fiber ferrules offer larger end-face areas than standard fibers, accommodating suspended disks for acoustic reception and elongated spiral arms for sensitivity tuning. Customizable PSS-OMRs fabricated via in-house 3D micro-printing exhibit adjustable resonance frequencies. Tests show the OMR-PAS sensor detects C_2H_2 at 45 ppb (~15 kHz) with 0.2-second response times, highlighting its potential for high-sensitivity, space-efficient gas monitoring.

3.2 Design and analysis of optical fiber PAS gas sensor based on a ferrule-top optomechanical resonator

Figure 3.1 illustrates our design of a fiber-optic acoustic sensor incorporating a ferrule-top PSS-OMR for PAS gas sensing. As depicted in **Fig. 3.1(a)**, positioning the OMR on the ferrule's end-face eliminates light-coupling components. The planar spiral spring features a central microdisk suspended by three spiral cantilevers, functioning as a semi-reflective surface to create a micrometer-scale Fabry-Pérot interferometer (FPI) with the input fiber's terminus. This configuration enables laser-interferometric PAS signal detection. The microdisk's reduced thickness mitigates parasitic cavity effects on the FPI's reflection spectrum. A critical innovation lies in the planar spiral spring design. Inspired by sensitivity-optimized microbeam architectures in accelerometers [107, 108], this geometry tailors the PSS-OMR's vibrational resonance modes. By extending effective cantilever length, the design boosts detection capabilities while maintaining compact dimensions for miniaturization.

Figure 3.1(b) shows a PAS microsystem, incorporating optical fiber OMR acoustic sensors, utilizing a pump laser spectrally aligned with the absorption signature of the target gas. This laser irradiates gas samples confined within a non-resonant photoacoustic cell (PAC), engineered to reduce volumetric gas requirements while amplifying pressure signals via thermoelastic expansion. Absorption by the target gas induces a low-

amplitude pressure wave, frequency-synchronized to the pump laser's modulation. Synchronizing this modulation with the PSS-OMR's resonant frequency induces oscillation, detected via a probe laser interrogating the FPI's reflectivity changes. This miniaturized architecture facilitates deployment in confined spaces and supports integration with multi-wavelength pump lasers for concurrent multi-gas analysis.

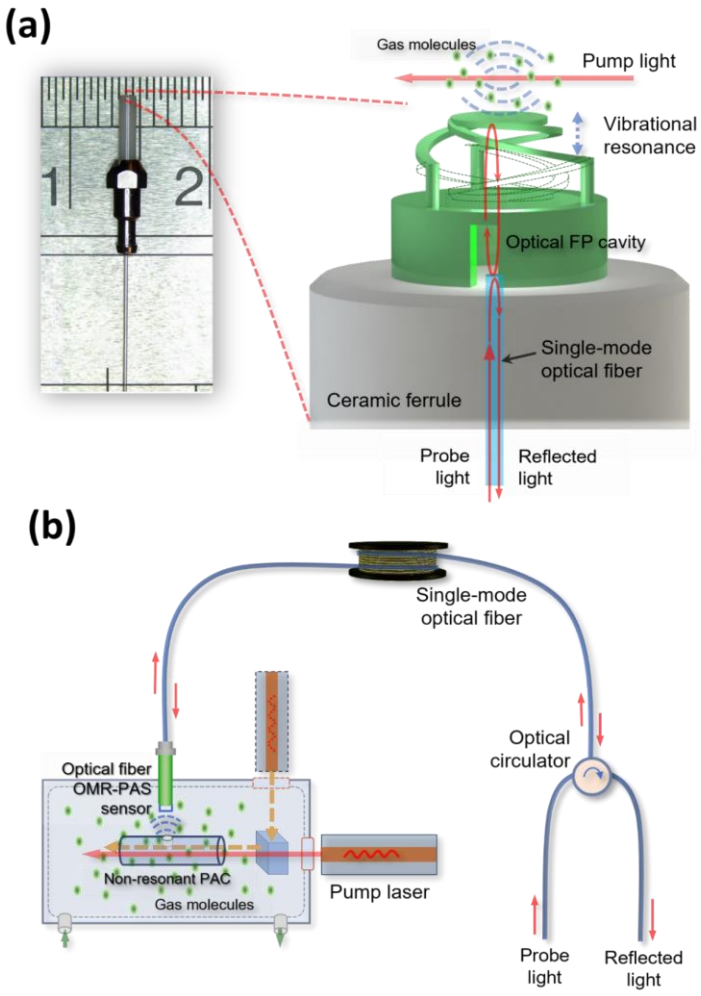

Figure 3.1. The architecture of a fiber-optic OMR-PAS gas sensor and its integration within a high-sensitivity trace-gas detection platform. (a) Cross-sectional schematic of the ferrule-top PSS-OMR, highlighting its 3D micro-printed planar-spiral spring resonator for acoustic signal transduction. (b) Operational diagram of the PAS microsystem, combining a non-resonant PAC with wavelength-selective laser

excitation to achieve low-volume gas sampling and signal amplification via acoustic resonance.

By approximating the spring arm as a linearized cantilever, the mechanical behavior of the PSS-OMR—anchored at one terminus with the opposite end restricted from rotational motion—can be analyzed via a pseudo-rigid-body model [109]. This simplification represents the spring arm as a fixed-guided beam functioning as a torsional spring. Under small-deflection assumptions, the displacement Δz of the central microdisk (corresponding to FP cavity length variation) in a three-arm spiral spring subjected to pressure P is expressed as:

$$\Delta z = \frac{PA \cdot L^3}{6K_\theta EI}, \tag{3.1}$$

where A denotes the microdisk's area, L is the spring arm length, $K\theta$ is the stiffness coefficient, E is Young's modulus, and I is the moment of inertia. Equation 3.1 reveals that pressure sensitivity depends on both the microdisk's surface area and the cubic relationship with spring arm length, underscoring the spiral design's critical role in enhancing sensitivity.

3.3 Numerical simulation results

3.3.1 Numerical simulation method

The mechanical behavior of the fabricated PSS-OMRs was evaluated computationally using COMSOL Multiphysics, an industry-standard finite element modeling tool. Material parameters for SU-8 resin, such as its

Young's modulus (3.4 GPa) and Poisson's ratio (0.22), were assigned in accordance with prior study [110]. Intrinsic material damping was incorporated as a loss factor within the simulations. Structural mechanics and acoustic pressure modules were employed to investigate the resultant deformations and natural frequencies of the PSS-OMR designs, respectively.

3.3.2 Numerical simulation results of optical fiber ferrule-top PSS-OMRs

Finite element analysis (FEA) was performed to evaluate the mechanical behavior of two PSS-OMR variants (PSS-OMR 1 and PSS-OMR 2) featuring distinct spring arm dimensions. Both configurations share an outer diameter of 400 μm, with central suspended microdisks measuring approximately 200 μm in diameter. Spring arm geometry was standardized to 25 μm in width and 10 μm in thickness, aligning with fabrication constraints of the employed optical 3D micro-printing technique. Arm lengths for PSS-OMR 1 and PSS-OMR 2 were specified as 434 μm and 328 μm, respectively. Simulations under 1 Pa static pressure revealed microdisk displacements of 17.1 nm (PSS-OMR 1) and 7.5 nm (PSS-OMR 2). **Figure 3.2** illustrates the cubic proportionality between spring arm length and displacement magnitude, consistent with Equation 3.1. Sensitivity further correlates with spring arm cross-sectional dimensions,

as evidenced by **Figure 3.3**, which maps displacement trends across varied arm widths and thicknesses under identical pressure. Frequency response analyses (**Figures 3.4(a)** and **3.4(d)**) demonstrate resonant displacements of 640 nm and 298 nm under 1 Pa excitation, highlighting the critical role of resonance amplification in sensitivity optimization.

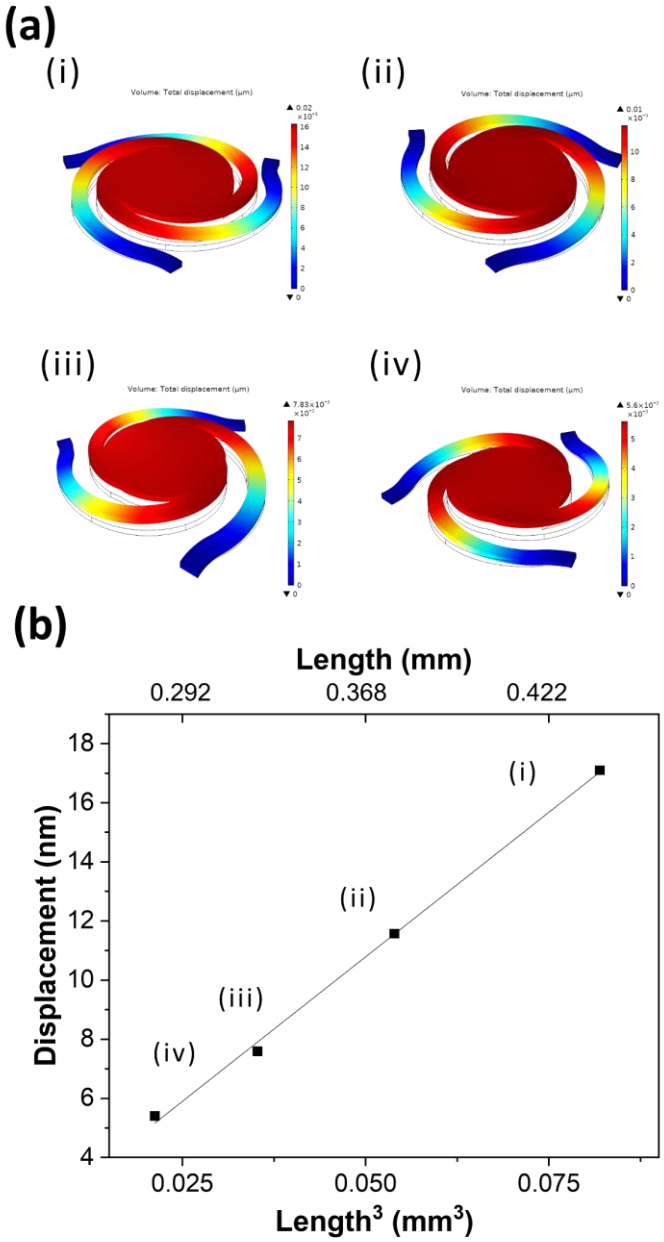

Figure 3.2. (a) Simulated deflection profiles across four ferrule-top optomechanical resonator (OMR) configurations under 1 Pa static pressure. Spiral cantilever lengths for the OMRs are 434 µm, 378 µm, 328 µm, and 277 µm. (b) Correlation between the

suspended microdisk's deflection and the cubic dependence on spiral cantilever length, validating Equation 3.1.

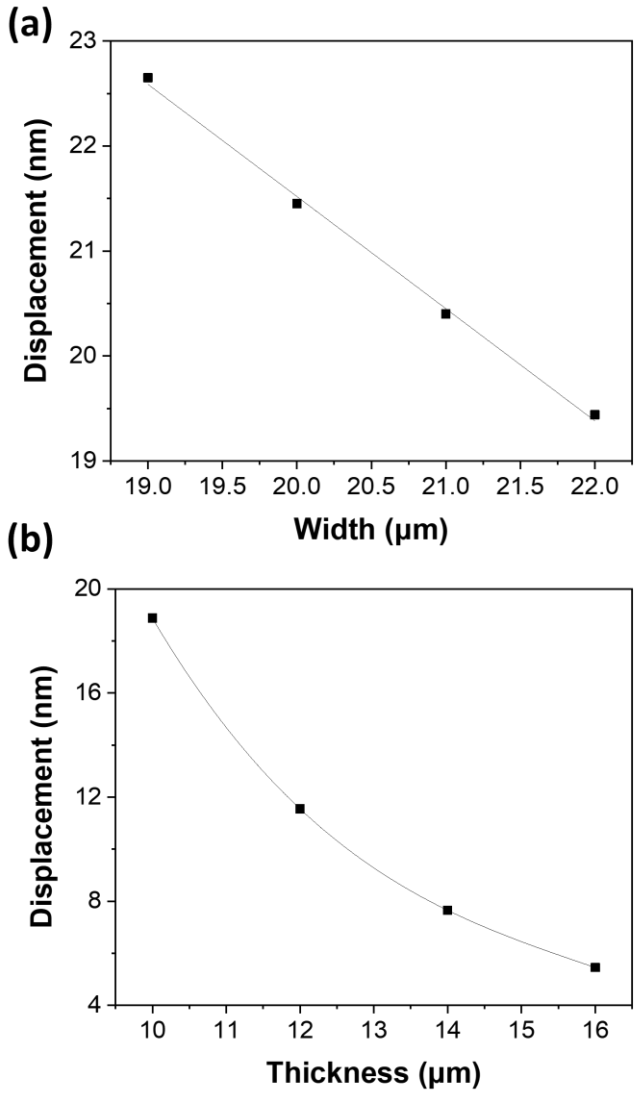

Figure 3.3. Simulated microdisk displacements in PSS-OMR sensors under 1 Pa acoustic excitation, analyzed for varying (a) spring arm widths and (b) thicknesses.

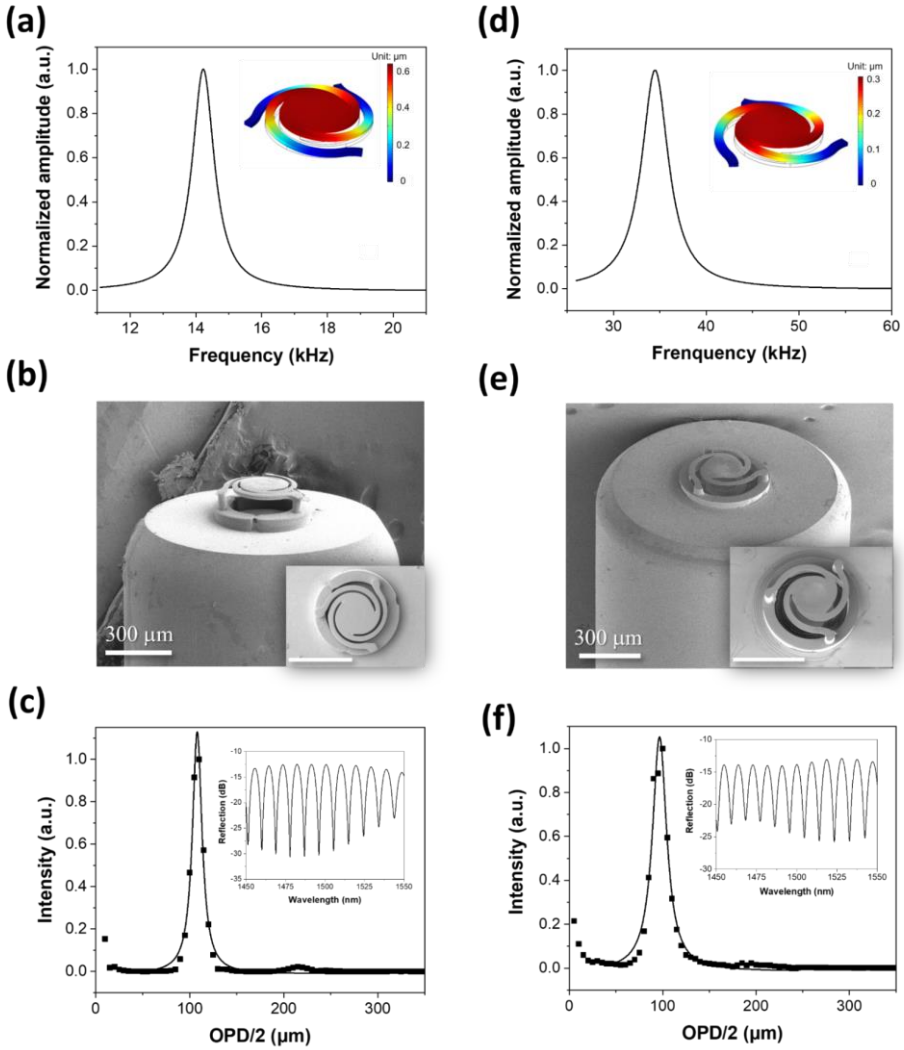

Figure 3.4. Numerical and experimental characterization of two fiber ferrule-top OMRs. (a) Simulated frequency-dependent displacement for OMR 1, with its primary resonant mode shown (inset). (b) SEM images of fabricated OMR 1. (c) Frequency-domain analysis (FFT) of OMR 1's reflection spectrum (inset). (d) Simulated frequency response of OMR 2, depicting its resonant mode (inset). (e) SEM images of OMR 2. (f) FFT-derived spectral response of OMR 2's reflection signal (inset).

3.4 Fabrication results

3.4.1 Photoresist materials for fabrication

The PSS-OMR sensors were fabricated via 3D micro-printing using SU-8 epoxy resin (acquired from HEXION Ltd.). To prepare the photoresist,

solid SU-8 was dissolved in cyclopentanone (sourced from Aladdin Scientific Corp.) at weight ratios of 15% (base layer) and 25% (top layer). The formulation included 4-octyloxydiphenyliodonium hexafluoroantimonate (OPPI, supplied by Arctom Scientific) and tributylamine (TBA, obtained from Meryer Chemical Technology Co., Ltd.), serving as the photoinitiator (4% by weight relative to SU-8) and inhibitor (0.5% by weight), respectively. For the upper layer fabrication, Tinuvin 234 (2-(2H-benzotriazol-2-yl)-4,6-bis(1-methyl-1-phenylethyl)phenol, procured from J&K Scientific), a UV-absorbing additive, was incorporated at 0.4% by weight relative to the SU-8 resin to modulate light absorption.

3.4.2 3D micro-printing processes

The manufacturing workflow, depicted in **Figure 3.5**, entails dual-layer fabrication steps for the base and top structures. Initially, SU-8 photoresist was deposited onto a fiber ferrule's end-face via dip-coating. The substrate underwent sequential soft-baking at 65°C (5 minutes) and 95°C (15 minutes) to remove residual solvents. Post-soft-baking, a machine vision-guided maskless UV lithography process defined structural patterns by projecting sliced 3D model data onto a DMD board, enabling real-time generation of UV exposure patterns. Post-exposure, the sample was thermally stabilized in a forced-air convection oven at 65°C for 40 minutes.

Development involved immersion in propylene glycol monomethyl ether acetate (PGMEA), followed by rinsing with methyl nonafluorobutyl ether ($C_5H_3F_9O$) to preserve the 3D geometry [111]. UV irradiation at 18.2 mW/mm² was applied for 150 s (base layer) and 300 s (upper layer), ensuring precise crosslinking.

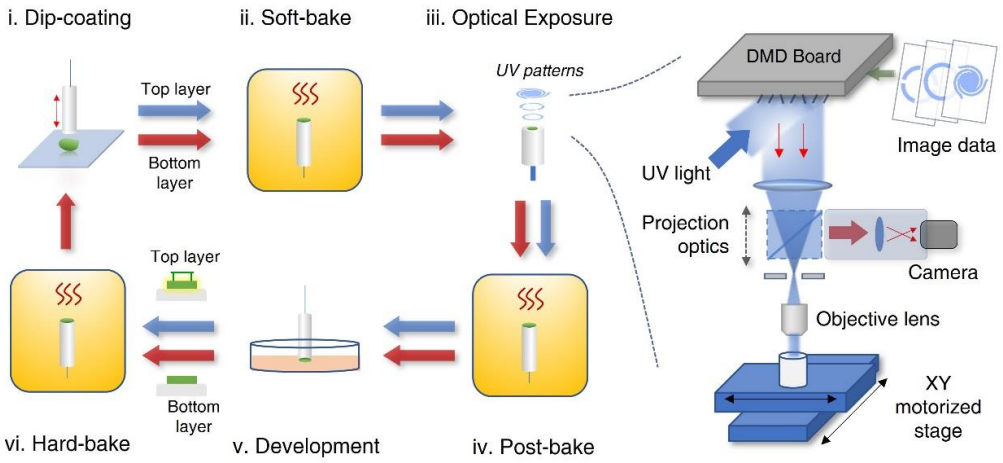

Figure 3.5. Outlines of the sequential steps of the optical 3D micro-fabrication protocol employed to produce fiber ferrule-top OMRs. This protocol involves two iterative cycles for constructing the foundational and upper layers. The right panel schematizes the mask-free UV lithography system integral to the patterning phase.

3.4.3 3D micro-printed optical fiber ferrule-top PSS-OMRs

The PSS-OMRs were fabricated on 1.25 mm-diameter fiber ferrules (10 mm length) via a customized 3D micro-printing technique [80, 81, 112], as detailed in prior sections. Scanning electron microscopy (SEM) images in **Figures 3.4(b)** and **3.4(e)** depict the completed PSS-OMR 1 and PSS-OMR 2. These devices comprise two strata: a base pedestal layer (enhancing FP cavity dimensions and mechanical stability) and an upper

functional layer housing the spiral spring and microdisk. Three support pillars ensure unrestricted oscillation of the spring-arm assembly, preventing contact with the pedestal. A faint circumferential recess is visible on thinner microdisks, see the insets in **Figures 3.4(b, d)**, attributable to fabrication-induced topography. The fabricated OMRs exhibit dimensional fidelity to design specifications, with smooth surfaces and precise alignment between upper layers and pedestals. This alignment positions the microdisk directly above the fiber core, forming stable FP microcavities—a testament to the 3D micro-printing system's precision in submillimeter-scale structural engineering.

Insets in **Figures 3.4(c)** and **3.4(f)** display interferometric reflection spectra of PSS-OMR 1 and PSS-OMR 2, acquired using a broadband illumination source and a high-resolution optical spectrum analyzer (0.1 nm resolution). Peak fringe visibilities reach ~18 dB (PSS-OMR 1) and ~14 dB (PSS-OMR 2) across their respective spectral ranges. Fast Fourier transform (FFT) analyses of these spectra, shown alongside, reveal cavity lengths approximating 100 μm for both devices—consistent with theoretical predictions.

3.5 Testing of optical fiber OMR-PAS gas sensors

3.5.1 Experimental setup for testing the acoustic responses of optical fiber PSS-OMRs

The acoustic performance of the fabricated fiber-optic PSS-OMRs was evaluated in air using a custom-built apparatus illustrated in **Figure 3.6**. Acoustic excitation across frequencies up to 60 kHz was produced by a piezoelectric loudspeaker (Kemo L010) controlled by a waveform generator. While spectral demodulation techniques [113, 114] are viable for FPI sensor interrogation, a narrow-linewidth laser system operating at a reflection spectrum quadrature point was selected for high-frequency signal detection via intensity demodulation. The laser wavelength was stabilized at a quadrature position of the PSS-OMR's reflection spectrum to maximize sensitivity. Reflected light was routed through an optical circulator to a photodiode (PD), where optical intensity fluctuations were converted to voltage signals for analysis on a digital oscilloscope. The PD's bandwidth was configured for 1 kHz–100 kHz operation. A reference microphone (Brüel & Kjær 4939), positioned adjacent to the PSS-OMR sensor, provided acoustic pressure calibration. To minimize ambient noise interference, all components—including the loudspeaker, sensor, and microphone—were housed within a soundproof enclosure.

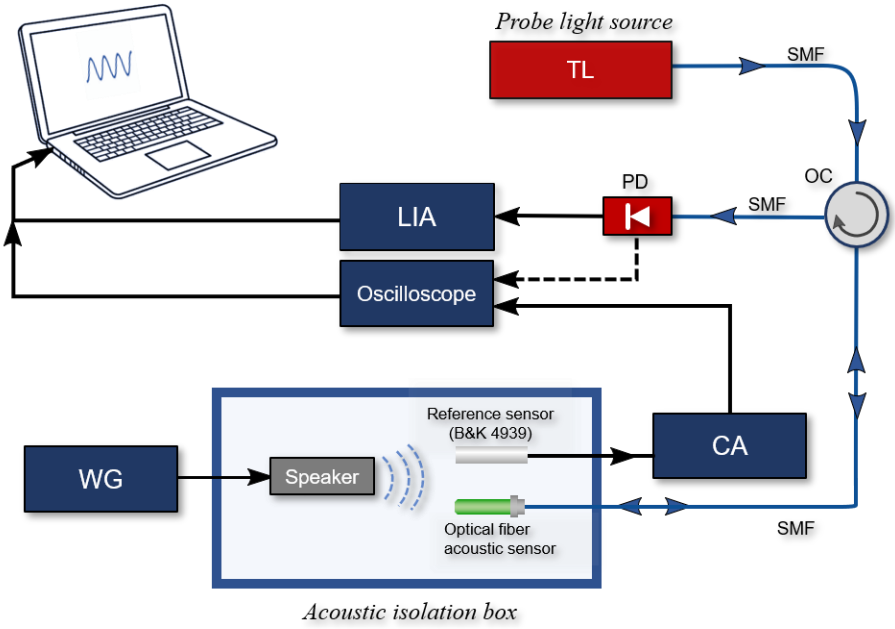

Figure 3.6. Schematic of the fiber-optic OMR acoustic testing platform. TL: tunable laser; SMF: single-mode fiber; OC: optical circulator; PD: photodetector; LIA: lock-in amplifier; WG: waveform generator; CA: signal conditioning amplifier.

3.5.2 Experimental setup for testing optical fiber OMR-PAS gas sensors

The developed fiber-optic OMR-PAS gas sensor was tested using a pump-probe configuration, as depicted in **Figure 3.7**. A 1533-nm distributed feedback (DFB) laser served as the pump source, amplified by an erbium-doped fiber amplifier (EDFA). A single-wavelength laser has been selected to target a distinct *P*(13) absorption line of C_2H_2 so as to ensure the high specificity and depress the potential interference from other gases during gas sensing. The probe beam was produced by a tunable semiconductor laser (TSL) with an adjustable wavelength range of 1500–

1630 nm. A proportional-integral-derivative (PID) controller stabilized the interferometer at quadrature by regulating the probe wavelength. This wavelength was incrementally scanned across the P(13) absorption line of acetylene (C_2H_2) while being sinusoidally modulated at ~7.35 kHz to induce acoustic excitation. Gas concentration quantification utilized wavelength modulation combined with second-harmonic (2*f*) detection. The photoacoustic signal was demodulated using a lock-in amplifier (Zurich Instruments MFLI, 0–500 kHz bandwidth).

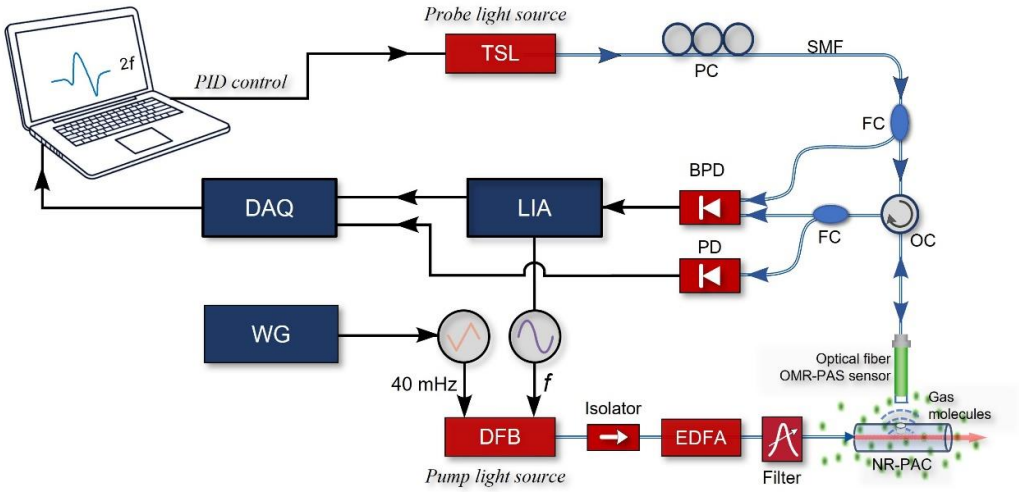

Figure 3.7. Schematic of the experimental setup for assessing the fiber-optic OMR-PAS gas sensor performance. TSL: tunable semiconductor laser; PC: polarization controller; SMF: single-mode fiber; FC: fiber coupler; OC: optical circulator; PD: photodetector; BPD: balanced photodetector; LIA: lock-in amplifier; DAQ: data acquisition system; WG: waveform generator; DFB: distributed feedback laser; EDFA: erbium-doped fiber amplifier.

3.5.3 Preparation of gas samples

Gas mixtures of varying concentrations were formulated by blending calibrated reference gases (at ambient temperature and atmospheric

pressure) using two mass flow controllers. For concentrations lower than 103 ppm, dilutions were created by mixing a 103 ppm C_2H_2 standard with high-purity nitrogen (N_2). Higher concentrations (>10^3 ppm) were achieved by diluting a 1000 ppm C_2H_2 standard with N_2.

3.5.4 Results of the PSS-OMRs' acoustic responses

Figure 3.8 experimentally characterizes the acoustic performance of two prototype PSS-OMR variants (designated PSS-OMR 1 and PSS-OMR 2). Frequency response spectra in **Figs. 3.8(a)** and **3.8(d)** reveal primary resonant frequencies of approximately 14.7 kHz and 34.5 kHz for PSS-OMR 1 and PSS-OMR 2, respectively. Subfigures include comparative overlays of finite-element simulations and empirical data, demonstrating strong agreement that validates experimental rigor. Lorentzian analysis of the resonance peaks yields quality factors (Q-values) of ~16.4 and ~10.8 for the two sensors, derived through experimental characterization.

Time-domain signal profiles for both PSS-OMRs, captured at their respective resonant frequencies, are illustrated in **Figs. 3.8(b)** and **3.8(e)**. Corresponding acoustic pressure-amplitude relationships (**Figs. 3.8(c)** and **3.8(f)**) demonstrate linear proportionality between signal amplitude and applied pressure. PSS-OMR 1 exhibits a resonant sensitivity of ~870 mV/Pa at 14.7 kHz, contrasting sharply with its non-resonant sensitivity of 8.0 mV/Pa at 30 kHz—revealing a substantial sensitivity enhancement

factor of ~109 due to micromechanical resonance.

Figure 3.9 analyzes the output waveform and corresponding spectral characteristics of PSS-OMR 1 under a 0.3 Pa sinusoidal acoustic stimulus at 14.7 kHz. The system achieves a SNR of 39.6 dB, corresponding to a noise-equivalent sensitivity of approximately 147 μPa/Hz$^{1/2}$. For PSS-OMR 2, resonant-frequency sensitivity reaches 103.4 mV/Pa, compared to 3.1 mV/Pa under non-resonant conditions—demonstrating a 33-fold sensitivity amplification through resonance-enhanced signal transduction.

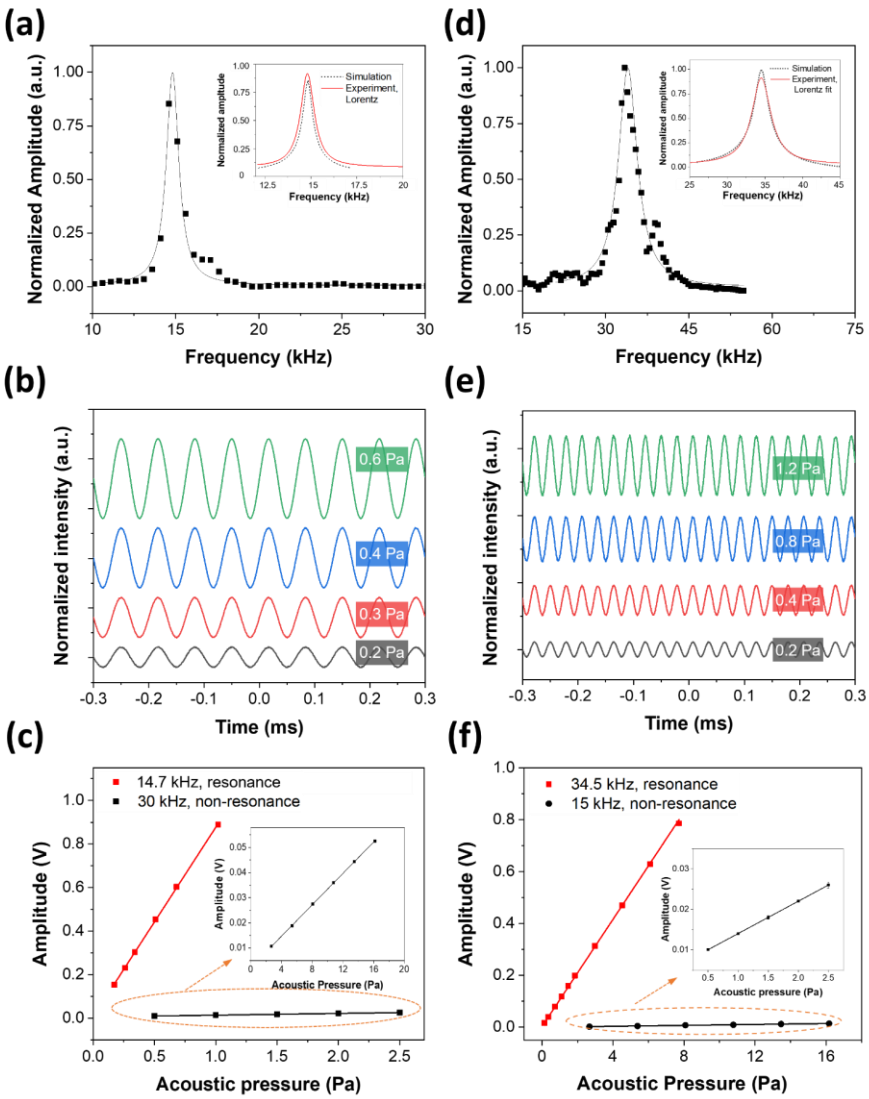

Figure 3.8. Acoustic performance characterization of the two fabricated fiber-optic OMRs. (a) Frequency-dependent response of OMR 1 under 0.2 Pa acoustic excitation; inset depicts comparative analysis of experimental and simulated data. (b) Temporal waveforms of OMR 1 at resonance (14.7 kHz) under acoustic pressures of 0.2, 0.3, 0.4, and 0.6 Pa. (c) Amplitude comparison for OMR 1 operating at resonant (14.7 kHz) versus non-resonant (30 kHz) frequencies. (d) Frequency response of OMR 2 under 0.5 Pa excitation; inset highlights simulation-experiment correlation. (e) Time-domain signals of OMR 2 at resonance (34.5 kHz) under pressures of 0.2, 0.4, 0.8, and 1.2 Pa. (f) Sensitivity comparison for OMR 2 at resonant (34.5 kHz) and non-resonant frequencies.

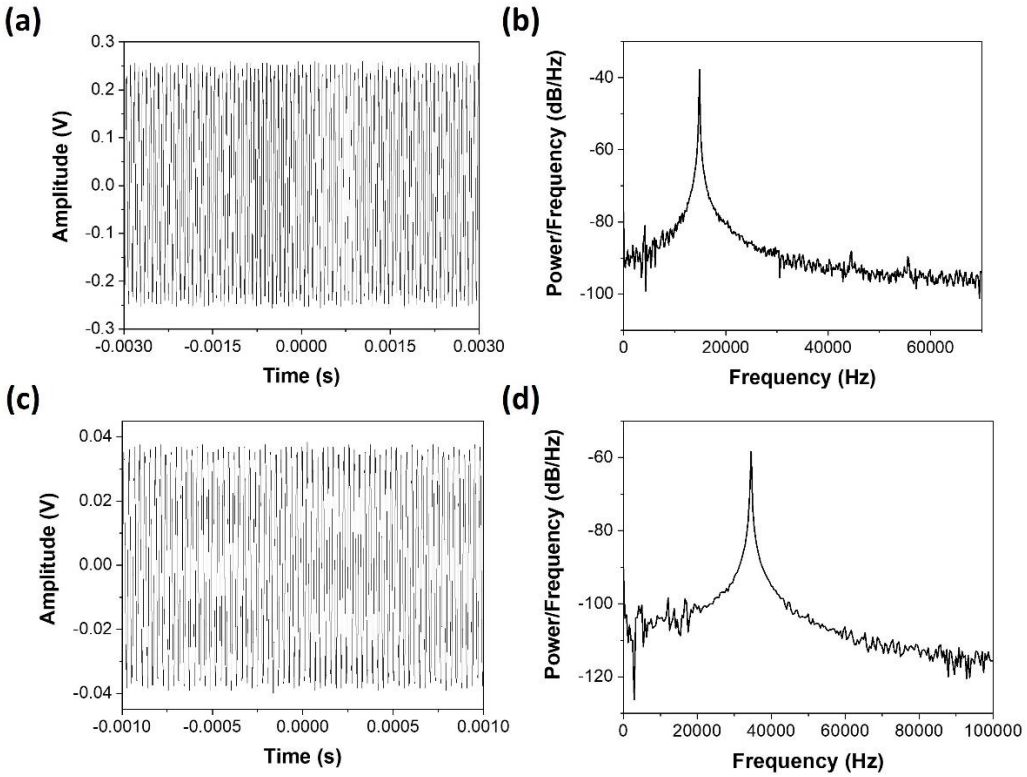

Figure 3.9. Resonant-mode output profiles and spectral analysis of fiber-optic OMR sensors. (a) Temporal response of OMR 1 to 0.3 Pa acoustic excitation at 14.7 kHz. (b) Power spectral density (PSD) of the signal in (a), demonstrating a 39.6 dB SNR. (c) Temporal output of OMR 2 under 1 Pa excitation at 34.5 kHz. (d) PSD of the signal in (c), confirming frequency-domain performance.

3.5.5 Results of trace-gas detection

The fiber-optic PAS gas sensor, incorporating PSS-OMR 1, was evaluated via the setup in **Figure 3.7**. A non-resonant photoacoustic cell (PAC) minimized gas consumption while confining acoustic signals. The PAC comprised a 5-mm-long silica capillary (inner diameter: ~600 μm) with a femtosecond-laser-drilled central aperture (~500 μm diameter), yielding a total volume of ~1.4 μL, which is 10 to 100 times smaller than conventional PACs. Open-pipe model and numerical simulations confirmed that the PAC's resonant frequency is about 66 kHz, which is intentionally offset from the OMR's fundamental resonance to prevent acoustic coupling.

Detection limits were assessed using 1000 ppm C_2H_2/N_2 mixtures. **Figure 3.10(a)** plots second-harmonic (2f, 14.7 kHz) lock-in signals acquired during wavelength scans across the C_2H_2 P(13) line at varying pump powers (lock-in parameters: 200 ms time constant, 18 dB/oct slope, 0.469 Hz bandwidth). **Figure 3.10(b)** illustrates the linear increase in PAS signal amplitude with pump power. System noise, measured under ambient air exposure with fixed pump wavelength, showed negligible dependence on pump power (**Figure 3.10(c)**), with 1σ noise levels remaining consistent. At 390 mW pump power, a signal-to-noise ratio (SNR) of ~4776 (1 s integration) corresponded to a noise-equivalent concentration (NEC) of 209 ppb and noise-equivalent absorption (NEA) of ~2.2×10^{-7} cm^{-1}. Higher

pump powers could further reduce detection thresholds.

As shown in **Fig. 3.10(d)**, Allan-Werle deviation analysis [12, 115, 116] conducted based on 1-hour noise data, revealed a minimum NEC of 45 ppb C_2H_2 (NEA: 4.7×10^{-8} cm^{-1}) at 280 s integration. NECs of 206 ppb (10 s) and 68 ppb (100 s) were observed at shorter integration times. All tests were conducted at ambient temperature; temperature-dependent PAS signal variations (depending on gas properties and thermal dynamics [117, 118]) need further evaluation for the gas sensing at non-ambient conditions. On the other hand, humidity effect is negligible due to H_2O and C_2H_2 do not have significantly overlapping absorption lines near 1531 nm, and H_2O does not affect the relaxation path of C_2H_2. [119].

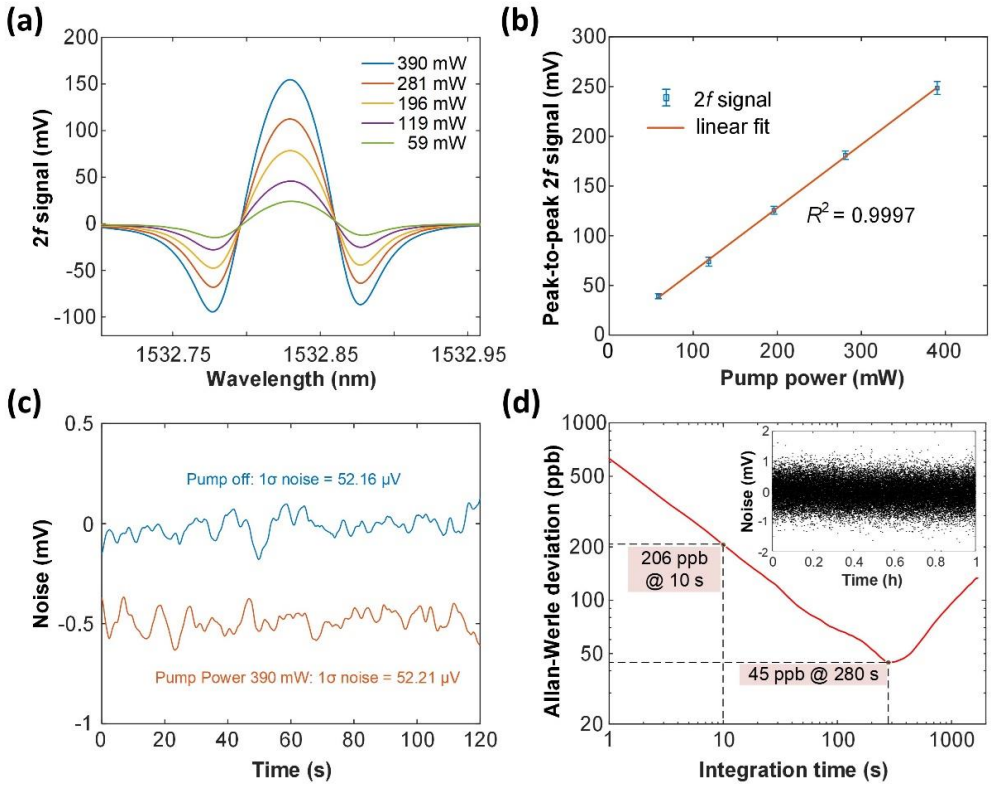

Figure 3.10. Detection limit characterization outcomes. (a) Acquired second-harmonic

(2f) signals for 1000 ppm C_2H_2 under varying pump power levels (detection bandwidth: 0.469 Hz). (b) Linear correlation between 2*f* signal amplitude (peak-to-peak) and pump power. Error bars represent standard deviation (S.D.) from five measurements, magnified 15× for visibility. (c) Comparative 1σ noise levels at the P(13) absorption line under pump-off (blue) and pump-on (~390 mW, orange) conditions (bandwidth: 0.094 Hz). The orange trace is vertically offset by 0.5 mV for clarity. (d) Allan-Werle variance analysis derived from 1-hour noise data (bandwidth: 3.125 Hz), illustrating stability over integration intervals.

The dynamic range of the fiber-optic OMR-PAS sensor was evaluated by introducing C_2H_2 gas mixtures of varying concentrations into the photoacoustic cell (PAC). **Figure 3.11(a)** illustrates the linear correlation between the second-harmonic (2f) signal amplitude (peak-to-peak) and C_2H_2 concentration (10–1000 ppm) at a fixed pump power of 390 mW. Representative 2f signals for low concentrations (10, 26, 55, 78 ppm) are shown in the inset. Temporal response characteristics were quantified by rapidly cycling 1000 ppm C_2H_2 at a flow rate of 265 sccm. **Figure 3.11(b)** displays normalized 2f signal dynamics during gas unloading (4.3 s) and reloading (8.7 s), with rise/fall times (90%–10% thresholds) of 0.20–0.26 seconds. The abrupt signal shift during flow transitions arises from gas-induced perturbations to the interferometer's operating point.

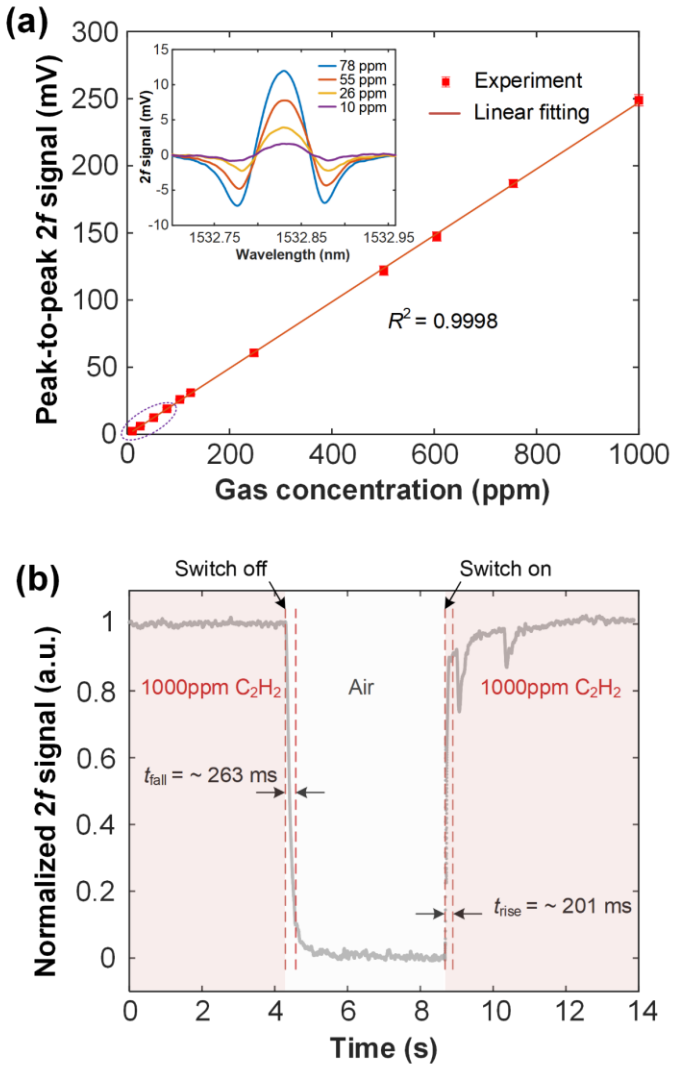

Figure 3.11. (a) Dynamic range analysis: 2f signal amplitude vs. C_2H_2 concentration. Error bars denote standard deviation (n=5), magnified 10× for visibility. Inset: 2f spectra for low-concentration samples (detection bandwidth: 0.094 Hz). (b) Normalized temporal response to 1000 ppm C_2H_2 flow modulation (bandwidth: 9.4 Hz).

3.5.6 Discussion

Non-resonant PACs play a part in enhancing PAS signals via confining acoustic waves unidirectionally [104]. The effect was tested by using copper and silica glass PACs (**Figure 3.12**) with identical geometries (see **Table 3.1**). Experiments involved continuous injection of 1000 ppm C_2H_2

into each PAC under ~7.35 kHz modulation.

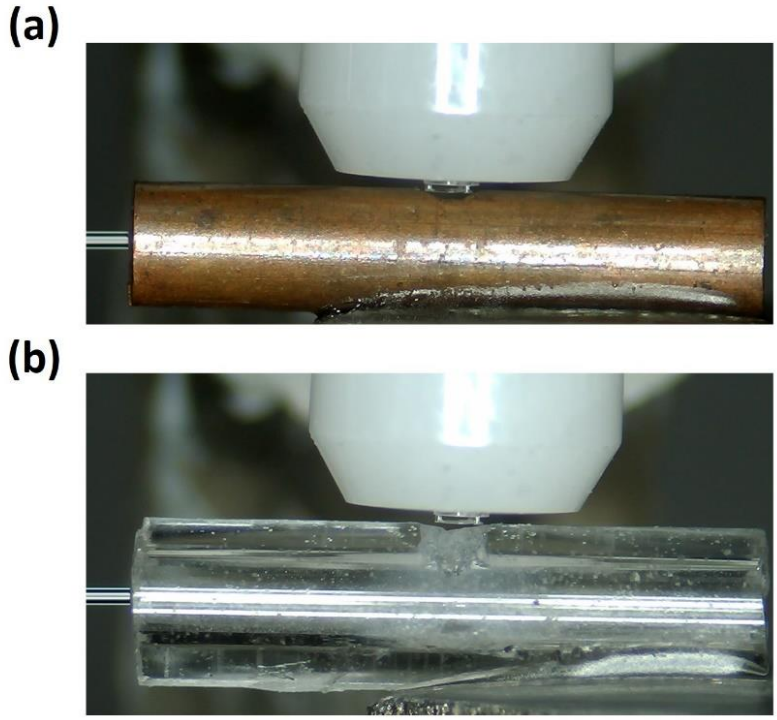

Figure 3.12. Non-resonant PAC prototypes: (a) 5-mm copper tubes; (b) 5-mm silica glass capillary.

Table 3.1. Geometric parameters of tested PACs.

Material	Inner diameter (mm)	Outer diameter (mm)	Length (mm)	Cell volume (μL)
Copper	0.6	1	5	1.4
Glass	0.6	1.4	5	1.4

As shown in **Fig. 3.13(a)**, both PACs amplified PAS signals by ~5× compared to direct detection. Minor signal variations between materials are likely resulted from inner wall fabrication inconsistencies. However, copper PACs introduced a notable background noise floor, see **Fig. 3.13(b)**, attributed to near-infrared light absorption by the metal. Silica glass PACs, being optically transparent in this range, exhibited significantly lower noise.

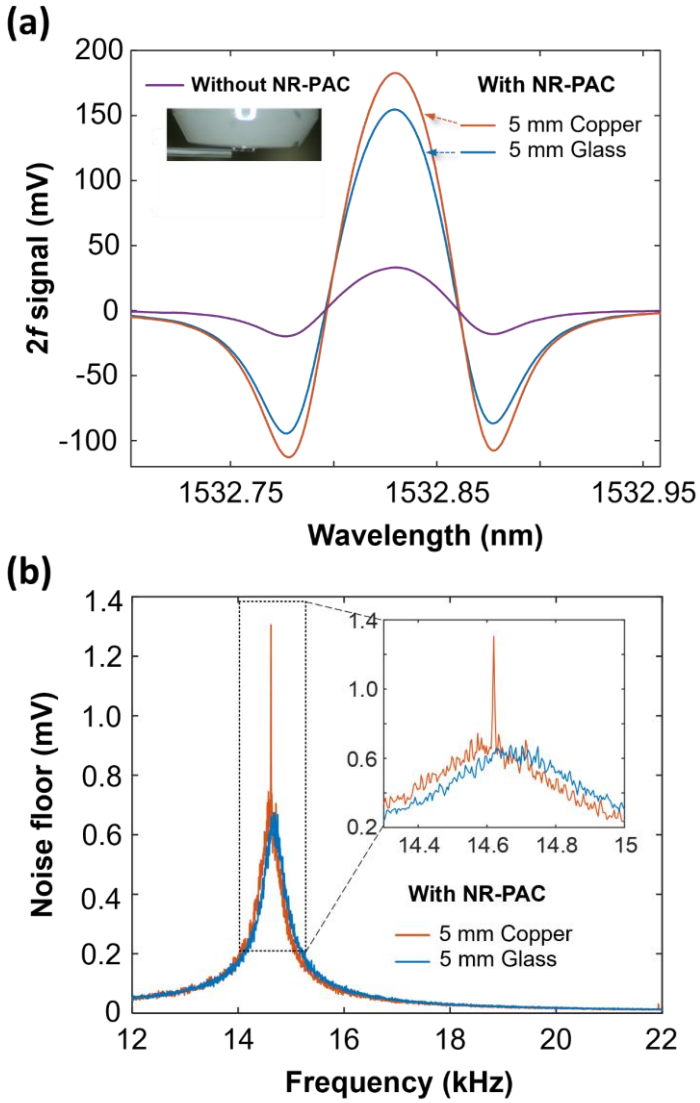

Figure 3.13. (a) PAS signal enhancement comparison for direct detection vs. copper/glass PACs. (b) Noise floor contrast between copper and glass PAC configurations.

The fiber-optic OMR-PAS platform, validated for C_2H_2 sensing, employs a versatile OMR microstructure. This design enables broad adaptability to other gases by substituting the pump laser wavelength. Furthermore, integration with tunable or multi-wavelength pump sources could expand the system into a compact, multi-gas detection microsystem without requiring hardware modifications.

3.6 Summary

In this chapter, a compact fiber-optic PAS gas sensor with a microscale PSS-OMR fabricated via in-situ 3D micro-printing on a fiber-optic ferrule end-face has been presented. By leveraging intrinsic optical coupling and resonant mechanical amplification, the design reconciles the inverse relationship between miniaturization and sensitivity inherent to conventional PAS systems. Experiment results validated a NEC of 45 ppb for C_2H_2 using a sensor head of 400 μm diameter. The response time of the sensor is about 0.2 s. The sensors have been further demonstrated through tests of dynamic range linearity from 10 to 1000 ppm and stability confirmed by Allan deviation analysis. With its rapid response, high sensitivity, and sub-millimeter footprint, this sensor technology addresses critical needs in environmental monitoring, industrial emission tracking, and real-time gas diagnostics. It can be employed to future develop multiplexed gas detection system for field deployment under fast varying conditions.

Chapter 4

Ultraminiature optical fiber photoacoustic spectroscopy gas sensor based on a 3D micro-printed fiber-top optomechanical microresonator

4.1 Introduction

Optical fiber PAS gas sensor based on optomechanical resonator (OMR) developed in Chapter 3 has shown its great promise in the development of miniature optical PAS sensors with high sensitivity and fast response. However, the use of external PAC makes the PAS gas sensor system bulky, which thus restricts its applications in space-constrained environments or high-density integration in future intelligent machines.

One of the promising solutions is optical fiber-tip PAS gas sensors with integrated PAC. The monolithic configuration makes the PAS system insensitive to mechanical vibrations, and thus the system could be compact and portable. For example, Zhou et al. demonstrated a fiber coupled CEPAS gas sensor for *in situ* trace gas detection in millimeter scale volumes [120]. The sensor consists of a non-resonant photoacoustic cell with glass micro-mirror suspended by a carbon fiber cantilever over the cell inlet, and its signal is readout interferometrically. By utilizing the

cantilever's mechanical resonance, it achieves a LoD of 24 ppb for C_2H_2. However, the reliance on two separate fibers for excitation and interrogation introduces complexity and compromises miniaturization of sensor head. In addition, Ma et al., demonstrated an ultracompact optical fiber-tip PAS gas sensor by assembling a polymer membrane on a short section of capillary at the end-face of an optical fiber [52]. It is a monolithically designed PAS sensor integrated with both a micrometer-scale PAC and FP micro-interferometer, achieving a very low LoD of 9 ppb in the detection of C_2H_2 gas. However, the mechanical resonance frequency of such a membrane is as high as ~520 kHz, where PAS signal is weak due to the damping effects from gas and heat flow in the cavity. Consequently, the sensor operated at a non-resonant frequency, i.e., 14 kHz, instead of its resonant frequency, thereby not benefiting from resonance amplification.

To overcome these challenges, in this Chapter, we present a monolithically designed optical fiber-tip gas sensor with a miniaturized PSS-OMR for resonance-enhanced PAS gas sensing. Compared to the ferrule-top PSS-OMR sensor reported in Chapter 3, the fiber-top OMR does not require an external PAC and is thus more suitable for space-constrained applications. Using our in-house optical 3D micro-printing technology, a micrometer-scale PAC integrated PSS-OMR with the height of 90 μm and the diameter of 120 μm was directly printed on the end-face of a single mode fiber (SMF). With a special design of spiral cantilevers

(i.e. microbeams), the PSS-OMR's resonant frequency is customized to be about 105 kHz. Experimental results show that mechanical resonance can enhance the PAS gas sensor's signal-to-noise ratio by approximately 5.5 times compared to off-resonance operation. The sensor can detect C_2H_2 gas at very low concentration levels down to 55 ppb without the need for an additional PAC, and its response time is less than 0.2 seconds.

4.2 Design and analysis of optical fiber PAS gas sensor based on a fiber-top optomechanical resonator

Figure 4.1 (i & ii) shows the schematic design of optical fiber-tip OMR-PAS sensor for trace-gas monitoring. The sensor uses a pump-probe sensing scheme, in which an SMF is used to deliver both the pump and probe lights into the micro-PAC integrated PSS-OMR. The central part of the PSS-OMR is a thin-film reflector that, together with the SMF end-face, forms a micrometer-scale FP interferometer (FPI). When gas molecules diffuse into the micro-PAC under the PSS-OMR, they absorb the modulated pump light and undergo non-radiative relaxation, generating periodic heating and consequently acoustic waves.

As shown in **Fig. 4.1(a)(ii)**, The weak PA signal can excite the vibrational resonance of the fiber-top PSS-OMR. Such an acoustic wave-induced resonant vibration of the suspended microdisk, i.e., thin-film reflector, may cause periodic variations of the FPI's length, reaching their

maximum amplitude when the 2 times of pump modulation frequency matches the resonance frequency of the PSS-OMR and then can be read out by an interferometric means. A photograph of the optical fiber-tip sensor is shown in **Fig. 4.1(b)**.

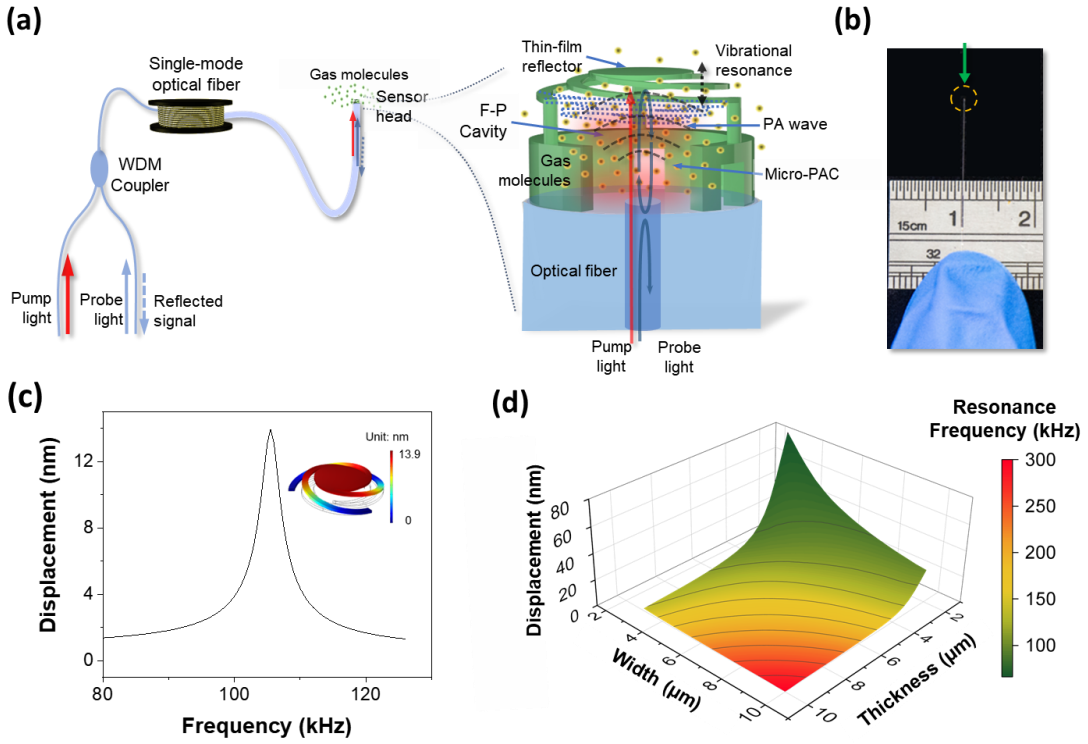

Figure 4.1. (a)(i) Schematic of an optical fiber-tip OMR-PAS gas sensor. (ii) Schematic of the sensor head based on a PAC integrated OMR. (b) A photograph of the sensor. (c) Simulated frequency response of the PSS-OMR. The inset shows its fundamental vibration mode. (d) Simulation results of displacement and resonance frequencies of the PSS-OMR as a function of the width and thickness of microbeams.

4.3 Numerical simulation results

Mechanical responses of the designed PSS-OMRs were numerically analyzed by using a commercial FEM software, i.e., COMSOL

Multiphysics. The PSS-OMRs are made of SU-8 resin, whose Young's modulus and Poisson ratio used in simulation are 3.4 GPa and 0.22, respectively [110]. Material intrinsic loss was included as damping in numerical simulation. Solid mechanics and pressure acoustics analysis were conducted to study the induced displacement and eigenfrequencies of the designed PSS-OMR, respectively.

Fig. 4.1(c) shows a typical simulated frequency response of the PSS-OMR under the excitation of 1-Pa acoustic pressure. As PAS gas sensors are not allowed to work at high frequency due to gas molecules' thermal damping effects, the width and thickness of the microbeams of PSS-OMR are chosen to be 6 μm and 3 μm, respectively, resulting in a natural resonance frequency of 105 kHz. From the simulation result, the Q factor of the fundamental resonance is about 20. The simulated displacement of the thin-film reflector under resonance is 13.9 nm, which is about 33.2 times the displacement observed under a 1-Pa static pressure (i.e., 0.419 nm). Notably, the micromechanical resonance of such a PSS-OMR can be flexibly customized by tailoring the width or thickness of its microbeams. **Fig. 4.1(d)** shows a summary of the calculated displacement of the PSS-OMRs with different wide and thick microbeams at the fundamental vibration resonance under the excitation of 1-Pa acoustic pressure. As expected, the displacement increases with the decreases of the microbeam's width and thickness, while the resonant frequency varies

oppositely.

4.4 Fabrication results

4.4.1 Photoresist materials for fabrication

The material used in the fabrication of the OMRs is EPON SU-8 resin acquired from HEXION Ltd. To prepare the photoresist, solid SU-8 resin was dissolved in cyclopentanone (sourced from Aladdin Scientific Corp.) at weight ratios of 20% (base layer) and 25% (top layer). The formulation included 4-octyloxydiphenyliodonium hexafluoroantimonate (OPPI, supplied by Arctom Scientific) and tributylamine (TBA, obtained from Meryer Chemical Technology Co., Ltd.), serving as the photoinitiator (4% by weight relative to SU-8) and inhibitor (0.5% by weight), respectively. For the upper layer fabrication, Tinuvin 234 (2-(2H-benzotriazol-2-yl)-4,6-bis(1-methyl-1-phenylethyl)phenol, procured from J&K Scientific), a UV-absorbing additive, was incorporated at 0.4% by weight relative to the SU-8 resin to enhance the vertical discernibility of the optical 3D micro-printing process.

4.4.2 3D micro-printing processes

The OMRs are directly printed on the optical fiber surface by utilizing our in-house 3D μ-printing technology [81, 82, 106]. **Figure 4.2** shows the dual-layer fabrication processes for the base and top structures. Initially, SU-8 photoresist was deposited on the fiber end-face via dip-coating. After

coating each layer of SU-8, the sample was soft-baked at 65°C (5 minutes) and 95°C (15 minutes) to remove residual solvents. After soft-baking, a machine vision-guided maskless UV lithography process defined structural patterns by projecting sliced 3D model data onto a DMD board, enabling real-time generation of UV exposure patterns. UV irradiation of 54.3 mW/mm² was applied for 40 s (base layer) and 150 s (upper layer). After exposure, the sample was post-baked in a forced-air convection oven at 65°C for 40 minutes. Eventually, the sample was developed involving immersion in propylene glycol monomethyl ether acetate (PGMEA), followed by rinsing with methyl nonafluorobutyl ether ($C_5H_3F_9O$) to preserve the 3D geometry [111]. The fabrication processes were repeated for the next layer of the designed 3D structure. After the two-round fabrication processes, the fabricated sample was hard-baked at 120°C for 60 minutes.

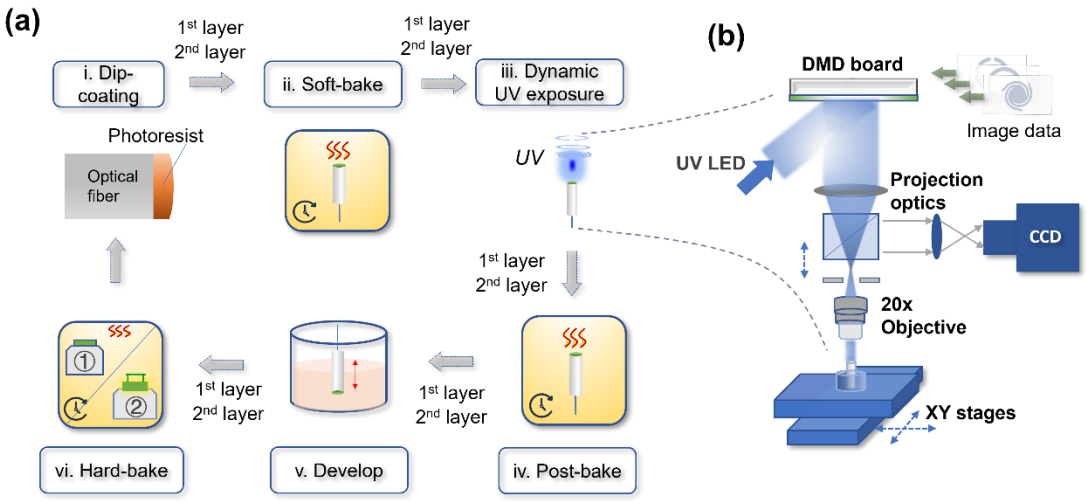

Figure 4.2. (a) Fabrication processes of 3D microstructures on the end faces of optical fibers. (b) Schematic diagram of the optical maskless exposure system.

4.4.3 3D Microprinted Optical Fiber-Top FP Microcavity

Figure 4.3(a) (i & ii) show the scanning-electron microscopy (SEM) images of PAC-integrated OMRs fabricated on the end-face of an optical fiber. The whole structure has a height of ~90 μm and diameter of 120 μm, which is precisely aligned with the end-face of a SMF. The lower layer of the structure is a ~40-μm-high three-petal base with three holes, allowing gas molecules flowing into the PAC. The diameter of its inner cavity is ~ 80 μm. The upper layer consists of a microdisk connected to supporting pillars by using three 5 μm-thick spiral microbeams. The length of each microbeam is about 106 μm. The central part of the microdisk is relative thin, called as thin-film reflector, forms together with the end-face of SMF a micrometer-scale FP interferometer. As shown in **Fig. 4.3(a)(ii)**, when the disc is relatively thin, a shallow perimeter is shown, which attributes to a uniform optical spectrum of the F-P cavity. The measured reflection spectrum of the FP micro-interferometer is shown in **Fig. 4.3(b)**. The measured free spectral range (FSR) is ~13.3 nm and fringe contrast is ~8 dB at near 1550 nm. By applying a fast Fourier transform (FFT) to the measured reflection spectrum, the length of the FP microcavity can be estimated to be about 84 μm.

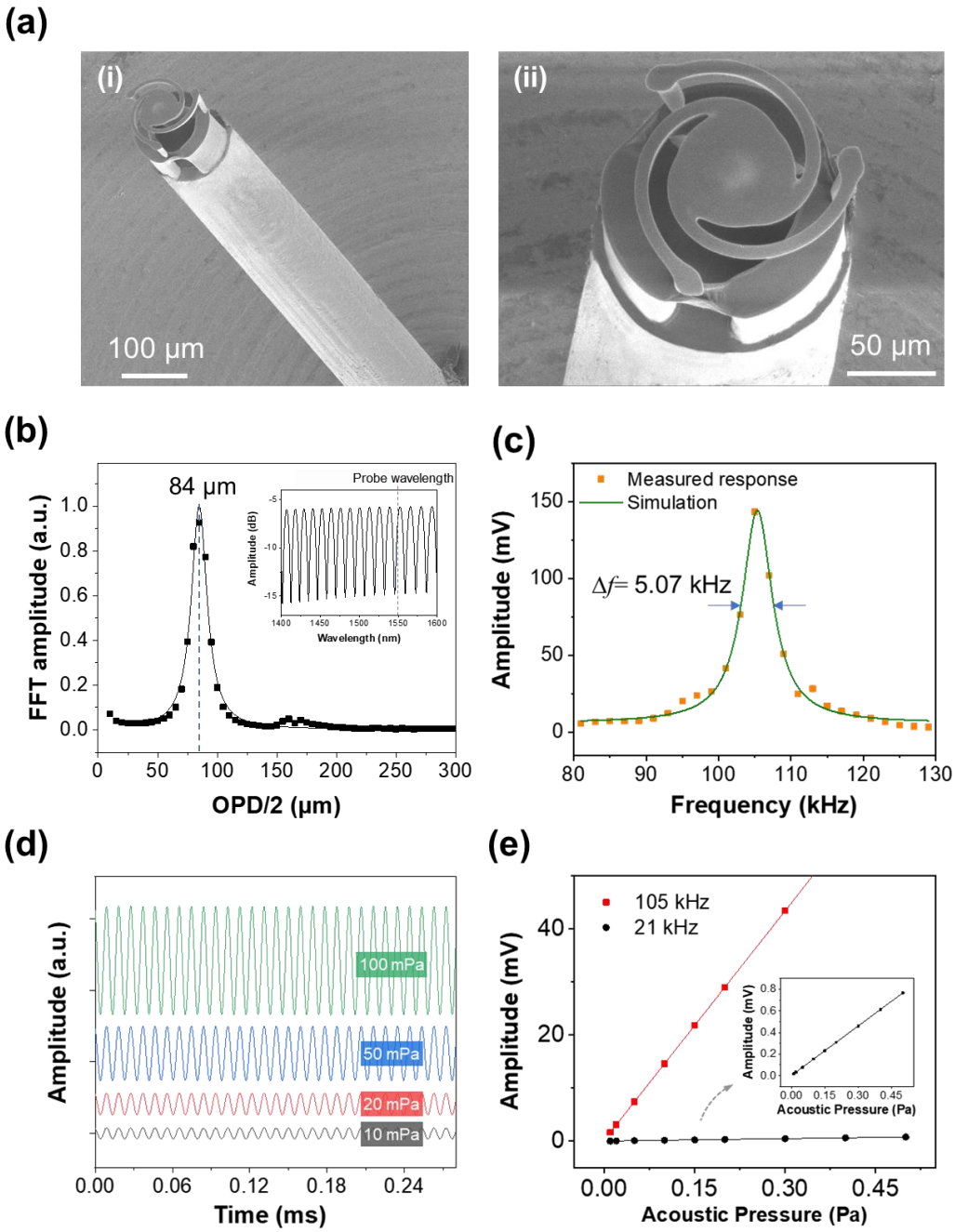

Figure 4.3. (a)(i) and (ii) SEM images of the fabricated optomechanical resonator. (b) FFT spectrum derived from measured reflection spectrum of the fabricated OMR. Inset: the corresponding reflection spectrum. (c) The measured frequency response of the OMR under 1-Pa acoustic excitation. (d) The output waveform measured at 105 kHz under acoustic pressure of 10, 20, 50, and 100 mPa. (e) A comparison of the output amplitude of the OMR working at resonant and non-resonant frequencies.

4.5 Testing of optical fiber OMR-PAS gas sensors

4.5.1 Experimental setup for acoustic testing

The acoustic performance of the fabricated PSS-OMR was evaluated experimentally using a home-made characterization platform, as shown in **Fig. 4.4**. Acoustic excitation was delivered via a piezoelectric transducer driven by a programmable waveform generator, producing controlled pressure waves across ultrasonic frequencies. To interrogate high-frequency acoustic responses, a narrow-linewidth probe laser source was implemented, with its wavelength stabilized at the quadrature bias point of the FPI. Reflected optical signals were routed through a circulator to a high-bandwidth photodetector (10–300 kHz passband), with resultant voltage waveforms captured and analyzed using a digital oscilloscope. For calibration, a reference condenser microphone was mounted near the optical fiber-tip OMR-PAS sensor to measure acoustic pressure for calibration. The piezo loudspeaker, the optical fiber-tip OMR-PAS sensor, and the calibration microphone were placed in an acoustic isolation box to suppress the noise influence from external environment.

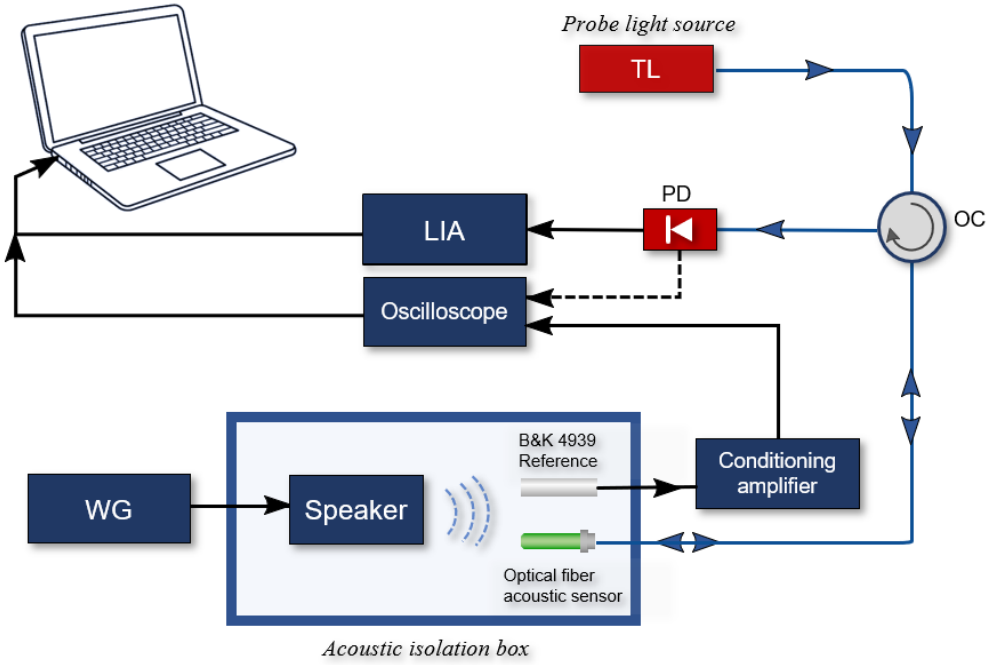

Figure 4.4. Schematic diagram of the acoustic testing setup. The passband of the PD is set from 1 kHz to 300 kHz. TL: tunable semiconductor laser; OC: optical circulator; PD: power detector; LIA: lock-in amplifier; WG: waveform generator.

4.5.2 Experimental setup for PAS gas testing

The optical fiber OMR-PAS gas sensor was characterized using a pump-probe dual-laser interrogation system (**Fig. 4.5**). A 1533-nm distributed feedback (DFB) laser served as the pump source, with its output amplified via an erbium-doped fiber amplifier (EDFA) to boost excitation intensity. A tunable semiconductor laser (TSL), operating across 1500–1630 nm, provided the probe beam. To stabilize the interferometric readout, the probe wavelength was dynamically regulated via a proportional-integral-derivative (PID) feedback loop, maintaining operation at the quadrature bias point. During testing, the probe wavelength was scanned across the P(13) absorption line of acetylene (C_2H_2) while being sinusoidally

modulated at 52.5 kHz—half the sensor's resonant frequency—to generate photoacoustic excitation.

Gas concentration quantification employed wavelength-modulated second-harmonic (2*f*) spectroscopy. The photoacoustic signal was extracted using a lock-in amplifier (Zurich Instruments MFLI, 0–500 kHz bandwidth), synchronized to the modulation frequency for noise suppression. During testing, the OMR-PAS gas sensor was placed inside a small gas chamber with two outlets for gas exchange.

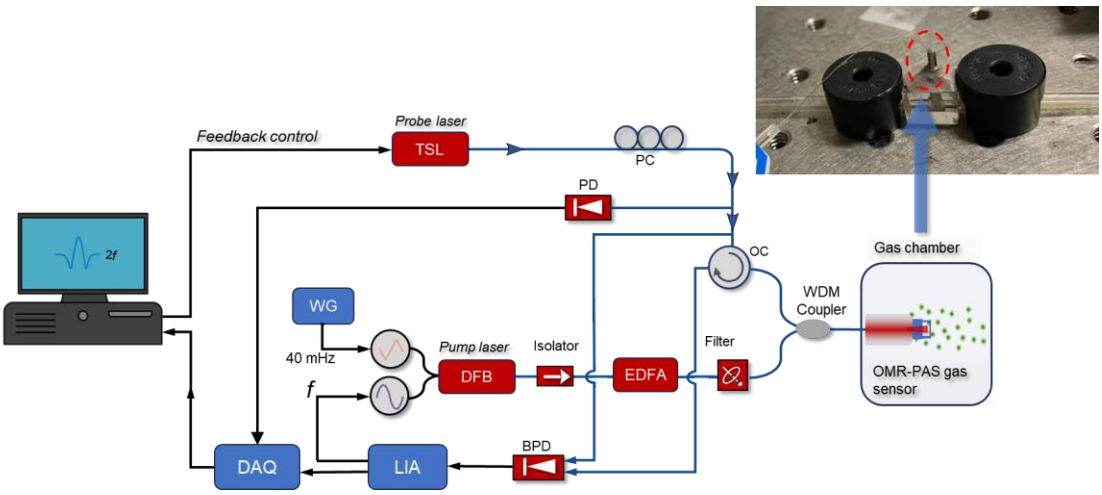

Figure 4.5. Schematic diagram of the PAS gas sensing setup. The photograph of the setup is shown in the inset. DFB, distributed feedback laser; TSL, tunable semiconductor laser; EDFA, erbium-doped fiber amplifier; WDM, wavelength-division multiplexer; PC, polarization controller; OC, optical circulator; BPD, balanced photodetector; LIA, lock-in amplifier; DAQ, data acquisition card; WDM, wavelength division multiplexing.

4.5.3 Preparation of gas samples

Standard gases for calibration were prepared through precise volumetric

blending of certified reference materials under ambient conditions (25°C, 1 atm). A 1010 ppm acetylene (C_2H_2) primary standard was diluted with ultrapure nitrogen (99.999%) using dual mass flow controllers (MFCs) operating in dynamic mixing mode. The MFCs maintained traceable flow rates to achieve target dilution ratios, enabling preparation of sub-ppm analytical gas mixtures with ±1% accuracy.

4.5.4 Acoustic sensing tests

The measured frequency response of the PSS-OMR to acoustic waves is shown in **Fig. 4.3(c)**. The fundamental resonant frequency was measured at approximately 105 kHz. Under non-resonant conditions, the frequency response curve exhibits a relatively uniform profile. The resonance peak exhibits a Lorentz shape with a full-width-half-maximum (FWHM) of 5.07 kHz, corresponding a mechanical quality (Q) factor of 20.7. A comparison of this measured frequency response to the simulation is given at **Fig. 4.6(a)**, which shows good coincidence.

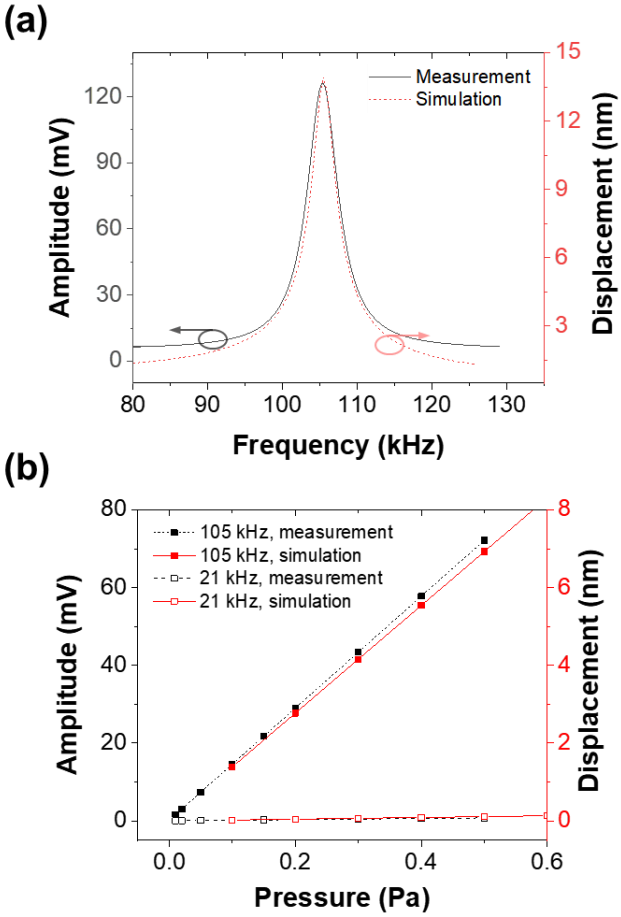

Figure 4.6. (a) Comparison of simulated displacement and measured frequency response (Lorentz fitting) of the sensor. (b) Comparison of simulated displacement and measured output amplitude of the sensor in resonance and non-resonance frequencies under various acoustic pressure.

Figure 4.3(d) shows the measured time-domain signals of the optical fiber OMR sensor at its resonance frequency of 105 kHz when the applied acoustic pressure are 10, 20, 50, and 100 mPa, respectively. The measured sensor output intensities with respect to applied acoustic pressures are illustrated in **Fig. 4.3(e)**, comparing its performance under resonant (colored line) and non-resonant conditions. The output signals exhibited a linear dependence on the acoustic pressure in both cases. The measured sensitivity of the sensor at resonance is 144 mV/Pa, compared to just

1.53 mV/Pa under non-resonant conditions, indicating that the resonance can enhance the sensor's acoustic sensitivity by 94 times. The power spectral densities obtained by FFT of the waveforms are shown in **Fig. 4.7**. A signal-to-noise ratio (SNR) as high as 45 dB was achieved under 100-mPa acoustic pressure, yielding an estimated noise-equivalent acoustic sensitivity of 10.7 μPa/Hz$^{1/2}$. For comparison, the measurements were repeated at a non-resonant frequency of 21 kHz, resulting in a sensitivity of 154.3 μPa/Hz$^{1/2}$.

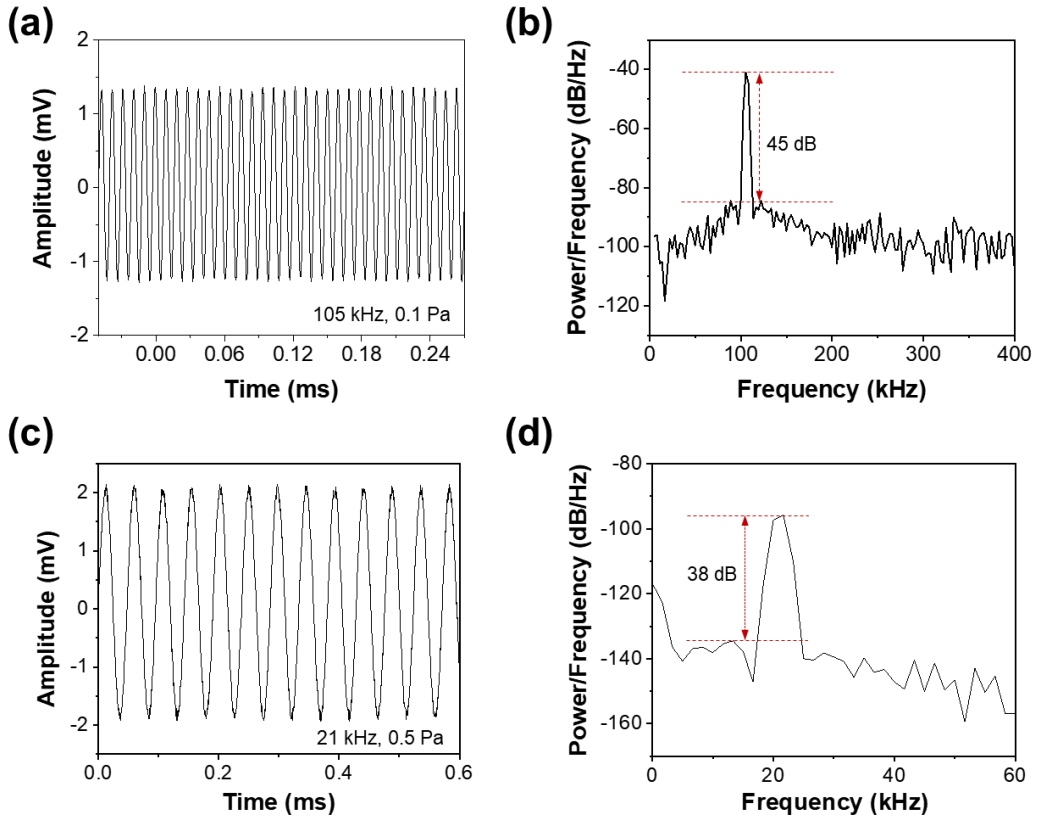

Figure 4.7. Measured output waveform and the corresponding power spectral densities. (a) and (b) represent OMR at resonance frequency of 105 kHz and acoustic pressure of 0.1 Pa. (c) and (d) represent the same OMR at non-resonance frequency of 21 kHz and acoustic pressure of 0.5 Pa.

4.5.5 Photoacoustic gas sensing tests

The detection limit of the OMR-PAS gas sensor was tested by continuously injecting N_2-balanced 1010-ppm C_2H_2 gas into the chamber. **Figure 4.8(a)** presents the 2*f* lock-in output signals acquired by scanning the pump wavelength across the *P*(13) absorption line of C_2H_2 at varying input pump power level when the demodulation frequency is 21 kHz (i.e., at off-resonance operation). **Figure 4.8(b)** displays the corresponding signals measured at a demodulation frequency of 105 kHz (i.e., at resonance mode). The corresponding peak-to-peak value of the 2*f* signal (PA signal) against the input pump power level is shown in **Fig. 4.8(c)**. In both cases, the peak-to-peak 2*f* signal amplitude exhibits a linear relationship to the pump power. As a comparison, the sensitivity is enhanced by ~14.1 times when the sensor worked at resonance mode.

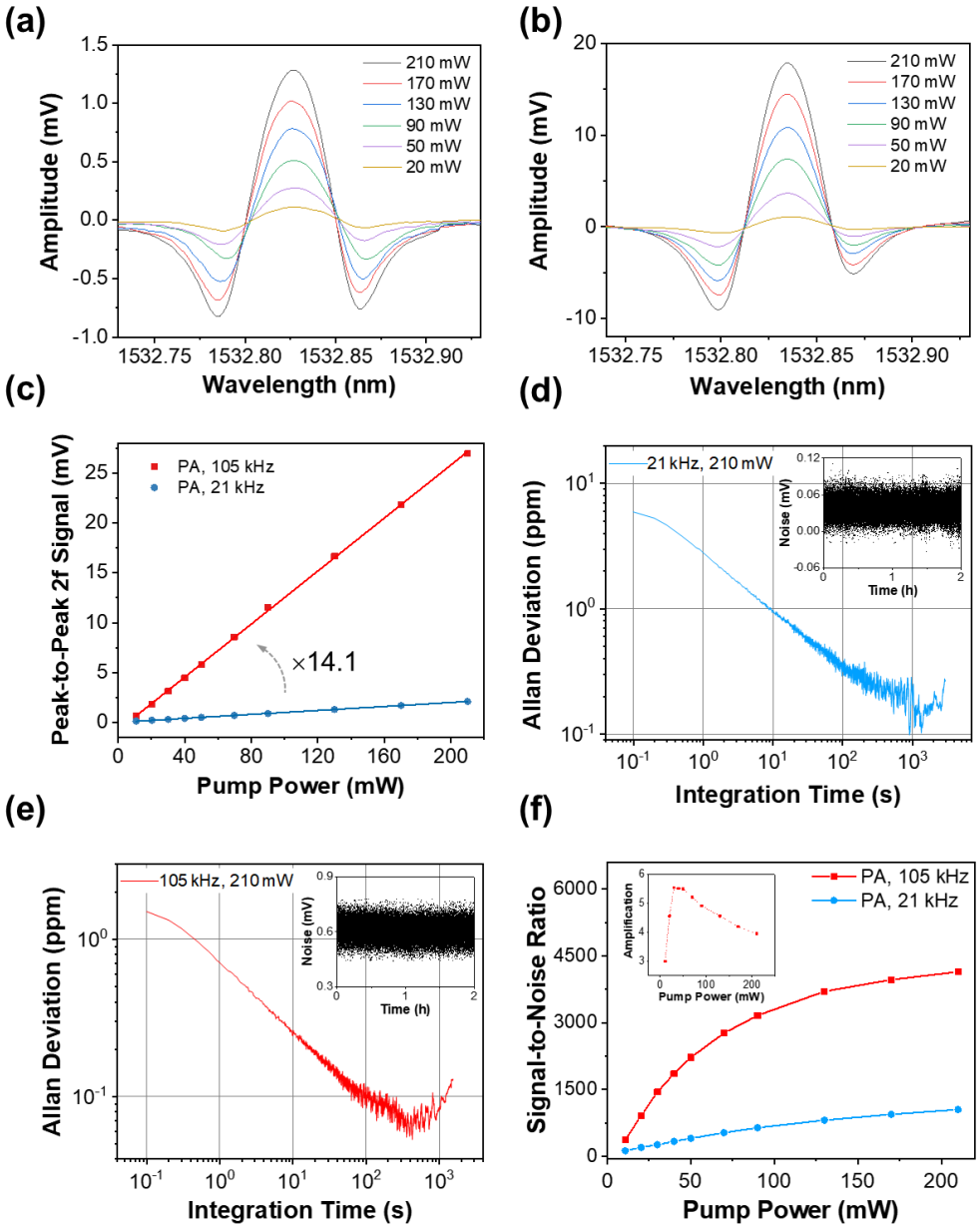

Figure 4.8. (a) Measured 2*f* signals for 1010-ppm C_2H_2 at 21 kHz under different input pump power levels. (b) Measured 2*f* signals for 1010-ppm C_2H_2 at 105 kHz under different input pump power levels. Data in (a, b) was measured under the detection bandwidth of 0.9375 Hz. (c) Peak-to-peak amplitudes of the 2*f* signal at the two frequencies plotted as a function of input pump power. (d) Allan-Werle deviation plot at 21 kHz, derived from 2-hour noise data recordings (inset). (e) Allan-Werle deviation plot at 105 kHz, derived from 2-hour noise data recordings (inset). Data in (d, e) was measured under the detection bandwidth of 3.125 Hz. (f) Comparison of the SNRs measured at the resonant (105 kHz) and non-resonant (21 kHz) frequencies. The inset is the calculated amplification. Noise levels were assessed using 10-s integration time.

The system noise is measured when the pump wavelength is fixed at the *P*(13) absorption line and the gas chamber is filled with pure N_2 for both resonance and non-resonance frequencies, respectively. To further assess the noise equivalent concentration (NEC) of the fabricated fiber-top OMR for C_2H_2 gas detection, we conducted an Allan-Werle deviation analysis [115, 116] based on the obtained noise data. As shown in **Fig. 4.8(d)**, under off-resonance operation, when the input pump power was 210 mW, the SNR for 10-s lock-in time constant calculated from the measured data was ~1050, whose corresponding NEC and noise equivalent absorption (NEA) were 962 ppb C_2H_2 and ~1.01×10^{-6} cm^{-1}, respectively. The NEC decreased with an increase of integration time up to 538 seconds, at which the NEC reached a minimum of 144.6-ppb C_2H_2, corresponding to a NEA of 1.52×10^{-7} cm^{-1}. **Fig. 4.8(e)** presents the measured result of the sensor under resonance operation. As a comparison, when the input pump power kept as 210 mW, the SNR for 10-s lock-in time constant was ~4146, whose corresponding NEC and NEA are 243.6 ppb C_2H_2 and ~ 2.56×10^{-7} cm^{-1}, respectively. Compared with off-resonance operation, the SNR is amplified by ~3.95 times by the resonance of PSS-OMR. The NEC further decreased with the increase of integration time. When the integration time is 356 seconds, the NEC reached a minimum of 55-ppb C_2H_2, corresponding to a NEA of 5.78×10^{-8} cm^{-1}, indicating the remarkable benefit of optomechanical resonance in enhancing the gas sensor's

detection ability.

A comparative analysis of the SNRs for the operations at 21 kHz and 105 kHz with an integration time of 10 s is shown in **Fig. 4.8(f)**. The SNRs at the resonance frequency are remarkably higher than these at the non-resonant frequency, highlighting the benefit of resonance amplification. As shown in the inset, the amplification factor quickly increased when the pump power increased from 10 mW to 30 mW, but it gradually dropped after the pump power further increased. When the pump power was 30 mW, the SNR at 105 kHz was 1445, whose corresponding NEC reached sub-ppm level, and it is about 5.5 times of the SNR measured at the frequency of 21 kHz. As a comparison, the SNR measured at the frequency of 21 kHz using the pump power of 210 mW was 1050. It indicates that the resonance amplification mechanism can substantially improve power efficiency to achieve a high SNR at a relatively low pump power.

The dynamic range of the optical fiber-tip OMR-PAS gas sensor was tested by filling C_2H_2 of different concentrations into the gas chamber at room temperature and atmospheric pressure. **Fig. 4.9(a)** shows the measured 2*f* signals for 10, 50, 100, and 200-ppm C_2H_2 when the pump power was 210 mW. The peak-to-peak values of these 2*f* signals with respect to C_2H_2 concentration are given in **Fig. 4.9(b)**. The measured results show that the peak-to-peak signal values exhibit a good linear relationship with C_2H_2 concentrations ranging from 10 to 1010 ppm, whose

coefficient of determination R^2 is 0.9986.

The response time of the gas sensor is tested by sequentially filling the gas chamber with pure N_2, 1010 ppm C_2H_2 in N_2, and then pure N_2 at a flow rate of 250 standard cm^3/min (SCCM) while the pump wavelength is fixed to the center of *P*(13) absorption line of C_2H_2. **Figure. 4.9(c)** illustrates the real-time recording of the 2*f* signal, which has been normalized by removing the baseline and scaling them against the maximum value. The response time, specifically the time required for the response reaching 90% (i.e., rise time) and descending to 10% (i.e., fall time) of the maximum 2*f* signal, is around 0.10 and 0.17 seconds, respectively. The long-term stability of the sensor system was tested by continuous measurement of 1010-ppm C_2H_2 in a laboratory environment. As shown in **Fig. 4.9(d)**, the measured fluctuation of the peak-to-peak 2*f* signal is ±3% over 1.5 hours.

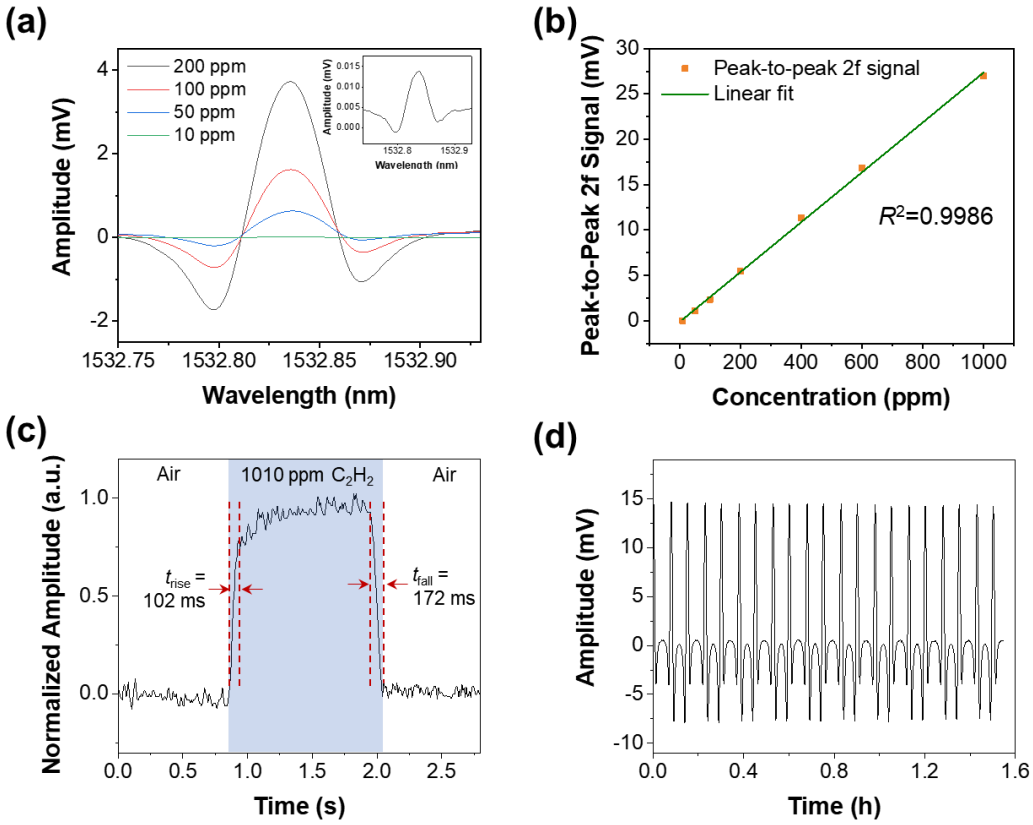

Figure 4.9. (a) 2*f* signal when pump laser is tuned across the P(13) line of C_2H_2 for 10, 50, 100, 200 ppm C_2H_2 at room temperature and atmospheric pressure. (b) Peak-to-peak value of the 2*f* signal as function of gas concentration. (c) Response time testing result. At ~0.6 s, 1010 ppm C_2H_2 gas was loaded into the gas chamber prefilled with N_2 at a flow rate of 10 SCCM, respectively. At ~1.9 s, pure N_2 was filled into the gas chamber at the same flow rate. Data in (c) is obtained with detection bandwidth of 9.4 Hz. (d) Measured 2*f* signal over a period of 1.5 h.

4.5.6 Discussion

Notably, the localized heating caused by the gas molecules' absorption of optical fiber-guided pump laser, known as the photothermal (PT) effect, leads to a change of refractive index (RI) of the gas medium. Therefore, one can infer that the PT effect also contributes to the phase change of the

probe light in FP cavity and thus conduces to the interferometric readout, especially when the pump light power is high. To evaluate the contributions of PT effect on the measured interferometric readout, we fabricated a reference photothermal interferometric (PTI) sensor head whose thin-film reflector is suspended by using short and wide beams, as shown in **Fig. 4.10(a)**. From the measured reflected spectrum and its corresponding FFT result, as shown in **Fig. 4.10(b)**, the cavity length of the reference sample is 88 μm, which is nearly identical to the fiber-tip OMR-PAS gas sensor. Since this reference PTI sensor has negligible response to acoustic wave, it can be used to assess the PT contribution in the OMR-PAS gas sensor.

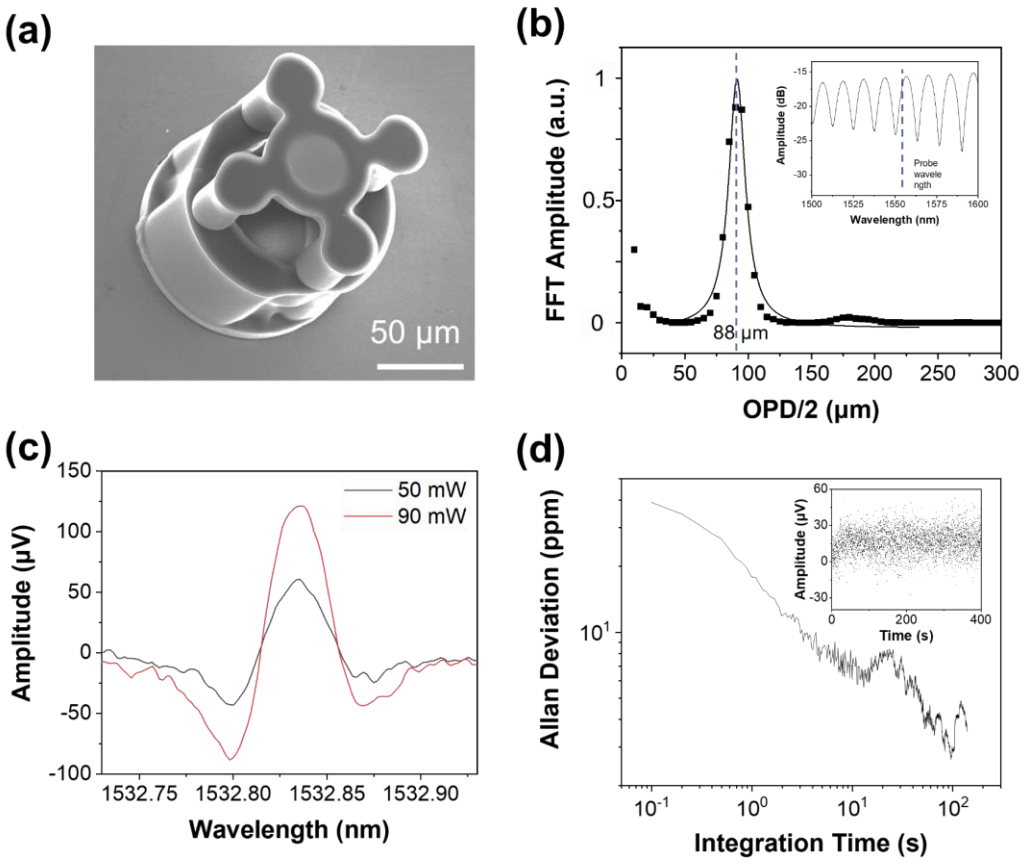

Figure 4.10. (a) The SEM image of an optical fiber-tip PTI gas sensor for reference. (b)

FFT spectrum derived from measured reflection spectrum of the fabricated sensor. Inset: the corresponding reflection spectrum. (c) 2*f* signal measured at 105 kHz of the PTI gas sensor with different pump power. The C_2H_2 concentration was 1010 ppm and data was measured with a detection bandwidth of 0.9375 Hz. (d) Allan-Werle deviation plots of the PTI gas sensor based on noise data over a period of 400 s with the detection bandwidth of 3.125 Hz and N_2 flow rate at 10 SCCM. The pump power was 90 mW and modulation frequency was 52.5 kHz.

A comparison of the peak-to-peak 2*f* signals at the frequencies of 21 kHz and 105 kHz measured by using the two sensor heads under different pumping power is shown in **Fig. 4.11(a)**. If we compare the peak-to-peak 2*f* signals measured by the reference sensor head, it can be observed that the PT effect decreases when the modulation frequency increases. This is due to the reduction in PT-induced refractive index modulation with increasing heat modulation frequency [121]. If we compare the peak-to-peak 2*f* signals at 21 kHz measured by the two sensor heads, it can be seen that the PT effect contributed a considerable proportion and the PA effect has further remarkably enhanced interferometric signal for OMR-PAS gas sensor. It attributes to the delicate design of the PSS-OMR and the integrated micro-PAC, which has effectively overcome the low acousto-mechanical coupling efficiency of this 100-μm scale PAS sensor operating at dozens kHz (at which frequency the wavelength of the acoustic wave ranges from millimeter to centimeter).

The measured SNRs at the two frequencies (i.e., 21 kHz and 105 kHz) measured by using the two sensor heads are presented in **Fig. 4.11(b)**. One

can see that, as the same with the measured peak-to-peak 2*f* signals, the SNRs at the frequency of 105 kHz (i.e., the resonance frequency of PSS-OMR) of the OMR-PAS sensor are far beyond the SNRs measured at the frequency 21 kHz and those measured by using the reference PTI sensor head at these two frequencies. It further confirms the superior role of the PSS-OMR's resonance in enhancing the signal of PAS gas sensors.

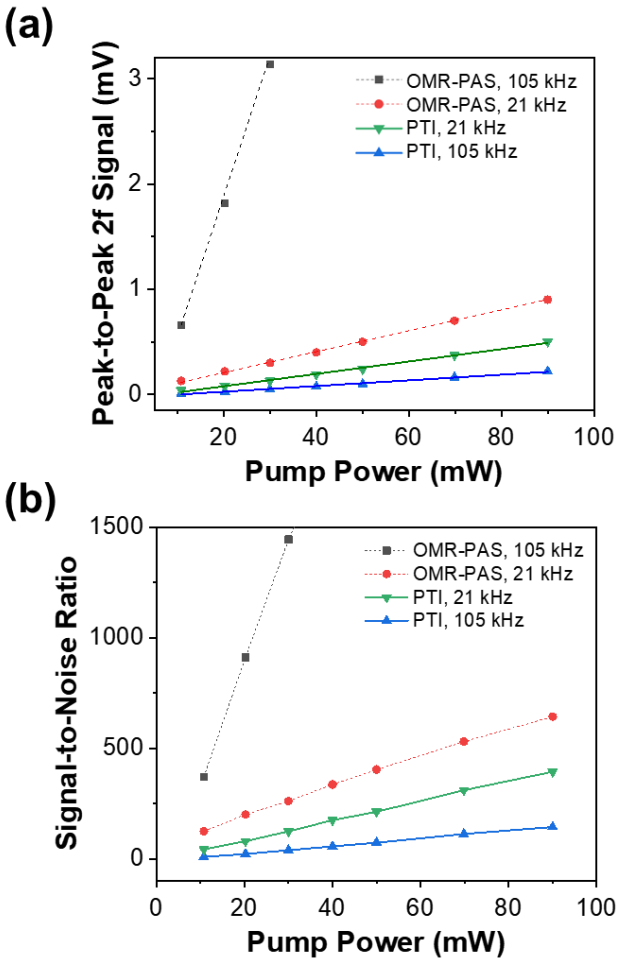

Figure 4.11. (a) Comparison of the measured amplitude of 2*f* signals of the OMR-PAS sensor and the reference PTI sensor at the frequencies of 105 kHz and 21 kHz, respectively. (b) Comparison of the measured SNRs of the OMR-PAS sensor and the reference PTI sensor at the frequencies of 105 kHz and 21 kHz, respectively. Noise levels were assessed using 10-s integration time.

Notably, the fiber-tip OMR-PAS gas sensor has a detection limit of 55

ppb, which is a bit higher than 45 ppb achieved in Chapter 3. This is mainly due to three reasons: 1) the reduced size of the fiber-top OMRs lowers its acoustic sensitivity and acousto-mechanical coupling efficiency; 2) a silica-tube PAC was used to enhance acousto-mechanical coupling efficiency in the optical fiber OMR-PAS gas sensor demonstrated in Chapter 3; 3) the reduced size results in a much higher resonant frequency at which the PA signal becomes weaker due to the damping effects.

The performance of recently reported compact PAS systems based on different types of miniature optical microphones is compared in terms of the system size, working / resonance frequency, NNEA, pump power, and SNR in **Table 4.1**. In general, the PSS-OMR with micrometer-scale monolithic design without the need for additional PAC exhibits a detection limit on the level of <100 ppb that is comparable with the large-size or even benchtop PAS sensor systems, and it has a microscale footprint featuring more than 3 orders of magnitude smaller than conventional PAS sensors. The SNR achieved by the PAS gas sensor at a given pump power was also remarkably higher than other previously reported sensors.

Table 4.1. Performance comparison with small-footprint PAS systems

Microphone type	Sensor head dimension (mm)	Working frequency / Resonance frequency	Integration time	LoD	Response time
Quartz tuning fork [98]	9.4 × 4.8 × 0.25	15.8 kHz / 15.8 kHz	316 s	50 ppb	300 ms

Membrane [9]	2.5 × 2.5 ×0.1	45.68 kHz / 45.68 kHz	200 s	119.8 ppb	Not stated
Membrane [52]	0.125 × 0.125 × 0.06	14 kHz / 520 kHz	200 s	9 ppb	20 ms
Cantilever [53]	2 × 1 (cantilever size only)	0.9 kHz / 0.9 kHz	10 s	860 ppb	Not stated
Cantilever [70]	2 × 0.8 (cantilever size only)	2.68 kHz / 2.68 kHz	1 s	200 ppb	Not stated
OMR (This work)	**0.125 × 0.125 × 0.09**	**105 kHz / 105 kHz**	**356 s**	**55 ppb**	**172 ms**

4.6 Summary

In summary, we have developed a small-size high-performance optical fiber-tip PAS gas sensor based on a miniaturized PSS-OMR. A 3D micro-printing technology has been utilized to directly print both the PSS-OMR and a micrometer-scale PAC on the end-face of a standard single-mode optical fiber to create a monolithically designed optical fiber OMR-PAS gas sensor. Experiments have been demonstrated that, enhanced by resonance amplification mechanism, this optical fiber-tip OMR-PAS gas sensor can highly sensitively detect low-contraction C_2H_2 gas down to ppb levels without the need of using additional PAC. Moreover, the semi-opening design of this OMR-PAS gas sensor enables a very fast response in gas monitoring, whose response time is less than 0.2 seconds. Such a small-size, high-sensitivity and fast-response gas sensor offers new

opportunities for real-time monitoring of trace gas fluctuations in confined environments, such as operando in-reactor monitoring and intravascular diagnostic applications.

Conclusions and Outlook

Chapter 5

5.1 Conclusions

In this thesis, miniature optical fiber PAS gas sensors based on directly 3D micro-printed OMRs have been developed for detection of trace gases. A special design of PSS-OMR has been devised to tackle the trade-off between small size and high sensitivity for PAS gas sensing. The use of planar-spiral springs not only reduces the size of the entire structure for sensor minimization but also tailors vibration resonance for sensitivity enhancement. A thin-film reflector is introduced in the PSS-OMR to form F-P micro-interferometer together with the end-face of optical fiber for optical interferometric readout of acoustic signals. Moreover, to precisely fabricate such exquisite and complex PSS-OMRs, an optical 3D micro-printing technology has been developed to enable rapid in-situ printing of micrometer-scale OMRs using SU-8 epoxy photoresist, which has advantages of high optical transparency, high mechanical strength, and superb chemical and temperature resistance, for development of small-size PAS gas sensors.

To be specific, two types of miniature optical fiber PAS gas sensors have been developed:

i) Miniature optical fiber PAS gas sensor based on a 3D micro-printed ferrule-top PSS-OMR. A PSS-OMR with a diameter of 400 μm is directly printed on the 1.25-mm diameter end-face of a fiber-optic ferrule to make a miniature optical fiber PAS sensor. Experimental results have revealed that mechanical vibrational resonance of such a PSS-OMR can enhance the sensor's acoustic sensitivity by over two orders of magnitude. The acoustic sensitivity can reach ~870 mV/Pa at a resonant frequency of 14.7 kHz, and noise equivalent acoustic sensitivity is about 147 $\mu Pa/Hz^{1/2}$. A 1.4 μL non-resonant PA cell has been prepared using a glass tube, with which the sensor can detect C_2H_2 gas at the concentration of 45 ppb. The sensor's response is very fast, and its measured response time is about 0.2 seconds.

ii) Ultraminiature optical fiber PAS gas sensor whose sensor head has been further scaled down and liberated from the use of PA cell. A much smaller PSS-OMR has been devised to the end-face of standard optical fiber for PAS gas sensing. Compared with the abovementioned optical fiber PAS sensor, this optical fiber-tip PAS gas sensor has a much smaller sensor head whose size is the same with a standard single-mode optical fiber, i.e., with a diameter of 125 μm. Moreover, it is a monolithic design enabling a direct deliver of pump and probe laser lights via the same optical fiber, eliminating the requirement of PA cell and alignment complexities in traditional PAS gas sensors. Experimental results reveal that mechanical vibrational resonance of this small PSS-OMR can also enhance the sensor's

acoustic sensitivity by about two orders of magnitude. Thanks to the resonance-enhanced mechanism, this optical fiber PAS sensor can detect C_2H_2 gas at the sub-ppm concentration level under a relatively low pump power, i.e., 44 mW, at on-resonance operation mode. Remarkably, compared to off-resonance operation, the signal-noise-ratio (SNR) of this optical fiber-tip PAS sensor can increase by about 550%. Moreover, this optical fiber PAS sensor has also a short response time of ~0.2 seconds.

Table 5.1 shows a summary of recently developed PAS gas sensors in terms of sensor size, pump power, NEC, NNEA, and response time. In general, both ferrule-top and fiber-top OMR-PAS gas sensors achieve a detection limit below 100 ppb, which is comparable to large-scale PAS systems, despite their micrometer-scale dimensions. Their microscale footprint is over three orders of magnitude smaller than conventional PAS sensors. Furthermore, these sensors demonstrate significantly faster response times than previously reported alternatives.

Table 5.1. Performance comparison with recently developed PAS gas sensors

Sensor type	Sensor head size (mm)	PAC	Pump power (mW)	NEC	NNEA (cm^{-1} $W/Hz^{1/2}$)	Response time (s)
Capacitive microphone [122]	N. A.	7.9 mL Resonant PA tube	130	8.7 ppm (H_2O)	N. A.	> 20
Quartz tuning fork [123]	25× 5	272 mL Multi-pass cell	1000	1.29 ppb (C_2H_2)	N. A.	N. A.

Cantilever [124]	2 × 2 × 16	0.35 mL Helmholtz resonator	15	15 ppb (C_2H_2)	2.7×10^{-9}	140
Cantilever [69]	1.5 × 1.5 × 18	32 μL Non-resonant PA tube	20	0.32 ppm (CH_4)	2.44×10^{-8}	N. A.
Diaphragm [9]	2.5× 2.5	Free space	123.9	119.8 ppb (C_2H_2)	9.782×10^{-8}	N. A.
Diaphragm [67]	12.7× 12.7	6.0 mL Resonant PA tube	14.7	4.87 ppb (CH_4)	4.42×10^{-10}	N. A.
Diaphragm [75]	~1.2 × ~1.2	Compact multi-pass cell	20	50 ppb (C_2H_2)	N. A.	N. A.
Cantilever [104]	10 × 10 × 20	0.56 mL Non-resonant PA tube	200	199.8 ppt (C_2H_2)	1.72×10^{-9}	N. A.
Ferrule-top PSS-OMR	**0.4 × 0.4 × 0.09**	1.4 μL Non-resonant PA tube	**390**	**45 ppb (C_2H_2)**	2.89×10^{-7}	**< 0.3**
Fiber-top PSS-OMR	**0.125 × 0.125 × 0.09**	Free space	**210**	**55 ppb (C_2H_2)**	2.29×10^{-7}	**< 0.2**

5.2 Outlook

Although the miniature optical fiber PAS gas sensors developed in this thesis were demonstrated to detect C_2H_2 gas, they can be applied to detect various gaseous analytes, such as methane (CH_4), ethylene (C_2H_4), and carbon dioxide (CO_2), as long as the pump laser with a wavelength matching with target gas absorption line is employed in the PAS system. Moreover, it may enable the detection of multiple gas species without the

need of structural redesign as the sensor head of our PAS system is not wavelength sensitive. This adaptability supports broad applications such as battery health monitoring (detecting C_2H_4 as an early indicator of lithium-ion cell thermal runaway), precision agriculture (tracking ethylene for optimized fruit ripening), and real-time in-reactor process diagnostics.

For instance, the small size, high sensitivity and fast response of these optical fiber gas sensors position them as a promising tool for in-reactor monitoring under complicated conditions. The integration of optical fiber PAS sensor into reactors could enable real-time tracking of gas evolution (e.g., CO_2 in catalytic processes or CH_4 in pyrolysis) to achieve unprecedented insights into dynamic reactions. Such advancements may transform operational paradigms in chemical engineering and materials science, enhancing safety and efficiency while reducing downtime. Moreover, the sensor's fast response (~0.2 s) and resistance to harsh environments make it viable for the deployment of distributed air quality monitoring network or wearable safety devices for hazard gas detection.

To further improve the performances of optical fiber PAS gas sensors, one may enhance either optical or mechanical Q-factor of the PSS-OMR. To enhance optical Q-factor, one may increase the reflectivity of the OMR's F-P cavity by capping the fiber end-face and thin-film reflector with high-reflection materials (e.g., gold nanolayer). It can result in the enhancement of interferometric signal contrast to increase optical

sensitivity of the sensor. Additionally, if a lens-like morphology can be achieved for the thin-film reflector, the in-cavity loss can be depressed to some extent to enhance optical *Q*-factor. To enhance mechanical Q-factor, the material composition or geometric parameters of PSS-OMR can be further optimized. For instance, SU-8 photoresist can be further doped with silica nanoparticles to lower its damping losses to minimize energy dissipation during vibration. These improvements may enhance the sensitivity and reduce operation power consumption of these OMR-based optical fiber PAS gas sensor towards a powerful and versatile tool for various applications with the demands of small size and high sensitivity.

References

1. Hodgkinson, J. and R.P. Tatam, *Optical gas sensing: a review.* Measurement Science and Technology, 2013. **24**(1): p. 012004.
2. Smith, D. and P. Spanel, *The challenge of breath analysis for clinical diagnosis and therapeutic monitoring.* Analyst, 2007. **132**(5): p. 390-6.
3. Adams, A.R., et al., *The prospects of LEDs, diode detectors and negative luminescence in infrared sensing of gases and spectroscopy.* Philosophical Transactions of the Royal Society of London. Series A: Mathematical, Physical and Engineering Sciences, 2001. **359**(1780): p. 621-634.
4. Xu, F., et al., *Concentration evaluation method using broadband absorption spectroscopy for sulfur dioxide monitoring.* Applied Physics Letters, 2006. **88**(23).
5. Mark, G.A., *Diode laser absorption sensors for gas-dynamic and combustion flows.* Measurement Science and Technology, 1998. **9**(4): p. 545.
6. Xiong, S., et al., *Photoacoustic Spectroscopy Gas Detection Technology Research Progress.* Appl Spectrosc, 2024. **78**(2): p. 139-158.
7. Lin, Z., et al., *Insights into Materials, Physics, and Applications in Flexible and Wearable Acoustic Sensing Technology.* Advanced Materials, 2024. **36**(9): p. 2306880.
8. Wu, J., et al., *Fiber-optic photo-acoustic spectroscopy sensor for harsh environment gas detection*. Optical Engineering + Applications. Vol. 6698. 2007: SPIE.
9. Tan, Y., et al., *Optical Fiber Photoacoustic Gas Sensor With Graphene Nano-Mechanical Resonator as the Acoustic Detector.* IEEE Journal of Selected Topics in Quantum Electronics, 2017. **23**(2): p. 199-209.
10. Rosenzweig, Z. and R. Kopelman, *Development of a submicrometer optical fiber oxygen sensor.* Anal Chem, 1995. **67**(15): p. 2650-4.
11. Hoo, Y.L., et al., *Design and modeling of a photonic crystal fiber gas sensor.* Applied Optics, 2003. **42**(18): p. 3509-3515.
12. Zhao, P., et al., *Mode-phase-difference photothermal spectroscopy for gas*

detection with an anti-resonant hollow-core optical fiber. Nature Communications, 2020. **11**(1): p. 847.

13. Yang, T., W. Chen, and P. Wang, *A review of all-optical photoacoustic spectroscopy as a gas sensing method.* Applied Spectroscopy Reviews, 2020. **56**(2): p. 143-170.
14. Xiong, Y. and F. Xu, *Multifunctional integration on optical fiber tips: challenges and opportunities.* Advanced Photonics, 2020. **2**(06).
15. Zhu, C., et al., *Advances in Fiber-Optic Extrinsic Fabry–Perot Interferometric Physical and Mechanical Sensors: A Review.* IEEE Sensors Journal, 2023. **23**(7): p. 6406-6426.
16. Sasaki, M., et al., *Direct Photolithography on Optical Fiber End.* Japanese Journal of Applied Physics, 2002. **41**(6S): p. 4350.
17. Kostovski, G., et al., *Nanoimprinted optical fibres: Biotemplated nanostructures for SERS sensing.* Biosensors and Bioelectronics, 2009. **24**(5): p. 1531-1535.
18. Prasciolu, M., et al., *Design and fabrication of on-fiber diffractive elements for fiber-waveguide coupling by means of e-beam lithography.* Microelectronic Engineering, 2003. **67-68**: p. 169-174.
19. Schiappelli, F., et al., *Efficient fiber-to-waveguide coupling by a lens on the end of the optical fiber fabricated by focused ion beam milling.* Microelectronic Engineering, 2004. **73-74**: p. 397-404.
20. Liberale, C., et al., *Micro-Optics Fabrication on Top of Optical Fibers Using Two-Photon Lithography.* IEEE Photonics Technology Letters, 2010. **22**(7): p. 474-476.
21. Jun Ki, K., et al., *Fabrication of Micro Fresnel Zone Plate Lens on a Mode-Expanded Hybrid Optical Fiber Using a Femtosecond Laser Ablation System.* IEEE Photonics Technology Letters, 2009. **21**(1): p. 21-23.
22. Pan, Y., et al., *Recent Advances in Light-Induced Thermoelastic Spectroscopy for Gas Sensing: A Review.* Remote Sensing, 2023. **15**(1): p. 69.
23. Bolshov, M.A., Y.A. Kuritsyn, and Y.V. Romanovskii, *Tunable diode laser spectroscopy as a technique for combustion diagnostics.* Spectrochimica Acta Part B: Atomic Spectroscopy, 2015. **106**: p. 45-66.

24. J. M. Langridge, et al., *Cavity enhanced absorption spectroscopy of multiple trace gas species using a supercontinuum radiation source.* Optics Express, 2008. **16**(14): p. 10178-10188.
25. Wang, Y., et al., *A Comprehensive Study of Optical Fiber Acoustic Sensing.* IEEE Access, 2019. **7**: p. 85821-85837.
26. Palzer, S., *Photoacoustic-Based Gas Sensing: A Review.* Sensors (Basel), 2020. **20**(9).
27. Yin, Y., et al., *Cantilever-enhanced photoacoustic spectroscopy for gas sensing: A comparison of different displacement detection methods.* Photoacoustics, 2022. **28**.
28. Besson, J.-P., *Photoacoustic spectroscopy for multi-gas sensing using near infrared lasers*. 2006, Swiss Federal Institute of Technology.
29. Tam, A.C., *Ultra sensitive laser spectroscopy*. 1983, New York: Academic press.
30. Trusler, J.P.M., in *Measurement Science and Technology*. 1991: Bristol.
31. A. Miklos, S.S., and P. Hess, *Photoacoustic spectroscopy, Theory, Encyclopedia of spectroscopy and spectrometry*. 1999, New York: Academic Press.
32. Schilt, S., L. Thévenaz, and P. Robert, *Wavelength modulation spectroscopy: combined frequency and intensity laser modulation.* Applied Optics, 2003. **42**(33): p. 6728-6738.
33. Wang, Q., et al., *Recovery of pure wavelength modulation second harmonic signal waveforms in distributed feedback diode laser-based photoacoustic spectroscopy.* Sensors and Actuators A: Physical, 2016. **245**: p. 54-62.
34. G. Jacobsen, H.O., and F. Birkedahl, *Current/frequency modulation characteristics for directly optical frequency-modulated injection lasers at 830 nm and 1.3 μm.* Electron. Lett., 1982. **18**: p. 874-876.
35. Chao, X., J.B. Jeffries, and R.K. Hanson, *Wavelength-modulation-spectroscopy for real-time, in situ NO detection in combustion gases with a 5.2 μm quantum-cascade laser.* Applied Physics B, 2012. **106**(4): p. 987-997.
36. Nelson, D.F., D.A. Kleinman, and K.W. Wecht, *Vibration-induced modulation of fiberguide transmission.* Applied Physics Letters, 1977. **30**(2): p. 94-96.
37. Sheem, S.K. and J.H. Cole, *Acoustic sensitivity of single-mode optical power*

dividers. Optics Letters, 1979. **4**(10): p. 322-324.

38. Li, C., et al., *A sensitivity-enhanced flexible acoustic sensor using side-polished fiber Bragg grating.* Measurement, 2018. **117**: p. 252-257.
39. Beard, P.C. and T.N. Mills, *Extrinsic optical-fiber ultrasound sensor using a thin polymer film as a low-finesse Fabry–Perot interferometer.* Applied Optics, 1996. **35**(4): p. 663-675.
40. Ma, J., et al., *Fiber-Optic Fabry–Pérot Acoustic Sensor With Multilayer Graphene Diaphragm.* IEEE Photonics Technology Letters, 2013. **25**(10): p. 932-935.
41. Liu, L., et al., *Fiber-Optic Michelson Interferometric Acoustic Sensor Based on a PP/PET Diaphragm.* IEEE Sensors Journal, 2016. **16**(9): p. 3054-3058.
42. Zhao, Y., et al., *Small in-fiber Fabry-Perot low-frequency acoustic pressure sensor with PDMS diaphragm embedded in hollow-core fiber.* Sensors and Actuators A: Physical, 2018. **270**: p. 162-169.
43. Zhang, B., et al., *Flexible Hollow Core Fiber Photoacoustic Gas Sensor Based on Embedded Acoustic Resonant Structure.* Anal Chem, 2023. **95**(34): p. 12761-12767.
44. NessAiver, M.S., et al., *Recording high quality speech during tagged cine-MRI studies using a fiber optic microphone.* Journal of Magnetic Resonance Imaging, 2006. **23**(1): p. 92-97.
45. Suchánek, J., et al., *Photoacoustic spectroscopy with mica and graphene micro-mechanical levers for multicomponent analysis of acetic acid, acetone and methanol mixture.* Microchemical Journal, 2019. **144**: p. 203-208.
46. Bilaniuk, N., *Optical microphone transduction techniques.* Applied Acoustics, 1997. **50**(1): p. 35-63.
47. Munir, Q. and H.P. Weber, *Fiberoptic sensor in a resonant optoacoustic cell.* Optics Communications, 1984. **52**(4): p. 269-273.
48. Wang, S., et al., *Optical interferometer-based methods for photoacoustic gas sensing: a review.* Applied Spectroscopy Reviews, 2023. **59**(3): p. 382-421.
49. Shi, J., et al., *Remote Gas Pressure Sensor Based on Fiber Ring Laser Embedded With Fabry–Pérot Interferometer and Sagnac Loop.* IEEE Photonics Journal, 2016.

8(5): p. 1-8.

50. Wang, Q., et al., *An all-optical photoacoustic spectrometer for trace gas detection.* Sensors and Actuators B: Chemical, 2011. **153**(1): p. 214-218.
51. Cao, Y., et al., *Miniature fiber-tip photoacoustic spectrometer for trace gas detection.* Optics Letters, 2013. **38**(4): p. 434-436.
52. Ma, J., et al., *Microscale fiber photoacoustic spectroscopy for in situ and real-time trace gas sensing.* Advanced Photonics, 2024. **6**(6): p. 066008.
53. Wang, J., et al., *Cantilever-enhanced dual-comb photoacoustic spectroscopy.* Photoacoustics, 2024. **38**.
54. Xu, J., et al., *Miniature all-silica fiber optic pressure and acoustic sensors.* Optics Letters, 2005. **30**(24): p. 3269-3271.
55. Wang, W., et al., *Miniature all-silica optical fiber pressure sensor with an ultrathin uniform diaphragm.* Optics Express, 2010. **18**(9): p. 9006-9014.
56. Wang, F., et al., *Extrinsic Fabry–Pérot Underwater Acoustic Sensor Based on Micromachined Center-Embossed Diaphragm.* Journal of Lightwave Technology, 2014. **32**(23): p. 4628-4636.
57. Guo, F., et al., *High-sensitivity, high-frequency extrinsic Fabry–Perot interferometric fiber-tip sensor based on a thin silver diaphragm.* Optics Letters, 2012. **37**(9): p. 1505-1507.
58. Liu, B., et al., *Extrinsic Fabry-Perot fiber acoustic pressure sensor based on large-area silver diaphragm.* Microelectronic Engineering, 2016. **166**: p. 50-54.
59. Chen, K., et al., *Fiber-optic Fabry-Perot interferometer based high sensitive cantilever microphone.* Sensors and Actuators A: Physical, 2018. **279**: p. 107-112.
60. Chen, L.H., et al., *High performance chitosan diaphragm-based fiber-optic acoustic sensor.* Sensors and Actuators A: Physical, 2010. **163**(1): p. 42-47.
61. Gong, Z., et al., *High-Sensitivity Fabry-Perot Interferometric Acoustic Sensor for Low-Frequency Acoustic Pressure Detections.* Journal of Lightwave Technology, 2017. **35**(24): p. 5276-5279.
62. Ni, W., et al., *Ultrathin graphene diaphragm-based extrinsic Fabry-Perot interferometer for ultra-wideband fiber optic acoustic sensing.* Opt Express, 2018.

26(16): p. 20758-20767.

63. Wu, Y., et al., *A Highly Sensitive Fiber-Optic Microphone Based on Graphene Oxide Membrane.* Journal of Lightwave Technology, 2017. **35**(19): p. 4344-4349.
64. Moradi, H., et al., *Ultrasensitive fiber optic Fabry Pérot acoustic sensor using phase detection.* Measurement, 2021. **172**: p. 108953.
65. Yingchun Cao, et al., *Miniature fiber-tip photoacoustic spectrometer for trace gas detection.* Optics Letters, 2013. **38**(4): p. 434-436.
66. Gong, Z., et al., *High-sensitivity fiber-optic acoustic sensor for photoacoustic spectroscopy based traces gas detection.* Sensors and Actuators B: Chemical, 2017. **247**: p. 290-295.
67. Xiao, H., et al., *Ultra-sensitive ppb-level methane detection based on NIR all-optical photoacoustic spectroscopy by using differential fiber-optic microphones with gold-chromium composite nanomembrane.* Photoacoustics, 2022. **26**: p. 100353.
68. Zhou, S., M. Slaman, and D. Iannuzzi, *Demonstration of a highly sensitive photoacoustic spectrometer based on a miniaturized all-optical detecting sensor.* Opt Express, 2017. **25**(15): p. 17541-17548.
69. Guo, M., et al., *Miniaturized anti-interference cantilever-enhanced fiber-optic photoacoustic methane sensor.* Sensors and Actuators B: Chemical, 2022. **370**.
70. Li, C., et al., *Fiber-Optic Photoacoustic Gas Sensor with Multiplexed Fabry-Perot Interferometric Cantilevers.* Anal Chem, 2023. **95**(48): p. 17477-17485.
71. Iannuzzi, D., et al., *Monolithic fiber-top sensor for critical environments and standard applications.* Applied Physics Letters, 2006. **88**(5).
72. André, R.M., et al., *Focused ion beam post-processing of optical fiber Fabry-Perot cavities for sensing applications.* Optics Express, 2014. **22**(11): p. 13102-13108.
73. Vaiano, P., et al., *Lab on Fiber Technology for biological sensing applications.* Laser & Photonics Reviews, 2016. **10**(6): p. 922-961.
74. Dai, G., et al., *Photothermally stabilized Fabry-Perot cavity with patterned nanofilm for photoacoustic trace gas sensing.* Sensors and Actuators B: Chemical,

2022. **355**: p. 131259.

75. Fan, E., et al., *Compact optical fiber photoacoustic gas sensor with integrated multi-pass cell.* Photoacoustics, 2023. **32**: p. 100524.
76. Said, A.A., et al., *Carving fiber-top cantilevers with femtosecond laser micromachining.* Journal of Micromechanics and Microengineering, 2008. **18**(3): p. 035005.
77. Lin, Y., J. Guo, and R.G. Lindquist, *Demonstration of an ultra-wideband optical fiber inline polarizer with metal nano-grid on the fiber tip.* Optics Express, 2009. **17**(20): p. 17849-17854.
78. Consales, M., et al., *Lab-on-Fiber Technology: Toward Multifunctional Optical Nanoprobes.* ACS Nano, 2012. **6**(4): p. 3163-3170.
79. Yao, M., et al., *Optical Fiber-Tip Sensors Based on In-Situ μ-Printed Polymer Suspended-Microbeams.* Sensors, 2018. **18**(6): p. 1825.
80. Wu, J., et al., *Optical Fiber-Tip Fabry–Pérot Interferometric Pressure Sensor Based on an In Situ μ-Printed Air Cavity.* Journal of Lightwave Technology, 2018. **36**(17): p. 3618-3623.
81. Yao, M., et al., *Ultracompact optical fiber acoustic sensors based on a fiber-top spirally-suspended optomechanical microresonator.* Opt Lett, 2020. **45**(13): p. 3516-3519.
82. Peng, W., et al., *Miniature optical fiber accelerometer based on an in-situ 3D microprinted ferrule-top Fabry–Pérot microinterferometer.* Light: Advanced Manufacturing, 2025. **6**(1): p. 152-160.
83. Tan, D., et al., *Reduction in feature size of two-photon polymerization using SCR500.* Applied Physics Letters, 2007. **90**(7).
84. Malinauskas, M., et al., *Ultrafast laser processing of materials: from science to industry.* Light: Science & Applications, 2016. **5**(8): p. e16133-e16133.
85. Liu, Q., et al., *“Optical tentacle” of suspended polymer micro-rings on a multicore fiber facet for vapor sensing.* Optics Express, 2020. **28**(8): p. 11730-11741.
86. Zou, M., et al., *Fiber-tip polymer clamped-beam probe for high-sensitivity*

nanoforce measurements. Light Sci Appl, 2021. **10**(1): p. 171.

87. Jin, W., et al., *Ultra-sensitive all-fibre photothermal spectroscopy with large dynamic range.* Nature Communications, 2015. **6**(1): p. 6767.
88. Long, D.A., et al., *Nanosecond time-resolved dual-comb absorption spectroscopy.* Nature Photonics, 2024. **18**(2): p. 127-131.
89. Karhu, J., et al., *LED-Based Photoacoustic NO_2 Sensor with a Sub-ppb Detection Limit.* ACS Sens, 2021. **6**(9): p. 3303-3307.
90. Fathy, A., et al., *Direct Absorption and Photoacoustic Spectroscopy for Gas Sensing and Analysis: A Critical Review.* Laser & Photonics Reviews, 2022. **16**(8): p. 2100556.
91. Lay-Ekuakille, A., G. Vendramin, and A. Trotta, *LED-based sensing system for biomedical gas monitoring: Design and experimentation of a photoacoustic chamber.* Sensors and Actuators B: Chemical, 2009. **135**(2): p. 411-419.
92. Mitrayana, D.K. Apriyanto, and M. Satriawan, *CO_2 Laser Photoacoustic Spectrometer for Measuring Acetone in the Breath of Lung Cancer Patients.* Biosensors, 2020. **10**(6): p. 55.
93. Yin, X., et al., *Highly sensitive photoacoustic multicomponent gas sensor for SF_6 decomposition online monitoring.* Opt Express, 2019. **27**(4): p. A224-A234.
94. Szabó, A., et al., *In situ and wide range quantification of hydrogen sulfide in industrial gases by means of photoacoustic spectroscopy.* Measurement Science and Technology, 2013. **24**(6): p. 065501.
95. Huszár, H., et al., *Ammonia monitoring at ppb level using photoacoustic spectroscopy for environmental application.* Sensors and Actuators B: Chemical, 2008. **134**(2): p. 1027-1033.
96. Zifarelli, A., et al., *Multi-gas quartz-enhanced photoacoustic sensor for environmental monitoring exploiting a Vernier effect-based quantum cascade laser.* Photoacoustics, 2022. **28**: p. 100401.
97. Ma, Y., et al., *In-plane quartz-enhanced photoacoustic spectroscopy.* Applied Physics Letters, 2020. **116**(6): p. 061101.
98. Wang, J., et al., *Quartz-enhanced multiheterodyne resonant photoacoustic*

spectroscopy. Light Sci Appl, 2024. **13**(1): p. 77.

99. Sampaolo, A., et al., *Quartz-enhanced photoacoustic spectroscopy for multi-gas detection: A review.* Anal Chim Acta, 2022. **1202**: p. 338894.
100. Wu, H., et al., *Beat frequency quartz-enhanced photoacoustic spectroscopy for fast and calibration-free continuous trace-gas monitoring.* Nature Communications, 2017. **8**: p. 15331.
101. Qiao, S., et al., *Ultra-highly sensitive HCl-LITES sensor based on a low-frequency quartz tuning fork and a fiber-coupled multi-pass cell.* Photoacoustics, 2022. **27**: p. 100381.
102. Zhao, J., et al., *Ppb-level all-optical off-axis QEPAS gas sensor based on dual-wavelength demodulation of out-of-plane vibration mode.* Sensors and Actuators B: Chemical, 2023. **385**: p. 133689.
103. Li, C., et al., *Miniature single-fiber photoacoustic sensor for methane gas leakage detection.* Optics and Lasers in Engineering, 2022. **149**: p. 106792.
104. Guo, M., et al., *High-Sensitivity Silicon Cantilever-Enhanced Photoacoustic Spectroscopy Analyzer with Low Gas Consumption.* Anal Chem, 2022. **94**(2): p. 1151-1157.
105. Li, T., et al., *Optical Fiber Ferrule-Top Spirally-Suspended Optomechanical Microresonators for Photoacoustic Spectroscopic Gas Sensing*, in *2023 Conference on Lasers and Electro-Optics Europe & European Quantum Electronics Conference (CLEO/Europe-EQEC)*. 2023. p. 1-1.
106. Li, T., et al., *Miniature optical fiber photoacoustic spectroscopy gas sensor based on a 3D micro-printed planar-spiral spring optomechanical resonator.* Photoacoustics, 2024. **40**: p. 100657.
107. Shi, S., et al., *High Sensitivity MEMS Accelerometer Using PZT-Based Four L-Shaped Beam Structure.* IEEE Sensors Journal, 2022. **22**(8): p. 7627-7636.
108. Bruno, F.A., et al., *Opto-Mechanical Lab-on-Fiber Accelerometers.* Journal of Lightwave Technology, 2020. **38**(7): p. 1998-2009.
109. John J. Parise, Larry L. Howell, and S.P. Magleby, *Ortho-planar linear-motion springs.* Mechanism and Machine Theory, 2001. **36**(11-12): p. 1281-1299.

110. Lorenz, H., et al., *SU-8: a low-cost negative resist for MEMS.* J. Micromech. Microeng, 1997. **7**: p. 121-124.
111. Shang, X., et al., *Fiber-Integrated Force Sensor using 3D Printed Spring-Composed Fabry-Perot Cavities with a High Precision Down to Tens of Piconewton.* Adv Mater, 2024. **36**(2): p. e2305121.
112. Zhao, P., et al., *Ultraminiature Optical Fiber-Tip 3D-Microprinted Photothermal Interferometric Gas Sensors.* Laser & Photonics Reviews, 2024: p. 2301285.
113. Chen, K., et al., *Fast demodulated white-light interferometry-based fiber-optic Fabry–Perot cantilever microphone.* Optics Letters, 2018. **43**(14): p. 3417-3420.
114. Zhao, X., et al., *Fiber-optic photoacoustic gas sensing: a review.* Applied Spectroscopy Reviews, 2024: p. 1-29.
115. Allan, D.W., *Statistics of atomic frequency standards.* Proceedings of the IEEE, 1966. **54**(2): p. 221 - 230.
116. Werle, P., R. Mücke, and F. Slemr, *The limits of signal averaging in atmospheric trace-gas monitoring by tunable diode-laser absorption spectroscopy (TDLAS).* Applied Physics B 1993. **57**: p. 131-139.
117. Chen, K., et al., *Fiber-optic photoacoustic gas sensor with temperature self-compensation.* Optics Letters, 2020. **45**(8): p. 2458-2461.
118. Kuusela, T. and J. Kauppinen, *Photoacoustic Gas Analysis Using Interferometric Cantilever Microphone.* Applied Spectroscopy Reviews, 2007. **42**(5): p. 443-474.
119. Pangerl, J., et al., *Characterizing a sensitive compact mid-infrared photoacoustic sensor for methane, ethane and acetylene detection considering changing ambient parameters and bulk composition (N2, O2 and H2O).* Sensors and Actuators B: Chemical, 2022. **352**: p. 130962.
120. Zhou, S. and D. Iannuzzi, *A fiber-tip photoacoustic sensor for in situ trace gas detection.* Review of Scientific Instruments, 2019. **90**(2).
121. Zheng, K., et al., *Waveguide-Based On-Chip Photothermal Spectroscopy for Gas Sensing.* Laser & Photonics Reviews, 2024. **18**(5): p. 2301071.
122. Qiao, S., et al., *Ultra-highly sensitive dual gases detection based on photoacoustic*

spectroscopy by exploiting a long-wave, high-power, wide-tunable, single-longitudinal-mode solid-state laser. Light: Science & Applications, 2024. **13**(1): p. 100.

123. Liu, Y., et al., *A highly sensitive LITES sensor based on a multi-pass cell with dense spot pattern and a novel quartz tuning fork with low frequency.* Opto-Electronic Advances, 2024. **7**(3): p. 230230-1-230230-9.
124. Li, C., et al., *Fiber-Optic Photoacoustic Gas Microsensor Dual Enhanced by Helmholtz Resonator and Interferometric Cantilever.* Analytical Chemistry, 2024. **96**(23): p. 9438-9446.